

Pressure-impulse diagrams for vented hydrogen deflagrations in 20-foot shipping containers

Numerical predictions using the Impetus Afea solver
and validation against data from full-scale experiments

By

Maiken Knutsen

Master of Science Thesis in

Process Safety Technology



Department of Physics and Technology

University of Bergen

September 2020

Acknowledgments

First and foremost, I would like to thank Dr. Arve Grønsund Hanssen at Impetus Afea for the help, expertise, and guidance throughout the work with this thesis and for providing the finite element tool, Impetus Afea Solver, used in this thesis. He has been very cooperative and provided important material needed to complete the thesis. Furthermore, I would like to express my appreciation towards my supervisor Dr. Trygve Skjold. His expertise and guidance have been very helpful.

Finally, I would like to express my gratitude towards my family and friends for their endless support and encouragement throughout this process.

Abstract

A pressure-impulse (P-I) diagram is a graphical representation of the level of structural response of a given structure to pressure loads characterised by different combinations of pressure and impulse. Weak structures, such as buildings and shipping containers, can experience considerable structural damage if subjected to relatively modest internal pressure loads, and it is important to dimension both enclosures and venting devices in a way that prevents structural collapse and the formation of projectiles. Shipping containers are often utilized for housing process equipment, such as compressors and electrolysers. Fires and explosions represent a significant hazard for such installations, and knowledge about how a specific structure responds to internal pressure loads is useful for risk assessments and safe design.

In the present study, P-I curves were created numerically for several wall displacements using the non-linear explicit finite element (FE) tool Impetus Afea Solver. The characteristics of the curves agree well with the theoretical characteristics of non-ideal explosions with finite rise time. The curves from the finite element method were compared to unique results from full-scale experiments conducted as part of the EU funded HySEA project. Most of the experimental results were located in the dynamic region of the P-I diagram. To make it easier to compare the experimental results with the different areas of damage in the P-I diagram, the experimental results were divided into categories of maximum displacement. Whereas some of the experimental results correspond to the areas in the P-I diagram with the same level of damage, others do not. There are several sources of uncertainty associated with both the numerical approach and the experiments. Sensitivity studies were performed to study the impact of varying the yield strength of the material in the container walls, moderate damage to the corrugated structure, and different pressure-time profiles for the pressure loads. Reducing the assumed yield strength of the material resulted in a significant increase in wall displacement. Damage to one of the walls affected not only the wall displacement of the damaged wall but the entire structure. Despite the deviations between model predictions and experiments, the use of P-I diagrams may still be valuable for safety and design purposes. The primary limitation from an engineering design point of view will most likely be the reliable prediction of the relevant pressure loads for a given structure.

The suggestions for further work include the use of a more detailed model for the FE tool, combined with direct comparison of the structural response obtained with the measured pressure-time histories for repeated loading of the same structure. This will require more computationally intensive calculations than could be included in the present study.

Nomenclature

Abbreviations

BB	Bottle basket
bc	Back wall centre ignition position
bu	Back wall upper ignition position
DDT	Deflagration to detonation transition
FO	Frame only
fc	Floor centre ignition position
FEM	Finite element method
FEA	Finite element analysis
FACEDAP	The Facility and Component Explosive Damage Assessment Program
LFL	Lower flammability limit
MIE	Minimum ignition energy
P-I	Pressure-impulse
PR	Pipe rack
RC	Reinforced concrete
SDOF	Single degree of freedom
UFL	Upper flammability limit

Symbols

A	Cross sectional area	[m ²]
a	Acceleration	[m/s ²]
B	Bulk modulus	[N/m ²]
C	Viscous damping constant	[Kg/s]
D_m	Maximum displacement	[cm]
D_p	Permanent deformation	[cm]
E	Young`s Modulus/ elastic modulus	[N/m ²]
F	Applied force	[N]

F_s	Force needed to extend or compress a spring	[N]
F_m	Maximum force on the system	[N]
I	Impulse	[Pa s]
i	Scaled impulse	[-]
k	Spring constant/stiffness of system	[N/m]
L	Length of object/structure	[m]
ΔL	Compression or elongation of object/structure/spring	[m]
M	Mass of the system	[kg]
P	Pressure	[Pa]
P_m	Maximum overpressure	[Pa]
p	Scaled pressure	[-]
S	Shear modulus	[N/m ²]
T	Natural period of vibration of the structure	[s]
t	Time	[s]
t_d	Load function duration	[s]
t_r	Pressure rise time	[s]
u	Velocity	[m/s]
ν	Kinematic viscosity	[m ² /s]
w_{max}	Maximum wall displacement	[m]
X_{max}	Maximum displacement	[m]
y	Displacement	[m]
Y_m	Maximum structural deflection	[m]

Greek symbols

σ	Stress	[Pa]
ε	Strain	[-]

Table of Contents

Acknowledgments	i
Abstract	ii
Nomenclature.....	iii
1 Introduction.....	1
2 General theory.....	4
2.1 Gas explosions	4
2.1.1 What is a gas explosion?	4
2.1.2 Consequences of gas explosions	4
2.2 Deflagration and detonation	5
2.2.1 Deflagration.....	5
2.2.2 Detonation.....	6
2.3 Hydrogen	6
2.3.1 Hydrogen properties	6
2.3.2 Minimum ignition energy	7
2.3.3. Flammability limits	7
2.4 Structural response	8
2.4.1 Stress, strain, and deformation	9
2.4.2 Reflection.....	11
2.4.3 Natural periods and resonance	12
2.4.4 Static versus dynamic response	12
2.4.5 Material	12
2.4.6 Damping	13
2.5 SDOF-system.....	13
2.6 Finite element method.....	15
2.7 P-I diagrams.....	15
3 The HySEA project	18
4 Literature review	22
4.1 Analytical method for generating P-I diagrams.....	22
4.2 Numerical methods for generating P-I diagrams	25
4.3 Experimental methods for generating P-I diagrams	30
5 Methodology	32
5.1 Methodology for generating numerical P-I diagrams using the Impetus Afea Solver	32
5.1.1 Background.....	32
5.1.2 Model simplifications	33

5.1.3 Model sensitivity studies.....	34
5.1.4 Final model.....	36
6 Results and discussion.....	38
6.1 Numerical pressure- impulse diagrams.....	38
6.1.1 P-I diagram for maximum wall displacement of 20 cm.....	39
6.1.2 P-I diagram for maximum wall displacement vs experimental results	40
6.2 Influence of steel strength on the structural response.....	57
6.3 Structural response with a dent in the frame	62
6.4 Harmonic vs triangular pressure load	72
6.5 20 cm P-I curve compilation.....	74
7 Conclusion and suggestion for further work.....	76
Bibliography.....	79
Appendix A: Results from simulated P-I curves for 5, 10, 20 and 30 cm displacement.....	83
Appendix B: Test results from the HySEA project	85
Appendix C: Further test details from the HySEA project.....	89
Appendix D: Maximum displacement and permanent deformation from the HySEA project	92
Appendix E: P-I curve results for w_{max} with a material yield strength of 235 MPa	94
Appendix F: Percentage increase in displacement with a dent	96
Appendix G: Uncertainty calculation.....	100
Appendix H: P-I curve results from triangular pressure loads	101

1 Introduction

With the world's increasing energy demands the search for environmentally friendly energy is critical. Hydrogen can potentially play a key role as an energy carrier in future sustainable energy systems. The fossil-based energy sources used today are non-renewable, and with its negative environmental impacts, interest in alternative energy sources has increased (Rosen & Koochi-Fayegh, 2016). The inherently intermittent and varying nature of renewable energy sources such as solar and wind implies a need for energy carriers for storing and transporting energy. Hydrogen is a promising energy carrier, partly due to the high specific energy content, and especially because it is carbon-free. Today hydrogen is mainly used as a feedstock in the production of petrochemicals and fertilizer, but the interest in using hydrogen as an energy carrier has increased significantly in recent years (Aarnes, et al., 2018; NMPE & NMCE, 2020; EU, 2020).

With the increasing interest in hydrogen as an energy carrier, hydrogen safety must be considered. Hydrogen is the lightest element; it is colourless, odourless, and has very low ignition energy (Najjar, 2013). In the industry, it is common practice to install hydrogen energy applications, such as refuelling stations, electrolysers, fuel cell backup systems, or other equipment in containers or smaller enclosures (Atanga, et al., 2019). Shipping containers are cost-effective, easy to install, and portable. Ignited releases resulting in fires and explosions represent a significant hazard for systems involving hydrogen energy applications and can result in severe losses in society (Skjold, et al., 2019c; EU, 2020). Identifying, preventing- and mitigating hazards associated with hydrogen installations in containers is critical for safe operations and design (Vendra & Wen, 2019).

Fires and explosions can cause severe damage to structures and their surroundings. Risk-reducing measures are usually required for systems involving hydrogen energy applications. Venting can be an effective way to reduce the risk of possible deflagrations in a confined area. For safe design purposes, it is important to consider the integrity and the structural response of the structure (Skjold, et al., 2019c). The focus of this thesis is on 20-foot shipping containers, which are relatively weak structures, and where the dynamic response is especially relevant.

The HySEA project

The 66 vented hydrogen deflagration experiments performed by Gexcon as part of the HySEA project consumed twelve containers from the same manufacturing series. The test matrix included 42 tests where the mixture was initially homogeneous and quiescent; 14 tests with venting through the doors, one test in a closed container, and 27 tests with venting through openings in the roof. The last 24 tests involved inhomogeneous mixtures; 17 with stratified mixtures and the remaining seven with initial turbulence generated by a transient jet or a fan

(Skjold, et al., 2019b). Other parameters investigated include hydrogen concentration, vent area, type of venting device, ignition position, and type and level of congestion inside the container. The results show that the maximum reduced explosion pressure can increase significantly with internal congestion, compared to an empty container (Skjold, 2018a). The pressure inside the container was measured by eight piezoelectric sensors in different locations, and the dynamic deflection of the container walls was measured by two Laser displacement sensors. Test number 70 was carried out to investigate the structural response of a quasi-static internal pressure load. This was done for a closed container, with no vent openings, and a low reactivity mixture of 12 vol.% hydrogen in air. The duration of the quasi-static pressure load had to be significantly longer than 60 milliseconds since the natural frequency of the container walls was about 15-17 Hz. The doors remained closed in Test 70, even though some leakage occurred, and the confined deflagration resulted in a near-constant overpressure of 0.3 bar for approximately one second (Skjold, et al., 2019c).

P-I diagrams

Weak structures, such as buildings and containers, may experience extensive structural damage when subjected to an internal pressure load. Pressure-impulse (P-I) diagrams are useful for evaluating which combination of pressure and impulse that will result in a specific level of damage on a specific structure. The P-I diagram can then be divided into regions with different degrees of damage, e.g. negligible damage, moderate damage, and failure. Figure 1.1 illustrates a P-I diagram with a typical P-I curve for an ideal blast load (Baker, et al., 1983; Krauthammer, et al., 2008).

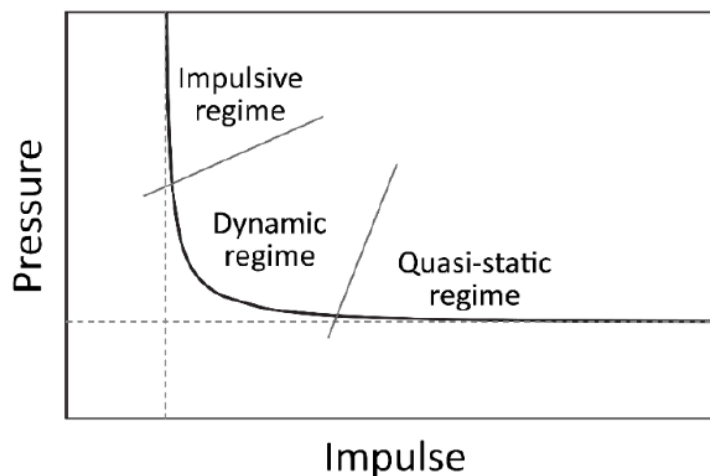


Figure 1.1. Illustration of a P-I diagram with a single P-I curve (Skjold, et al., 2019c).

Objective

The primary objective of the present study was to develop representative P-I curves for 20-foot shipping containers utilizing a numerical method, and to compare the results with experimental data from the full-scale experiments performed as part of the HySEA project. The tool used for the simulations was the non-linear explicit finite element tool, Impetus Afea Solver. Sensitivity studies were also performed, including the influence of steel strength on the structure and the impact of moderate damage on the structural response. The novel aspect of the current contribution is the focus on internal deflagrations, since most previous work has focused on the structural response of structures subjected to idealised blasts generated by high explosives (i.e. blasts waves with near-zero rise time).

2 General theory

This chapter introduces basic concepts related to the structural response of structures subjected to pressure loads generated in explosions.

2.1 Gas explosions

Accidental explosions represent a significant hazard in industries that produce, transport, store, or process flammable substances. Many of the largest property losses in society are associated with accidental explosions (MARSH, 2018). To reduce the frequency and consequences of accidental gas explosions it is imperative to have a good understanding of what a gas explosion is (Bjerketvedt, et al., 1997).

2.1.1 What is a gas explosion?

According to Bjerketvedt et al. (1997), a gas explosion can be defined as a process where the combustion of a premixed gas cloud, for example, a fuel-oxidizer, causes a rapid increase of pressure. Gas explosions can occur in various environments. They can occur in unconfined or open process areas, offshore, in buildings, in pipes, during transport by e.g. vehicles or ships, and inside process equipment.

2.1.2 Consequences of gas explosions

Figure 2.1 shows an event tree that summarises some typical consequences that can result from an accidental release of combustible gas or liquid into the ambient atmosphere. Depending on the circumstances, ignition can occur immediately or delayed. A fire will occur if combustible gas or vapour ignites before it mixes with ambient air or an oxidizer. If a pre-mixed combustible fuel-air cloud is formed and ignition occurs, it can result in a very dangerous situation with potentially disastrous consequences. An explosion can lead to material damage, casualties, huge economic losses, and result in a domino effect with accidents such as fires or BLEVE's (Boiling liquid expanding vapour explosions). It is not straightforward to estimate the consequences of gas explosions. Bjerketvedt et al. (1997) list the following factors that may influence the development and consequences of gas explosion scenarios:

- Type of fuel and oxidizer
- Fuel concentration
- Size of the combustible cloud
- Location of ignition
- Strength of the ignition source
- Size, location, and type of explosion vent areas
- Location and size of structural elements and equipment (congestion/confinement)
- Flammability limits of the fuel

- Mitigation schemes

Gas explosions can be classified according to the environment within which they take place:

- I. Confined gas explosions: within containers, tanks, process equipment, pipes, closed rooms, underground, etc.
- II. Partly confined gas explosions: in a compartment, buildings, or offshore modules.
- III. Unconfined gas explosions: in process plants and other unconfined areas.

It is important to be aware that gas explosions can occur in any of these environments, as well as in a combination of these environments. (Bjerketvedt, et al., 1997)

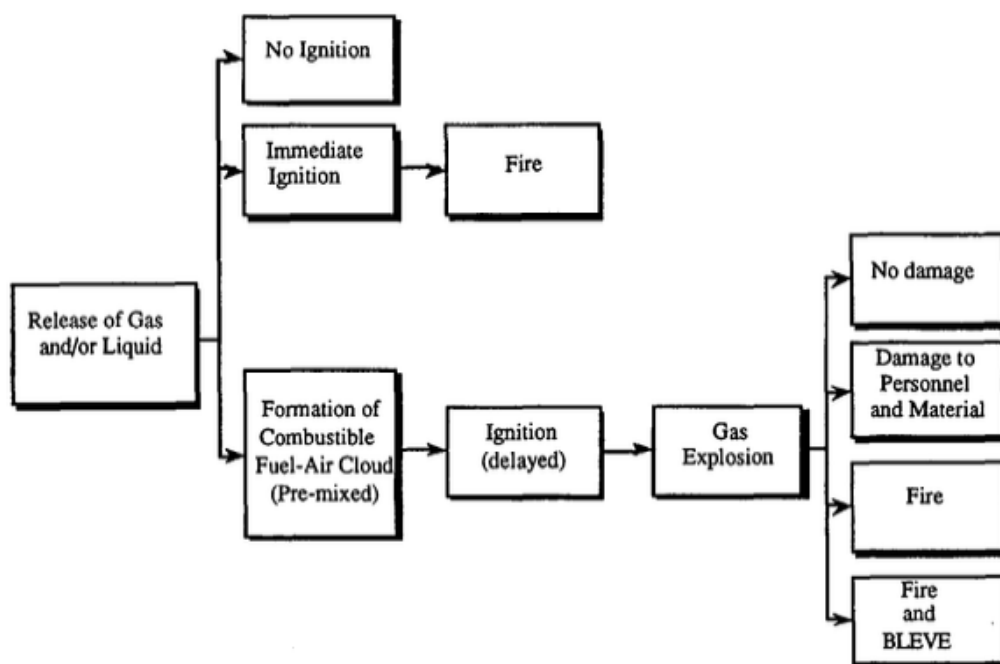


Figure 2.1. An event tree showing typical consequences of accidental releases of combustible gas or liquid into the atmosphere (Bjerketvedt, et al., 1997).

2.2 Deflagration and detonation

How fast the flame propagates and whether the pressure can be relieved will determine the pressure load on structures. The flame can propagate in two different modes through a flammable cloud: deflagration and detonation (Bjerketvedt, et al., 1997).

2.2.1 Deflagration

Deflagration is the most common mode of flame propagation for accidental gas explosions. A deflagration entails subsonic combustion, which means that the flame front propagates at a subsonic speed relative to the unburnt gas ahead of the flame. Turbulence can influence the

flame front velocity in deflagrations. High turbulence intensity will in general lead to a higher burning rate due to wrinkled flame front and turbulent mass and heat transfer (Bjerketvedt, et al., 1997).

2.2.2 Detonation

Detonation can be described as a flame front that is coupled to a shock wave. The peak overpressure increases significantly in detonations, and it is the most devastating form of gas explosions (King, 1990). A detonation is often referred to as supersonic combustion, which means that the flame front propagates at a supersonic speed relative to the unburnt gas ahead of the flame (Bjerketvedt, et al., 1997).

2.3 Hydrogen

Hydrogen is an energy carrier that can contribute to the world's reduced greenhouse gas emissions and air pollution (Ng & Lee, 2007). It is considered a perfect fuel as it is energy-efficient and clean (Najjar, 2013). Processes that produce, transport, or use hydrogen are referred to as hydrogen technologies. Hydrogen has several areas of application. It can be used to power fuel cells, turbines, combustion engines, to produce ammonia, to hydrogenate petroleum products as well as various industrial processes, such as glass production and manufacturing of electronics (Rivkin, et al., 2015).

An increase in the use of hydrogen as an energy carrier in the future will bring the public in closer contact with larger quantities of hydrogen. This brings safety-related issues that must be addressed (Ng & Lee, 2007). Equipment for hydrogen applications is often installed or stored in 20 or 40-foot shipping containers (Vendra & Wen, 2019). For such installations, fire and explosions represent a significant hazard (Skjold, et al., 2018c). Hydrogen accidents could lead to several different hazards. Some examples of hazards are asphyxiation, thermal hazards (e.g. frostbite), and pressure effects from deflagrations or detonations. If suitable safety measures are applied, the damage may be reduced. If hydrogen safety is neglected, it could lead to fatalities and costly consequences (Molkov, 2015).

2.3.1 Hydrogen properties

Hydrogen is a colourless, odourless, and extremely flammable gas. With an atomic number of one, it is the lightest element. It has a low ignition energy (0.017 mJ) and a wide flammability range (4-75 vol.%). Hydrogen has the highest specific energy [mJ/kg] compared to any other fuel (Aarnes, et al., 2018). However, the low energy density [mJ/litre] of hydrogen gas at ambient condition implies that hydrogen usually is stored and transported at high pressures (690-1030 bar) or low temperature (~20 K) (Rivkin, et al., 2015).

Since hydrogen is lighter than air, a flammable cloud will rise due to buoyancy. Hydrogen is a very reactive fuel that can result in quick acceleration of deflagration and potentially a transition to detonation, DDT. Hydrogen explosions can result in severe damage. Figure 2.2 summarizes the result from experiments with different stoichiometric fuel-air mixtures in a ten-meter long wedge-shaped vessel. Hydrogen and ethylene give higher explosion pressures compared to the other fuels under the same conditions (Bjerketvedt, et al., 1997).

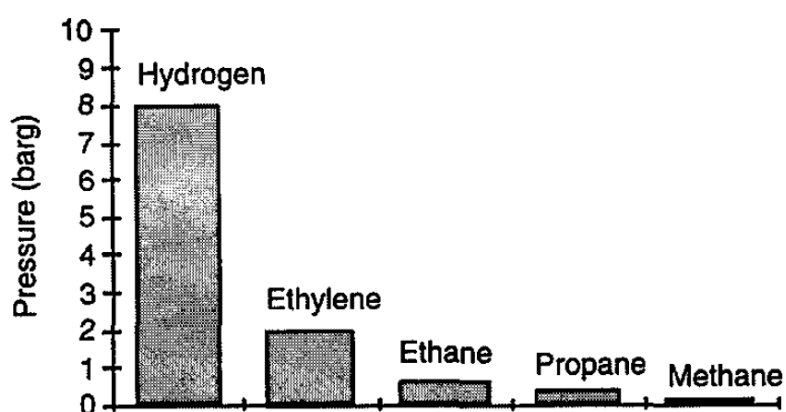


Figure 2.2. Comparison of resulting explosion pressures for different stoichiometric fuel-air mixtures in a 10-meter long wedge-shaped vessel under the same conditions (Bjerketvedt, et al., 1997).

2.3.2 Minimum ignition energy

The minimum ignition energy, MIE, is the minimum energy that is needed to successfully ignite a flammable fuel-oxidizer mixture (Bjerketvedt, et al., 1997). Examples of ignition sources are an electric spark or an electrostatic discharge (Eckhoff, 2016). The ignition energy depends on the fuel concentration. It is between 0.1 and 0.3 mJ in ambient air for most combustible fuels, but, significantly lower for hydrogen (0.017 mJ) (Babrauskas, 2003).

2.3.3. Flammability limits

Fuel-air mixtures are only able to propagate a flame within certain concentration limits. Outside of these limits, the fuel-air mixture is no longer flammable. These limits are referred to as the lower and upper flammability limits, respectively (LFL and UFL). Different fuel-air mixtures have different flammable ranges (Eckhoff, 2016). Figure 2.3 illustrates the flammable ranges for various fuels at ambient conditions. Hydrogen has a wide flammable range compared to the other fuel-air mixtures.

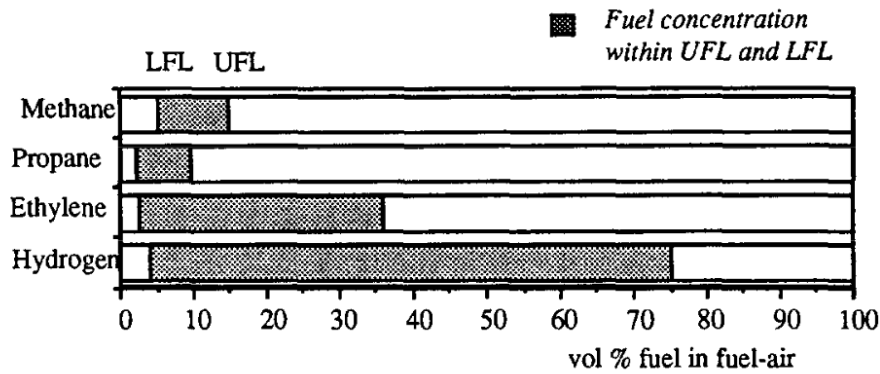


Figure 2.3. Flammable ranges for different fuel-air mixtures at 1 atm. and 25°C (Bjerketvedt, et al., 1997).

Figure 2.4 illustrates how the flammable range increases with increasing temperature (Bjerketvedt, et al., 1997).

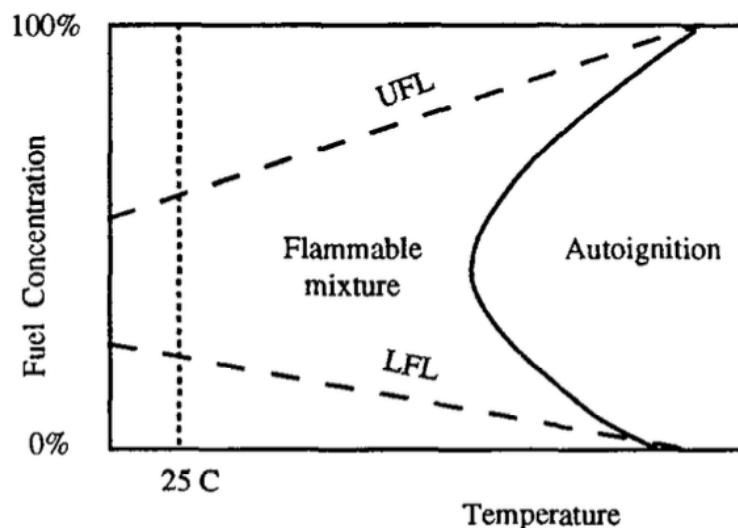


Figure 2.4. Illustration of the effect of increased temperature on LFL and UFL (Bjerketvedt, et al., 1997).

2.4 Structural response

Safe design of structures that may be subjected to pressure loads from a gas explosion requires an adequate understanding of how the structures respond to transient load. The structural response may involve deflection, internal stress, strain, deformation, rupture, collapse, or projectiles (Tedesco, et al., 1999). Several factors affect the structural response, including layout, material properties, damping characteristics, congestion, explosive components, and the position of the ignition source (Bangash & Bangash, 2006).

2.4.1 Stress, strain, and deformation

To determine if a pressure load would damage a structure or a building it is necessary to understand how stress and strain inflict deformation (Baker, et al., 1983). An explosion will produce pressure differences and the blast load can create internal stresses and forces on the structure. When the stresses created from the forces exceed the yield strength of the structures, the load becomes destructive and deformation occurs (Shepherd, 2007).

Stress (σ) is defined as force per unit area, and hence the magnitude of the forces that act on and causes deformation of structural objects.

$$\sigma = \frac{F}{A} \quad \left[\frac{N}{m^2} = Pa \right] \quad (2.1)$$

There are different types of stresses, depending on how the forces act on an object or structure. *Tensile stress* results from pulling an object, resulting in elongation. Similarly, compression introduces *compressive stress*. *Bulk stress* is a result of forces acting on all sides of an object, and *shear stress* occurs when forces act tangentially relative to the object's surface (Lien & Løvholden, 2001).

The deformation of a structure or object in response to stresses is referred to as strain (ε). Strain describes an object's change in either length (tensile or compressive strain), volume (bulk strain), or geometry (shear strain). Hence strain is a dimensionless number, tensile strain is defined as (Lien & Løvholden, 2001):

$$\varepsilon = \frac{\Delta L}{L} \quad (2.2)$$

Up to the materials elastic limit, the relation between stress and strain is linear according to Hook's law:

$$F_s = k * \Delta L \quad (2.3)$$

where F_s is the force needed to extend or compress a spring, k is the stiffness of the system and ΔL is the compression or elongation of the system.

However, Figure 2.5 illustrates that the linear relationship between stress and strain only applies when stress is sufficiently low. Elasticity is a property that describes how an object will return to its original shape and size when the applied forces are removed. The proportionality constant E that gives the relation between stress and strain is referred to as the elastic

modulus or Young's modulus. Within the elastic area a general equation for the relationship between stress, strain, and the elastic modulus is defined as (Lien & Løvholden, 2001):

$$\sigma = E \times \varepsilon \quad (2.4)$$

As mentioned above, strain is dimensionless, and it follows that the elastic modulus has the same unit as stress. E is the elastic modulus for tensile stress, bulk modulus B for the bulk stress, and shear modulus S for the shear stress. Table 2.1 summarises some characteristic values for the three elastic moduli (Lien & Løvholden, 2001).

Table.2.1. Characteristic values for the elastic moduli (Lien & Løvholden, 2001).

Material	E $\times 10^{10} \text{ N/m}^2$	S $\times 10^{10} \text{ N/m}^2$	B $\times 10^{10} \text{ N/m}^2$
Aluminium	7.0	2.6	7.8
Copper	12.4	4.5	13.1
Glass	5.5	2.3	3.1
Gold	7.9	2.8	16.6
Steel (0.3% C)	20.0	8.1	12.3
Steel (0.6% C)	19.6	8.0	12.1
Bone	0.9	-	-
Concrete	3.0	-	-
Wood	1.3	-	-

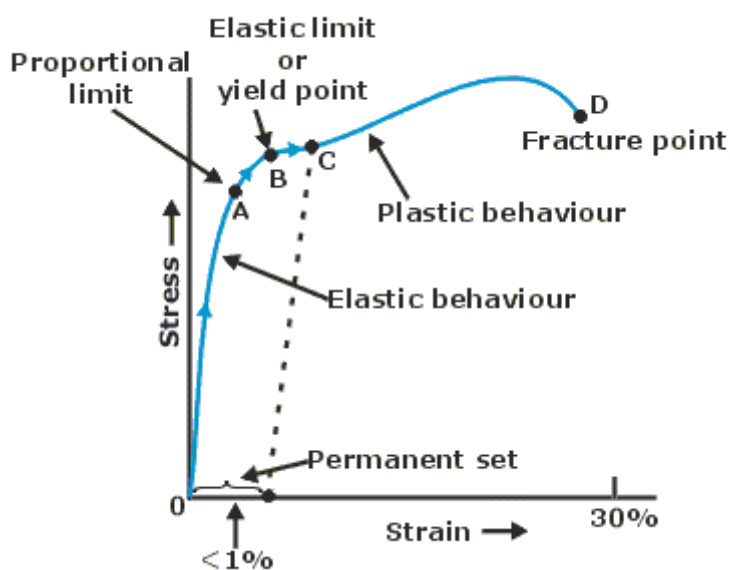


Figure 2.5. A characteristic stress-strain curve.

Beyond the proportionality area on the curve in Figure 2.5, the so-called elastic limit or yield point follows. The yield strength of an object says something about how much stress the object can undergo before it goes from elastic deformation to plastic deformation. Beyond the yield point, the object or material deforms permanently, and Hook's law is no longer valid. If the stress increases further beyond the yield point, a fracture will eventually occur. The maximum stress is referred to as the ultimate tensile strength after this failure will occur at point D. Table.2.2 shows some characteristic values for some elastic properties of some materials (Lien & Løvholden, 2001).

Table.2.2. Characteristic values for elastic properties of some materials (Lien & Løvholden, 2001).

Material	Elastic limit [10^6 N/m^2]	Ultimate tensile strength [10^6 N/m^2]
Aluminium	95	110
Glass	-	50
Steel	250	400
Bone	-	170
Concrete	-	40
Wood	-	50

2.4.2 Reflection

As soon as pressure loads run into a structure or an object (e.g. a wall), an interaction between the wave and the object will occur. This will result in a reflection of the pressure waves (Bjerketvedt, et al., 1997). Pressure loads from an explosion will ideally spread spherically, but when there is an explosion in a confined space or there are obstacles, it will interrupt its path and cause reflections (Doormaal, et al., 2013). Reflection is most relevant for structures subjected to blast waves from high explosives.

Reflection may influence peak overpressures. The loading on a structure exposed to an internal explosion is a complex phenomenon. Different degrees of damage to the structure will depend on the degree of confinement, congestion, material properties, and the resulting peak overpressures. Structures without venting would have to be stronger to resist damage from explosions compared to vented structures because some of the explosion energy will be dissipated through the breaking of windows, weak partitions, or opening of vent panels. Venting reduces peak values of internal pressures and can be very beneficial for protecting the structure against damaging pressure build-up (Cormie, et al., 2009).

Internal congestion or explosions propagating between connected rooms are conditions that may generate turbulence resulting in higher pressures (Ngo, et al., 2007). When explosions in complex geometric structures occur, there will be a reflection in different angles and directions. The load on the structure will depend on the geometric design of the structure, the direction of reflections, the venting of structures, etc. (Johansson & Laine, 2007).

2.4.3 Natural periods and resonance

The natural frequency is the frequency that an object or structure obtains when it oscillates in the absence of any applied force or damping. The time needed to complete one cycle of oscillation is the natural period. The inverse of the natural period (i.e. Eigenperiod) is the natural frequency (Eigenfrequency). The natural period of a structure may change if it is subjected to a pressure load resulting in damage. When a vibrating object or structure is subjected to a force with frequencies close or equal to its natural frequency, it will result in a dramatic increase in the amplitude of the vibrations. This is known as resonance. Even a small force can increase vibration significantly (Arnold, 2006).

2.4.4 Static versus dynamic response

When a structure or an object is exposed to dynamic loading such as an explosion, it will result in dynamic response. Knowledge of the dynamic properties of different structural materials is required to design structures that can withstand the effect of an accidental explosion. Structures and materials respond very differently to static loads, compared with the dynamic loads created by explosions. It is imperative that the designer understands the difference between these loads (ASCE, 2010).

If the load changes very slowly relative to the structure's natural period T or is present during a long period without changing, it is a static or quasi-static load. On the other hand, if the load varies very quickly relative to T , it is a dynamic load (Jansen, et al., 1992). Dynamic means time-varying in this context. The load from a gas explosion is usually dynamic (Bjerketvedt, et al., 1997).

2.4.5 Material

The ability of a structure to withstand applied forces rely on the mechanical properties of the material, such as strength, hardness, ductility, brittleness, and resilience. Hardness is the material's ability to resist permanent deformation, while ductility is the material's ability to deform plastically before it fractures. Metals are fairly ductile materials, and will not fracture as easy as other brittle materials such as glass (Arnold, 2006). Resilience is the material's ability to resume its original shape. Materials respond very differently to static loads compared to dynamic loads. When materials like steel (the focus in this thesis) are under dynamic loading, they achieve an increase in strength, which can improve the resistance of the structure.

Structures subjected to dynamic loads, such as blast waves, usually undergo plastic (permanent) deformation, which results in energy absorption of the explosion energy. Yielding is often accepted in blast design for economic reasons, while the stresses should be limited to the elastic range for conventional design (ASCE, 2010). Design for plastic deformation allows for lighter structures due to energy absorption (Biggs, 1964).

2.4.6 Damping

When a structure undergoes vibration, it will experience decay in its amplitude, and the oscillation will eventually cease. This decay in amplitude or damping is due to energy absorbed by internal friction. Different materials and structures will affect the damping. Heavy concrete structures will result in more damping than a lighter steel frame structure (Arnold, 2006).

2.5 SDOF-system

The single degree of freedom (SDOF) system is a basic analytical model that is used in most blast-resistant designs. It is often used to calculate the displacement of the centre of a structure such as a beam, a column, or a wall. Various structures can adequately be represented by an SDOF system for analysis, even though in reality all structures have more than one degree of freedom. Figure 2.6 shows a simple system with a mass connected to a spring and a damper. The mass is only allowed to move in one direction, and it is therefore called a single degree of freedom system. Considering dynamic equilibrium, the linear elastic SDOF system illustrated in Figure 2.6 can be expressed by the equation of motion as follows:

$$Ma + Cu + ky = F(t) \quad (2.6)$$

where: M = mass

a = acceleration

C = viscous damping constant

u = velocity

k = stiffness

y = displacement

F = blast force or applied force

t = time

The forces acting on the mass are the inertial force, Ma , the damping force, Cu , the resistance, ky , and the applied force, F . In blast design, damping is typically ignored because of the short rise time to maximum response. Damping effects will therefore have an inconsequential effect on the maximum displacement (ASCE, 2010).

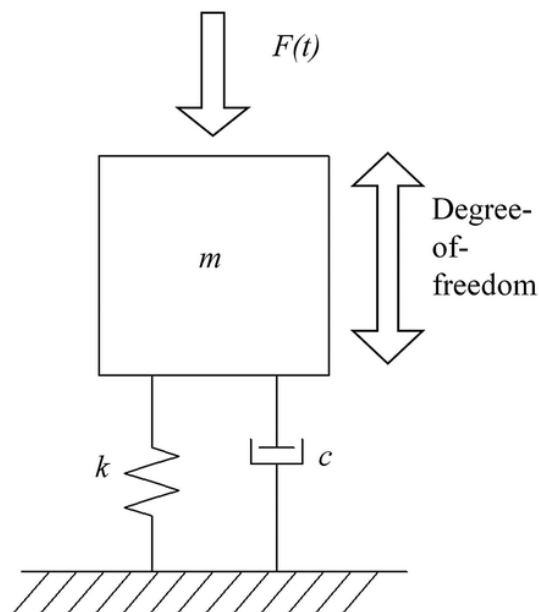


Figure 2.6. Illustrated damped SDOF model for dynamic analysis.

The system above is a linear elastic system where the resistance function is a straight line with slope K and no upper limit. For many practical situations, this is not the case. The function may be nonlinear, which implies that the slope is not constant and/or inelastic, which means that when the load is removed from the spring the resistance does not necessarily return to zero following the same path. This is a one-degree-of-freedom elastic-plastic system (Biggs, 1964). A numerical solution can be found by extending the elastic one-degree-of-freedom spring-mass system. This is done by replacing the elastic spring force, Ky , by resistance force, R , which is any general function of the displacement (Baker, et al., 1983). Inelastic behaviour is normally assumed in structural design where the dynamic response of a structure goes from the elastic range and into the plastic range. Figure 2.7 illustrates the idealized situation where the resistance increases linearly with the slope of k as the displacement increase until the elastic limit of displacement y_{el} is reached. The maximum resistance R_m is assumed to remain constant until the structure's ductility limit is reached. If the displacement of the structure reaches its maximum before this limit and decreases, it will "bounce back". The resistance is then assumed to decrease with a line parallel to the elastic slope. This resistance function is as mentioned only an idealization, and this function will have curved transitions for real structures (Biggs, 1964).

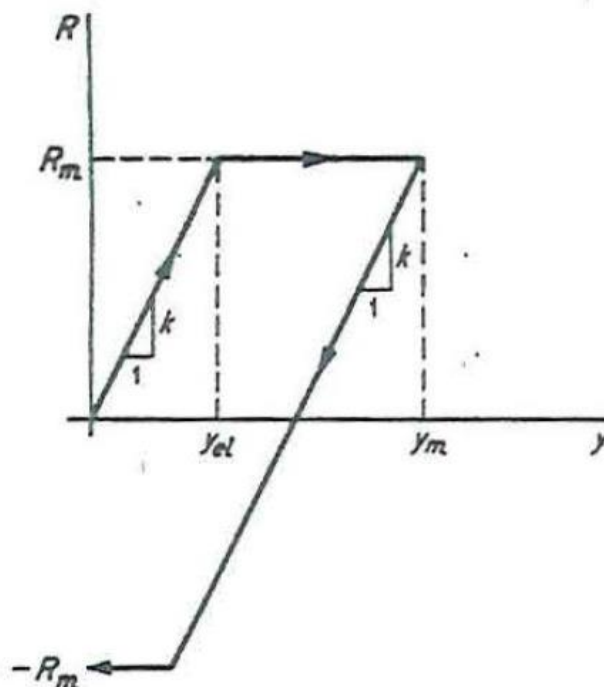


Figure 2.7. Idealized resistance function (Biggs, 1964).

2.6 Finite element method

The finite element method (FEM) is widely used for problems in structural analysis when the physical phenomenon consists of complex geometries, material properties, or loadings. Analytical solutions are generally not attainable for such problems. FEM is a numerical method that solves engineering problems described by partial differential equations. This method divides larger systems into smaller systems to solve a specific problem. These smaller parts are called finite elements and are achieved by the construction of a computational mesh. Equations for each finite element is formulated and combined to achieve the solution of the whole system. Simulating physical phenomenon is widely used to analyse the structural response and this simulation or analysis is referred to as finite element analysis (FEA) (Logan, 2012).

2.7 P-I diagrams

Pressure-impulse (P-I) diagrams can be used to evaluate the level of damage a specific structure obtains when subjected to a specific load. P-I diagrams can be divided into regions by several P-I curves each representing a certain level of damage (e.g. permanent deformation) (Skjold, et al., 2019c). The area under the pressure-time history curve is defined as the impulse (Krauthammer, et al., 2008). An idealised pressure-time curve for confined gas or dust explosions are illustrated in Figure 2.8. The relationship between pressure and impulse can be found by numerical or analytical methods. Figure 2.9 illustrates a typical P-I curve for a blast load. If the combination of pressure and impulse is located to the left and below the curve there will be less damage, while to the right and above the curve there will be more

damage (Cormie, et al., 2009). The level of damage will increase as pressure and impulse increase (Baker, et al., 1983).

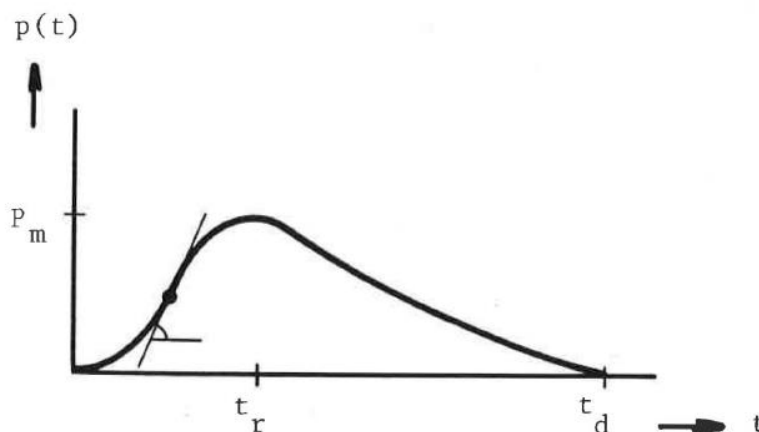


Figure 2.8. Idealised pressure-time history for typical confined gas or dust explosions (Baker, et al., 1983).

Figure 2.9 and Table 2.3 summarize the strong relationship between the structural response and the ratio of the load function, t_d , to the natural period of the structure, T , which can be classified into three regimes: impulsive loading regime, dynamic loading regime, and quasi-static loading regime (Krauthammer, et al., 2008). The maximum response can depend on either the applied impulse (impulsive region), the pressure (quasi-static region), or on both the pressure and the impulse (dynamic region). In the *impulsive loading regime*, the duration of the load is very short relative to the structure's natural frequency and the maximum structural response is therefore not reached before the duration of the load is over. This creates the vertical impulsive asymptote which defines the minimum impulse that is required to reach a particular level of damage. In the *quasi-static loading regime*, the duration of the load is substantially longer relative to the structure's natural frequency and the maximum structural response is reached before the applied load is removed. This creates the horizontal pressure asymptote which defines the minimum peak overpressure that is required to reach a particular level of damage. In the *dynamic loading regime*, the maximum response is reached close to the end of the loading regime and the structural response is more complex and influenced by the load history profile (Abedini, et al., 2018; Shi, et al., 2008).

Table.2.3. The three regimes of blast loading (Cormie, et al., 2009).

$\frac{t_d}{T} < 0.1$	Impulse loading
$0.1 < \frac{t_d}{T} < 10$	Dynamic loading
$\frac{t_d}{T} > 10$	Quasi-static loading

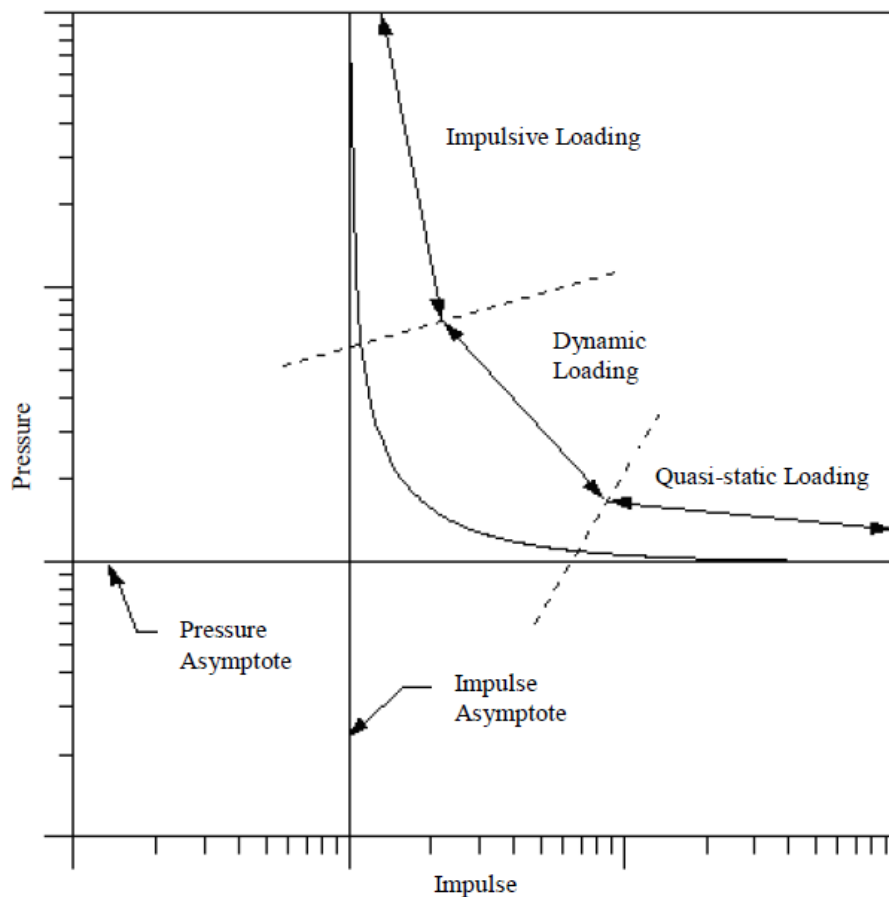


Figure 2.9. Illustration of a typical pressure-impulse curve for loading with short rise time (Shi, et al., 2008).

P-I diagrams are significantly influenced by the shape of the pulse load (e.g. possible oscillation), the rise time of the load, plasticity, damping, the structure's geometry, and material properties (Abedini, et al., 2018; Skjold, et al., 2019c). P-I diagrams are often derived for ideal blast loads and Baker et al. (1983) emphasised that there is a significant difference between the structural loading caused by internal gas or dust explosions, compared to structural loading caused by condensed explosives. Ideal blast waves produced by condensed explosives or other detonations have near-zero rise time, and the decay is near exponential. On the other hand, non-ideal blast waves caused by gas, vapour, or dust explosions (i.e. vented deflagrations) have finite rise time. Non-ideal explosions may display multiple pressure peaks. Loading with finite rise time will result in more severe damage than loading with zero rise time due to the resonance between the natural frequency of the structure and the rate of the load (Baker, et al., 1983; Skjold, et al., 2019c).

3 The HySEA project

This thesis will use empirical results from the HySEA project. The experimental program included two experiment campaigns with vented hydrogen deflagrations in 20-foot shipping containers. The experiments were performed during the period from September 2016 to February 2018 on the Gexcon test site on Sotra, an island outside Bergen. The background, experimental procedures, and the results of this project are described in further detail by Skjold (2018a).



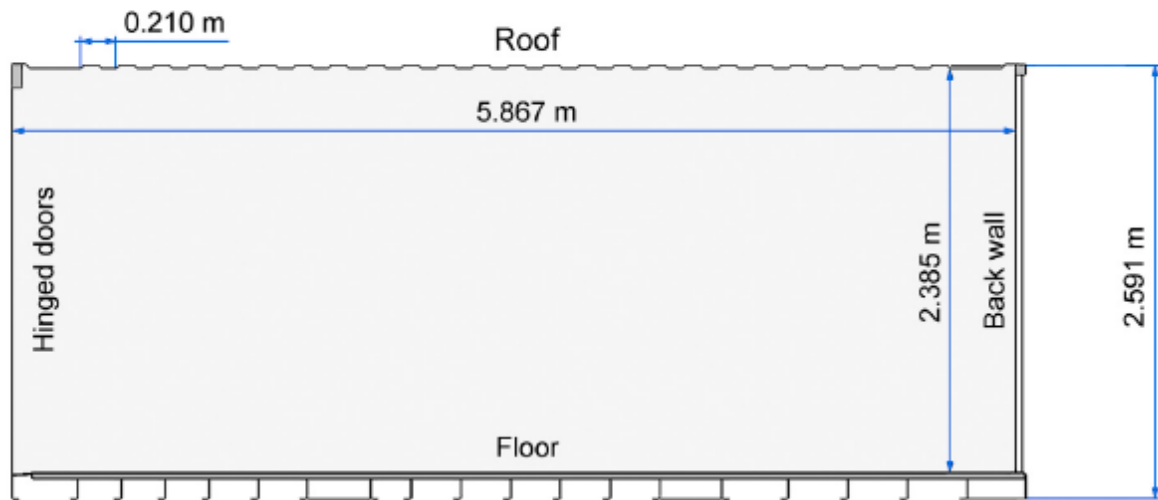
Figure 3.1. One of twelve 20- foot ISO containers before testing (Skjold, et al., 2019b).

Figure 3.1 shows one of the twelve 20-foot ISO containers before testing. Figure 3.2 summarises the main dimensions of the containers. Plywood covered the floor of the containers while the walls and the roof were made from 2 mm thick corrugated steel plates. The depth and length of the corrugation were around 35 mm and 280mm, 16 mm, and 210 mm, for the walls and roof respectively (Skjold, et al., 2019b).

Figure 3.3 illustrates the location of the vent openings, either through the door or the roof. The same figure shows the three different locations for obstacles (1-3) and the ignition source. The obstacles that were used were either a bottle basket (BB) or a pipe rack (PR). The locations for the ignition source were back wall centre (bc), back wall upper (bu), or floor centre (fc).

The illustration on the right in Figure 3.3 shows a 3D illustration of a container with frame only (FO) and a container with a bottle basket located in the inner position (BB1) (Skjold, et al., 2019a).

Side view:



Top view:

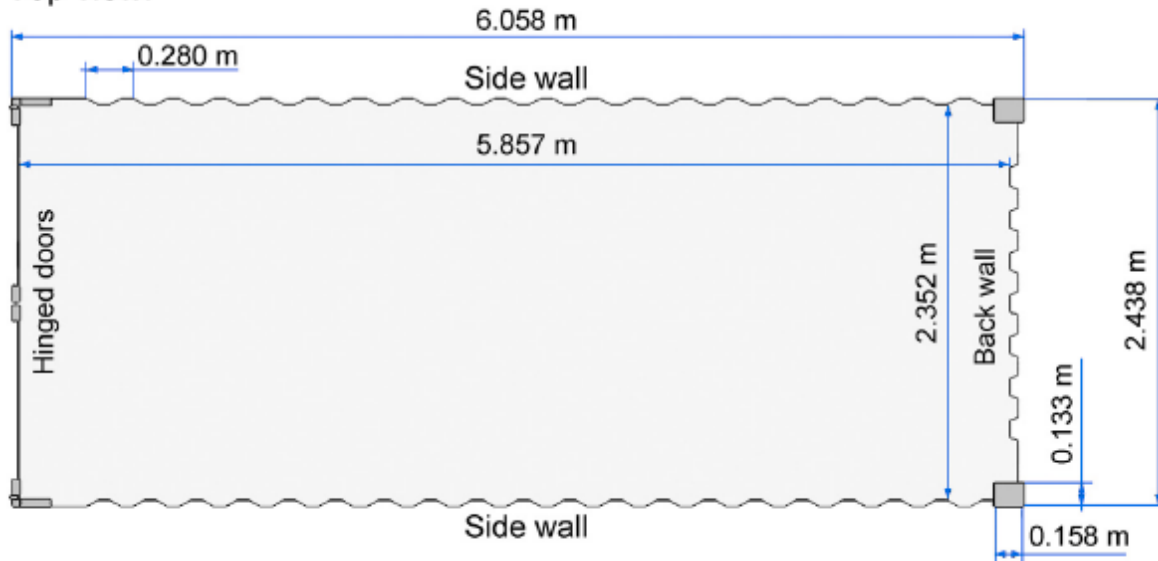


Figure 3.2. Main dimensions of the 20-foot ISO containers (Skjold, et al., 2019b).

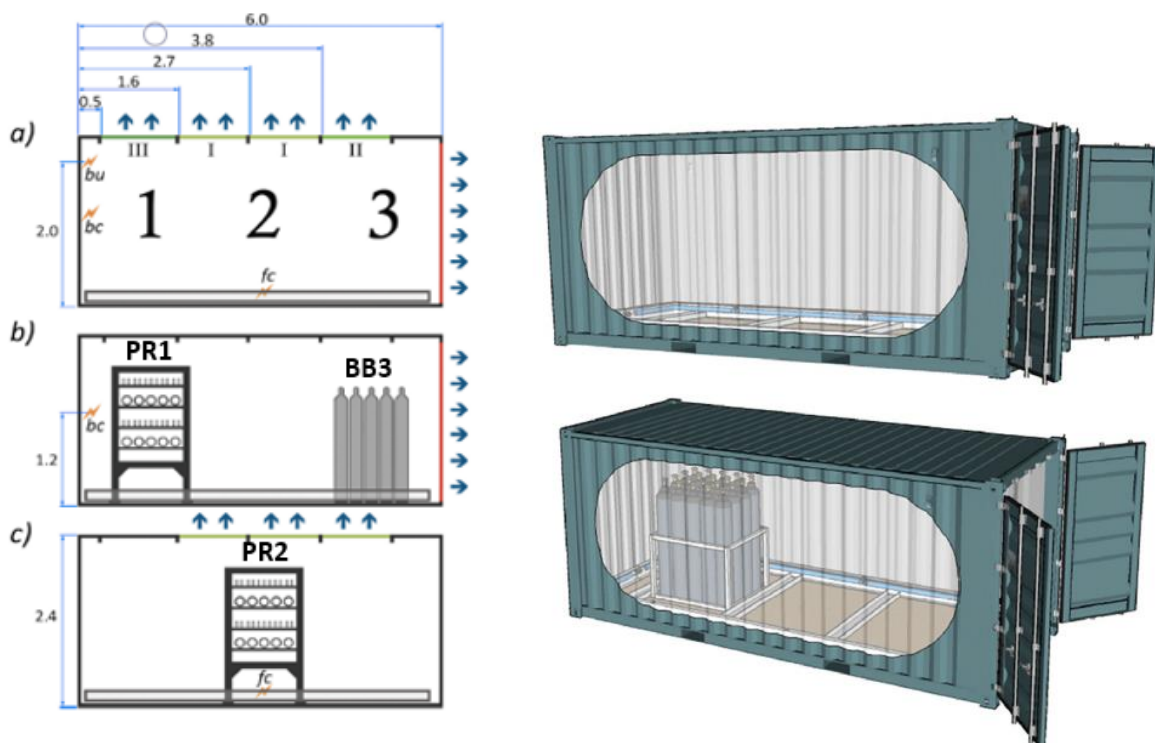


Figure 3.3. Location of vent openings, obstacles, and ignition locations (left), and 3D model with bottle basket in inner position (right) (Skjold, et al., 2019b).

Figure 3.4 shows the location of the eight piezoelectric sensors that measured the internal. The dynamic deflection of the two side walls was measured by laser displacement sensors located near the centre of each side wall (Skjold, et al., 2019c). More detailed information about the measurement system can be found in Skjold (2018a).

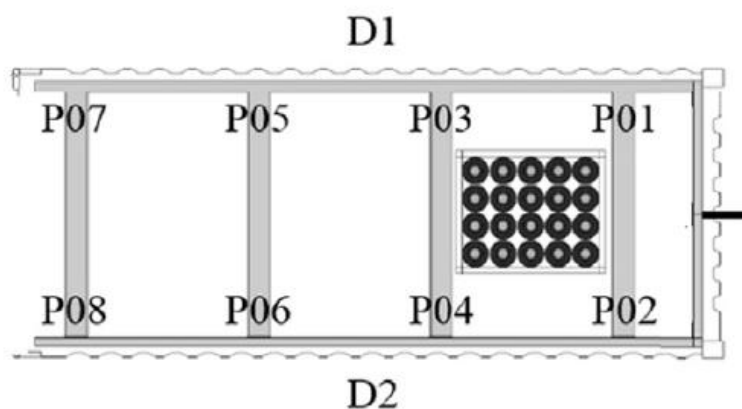


Figure 3.4. Position of the sensors that measured internal pressures (P01-P08) and wall deflection (D01-D02). The container doors are located on the (Skjold, et al., 2019a).

Skjold et al. (2019c) constructed empirical P-I diagrams for 20-foot shipping containers subjected to internal hydrogen deflagrations using the permanent deformation of the walls as the damage criterion. Figure 3.5 illustrates a simplified P-I diagram for ideal blast loads with zero rise time (left), and a modified diagram for loading with finite rise time (right). All the experimental results fall within the dynamic loading regime apart from the quasi-static test result. Uncertainties such as complex pressure loading histories and influence of permanent deformation from previous tests influence the result significantly.

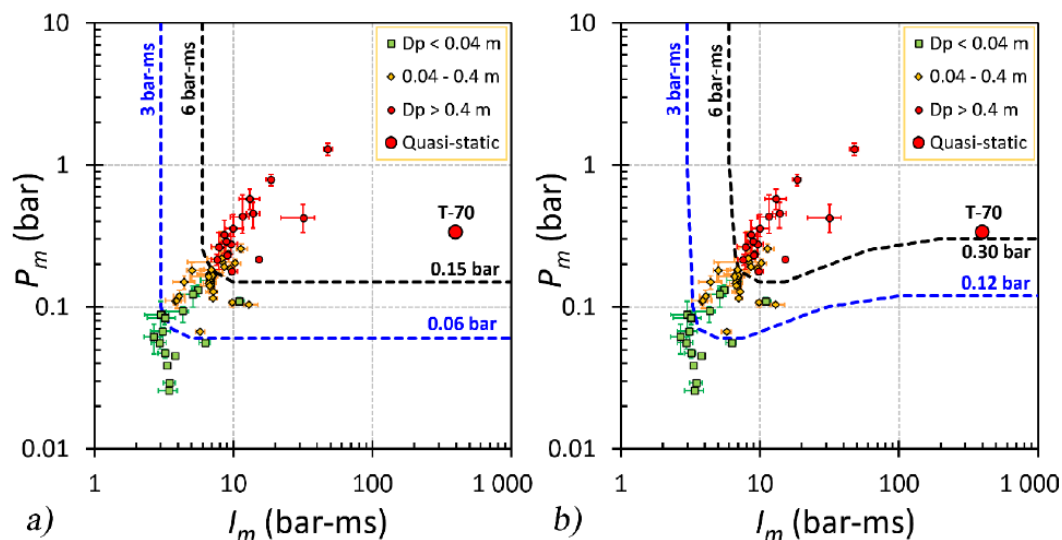


Figure 3.5. Simplified (left) and modified (right) empirical P-I diagrams (Skjold, et al., 2019c).

4 Literature review

This chapter presents a literature review that is focused on the development of P-I diagrams. The following studies were primarily carried out for blast loads with near-zero rise time on simple structural elements such as beams, columns, and walls. Various methods can be used to derive P-I diagrams for structures that are subjected to blast loads. Including analytical methods (SDOF and energy balance method), numerical methods, and experimental methods (Abedini, et al., 2018).

4.1 Analytical method for generating P-I diagrams

Oswald & Skerhut (1994) developed a simple hyperbolic function for reinforced concrete slabs that produce curve fitting for a linearly elastic flexural model using the energy balance method:

$$(P - A)(I - B) = 0.4\left(\frac{A}{2} + \frac{B}{2}\right)^{1.5} \quad (4.1)$$

Krauthammer et al. (2008) proposed an approximate equation for a perfectly flexural elastic SDOF system that has been subjected to either rectangular or triangular pulses by modifying Equation 4.1:

$$(P - A)(I - B) = C(A + B)^D \quad (4.2)$$

where A is the impulsive asymptote, B is the quasi-static asymptote and C and D are approximate constant values.

Shi et al. (2010) expressed another curve fitting equation for the damage to reinforced concrete (RC) columns with flexural failure similar to the previous two (Equation 4.3). P_0 and I_0 are the pressure and impulse asymptotes, respectively.

$$(P - P_0)(I - I_0) = 12\left(\frac{P_0}{2} + \frac{I_0}{2}\right)^{1.5} \quad (4.3)$$

Xu et al. (2014) used a single degree of freedom (SDOF) system for reinforced concrete (RC) slabs to predict the shear response to external blast loads. Dynamic response equations for a structural member that experienced direct shear failure were derived for elastic, plastic, and elastoplastic shear resistance-slip models. Xu et al. (2014) used the curve fitting Equation 4.4

as a simplified method to obtain P-I diagrams for the direct shear failure of RC slabs subjected to external blast loads. P_0 and I_0 are the pressure and impulse asymptotes found by the SDOF method. The constants n_1 and n_2 are related to the configuration of the RC slab that was estimated from the assessment of the RC slab (Xu, et al., 2014).

$$(P - P_0)(I - I_0) = n_1 \left(\frac{P_0}{2} + \frac{I_0}{2} \right)^{n_2} \quad (4.4)$$

Xu et al. (2014) used parametric studies based on the elastoplastic model to generate formulae for the pressure and impulse asymptote to evaluate the accuracy of Equation 4.4. Changing parameters of the RC slabs such as the span length, the concrete reinforcement ratio, thickness, concrete, and steel strength were explored to see the effect on the P-I curve. The analytical formulae for the pressure and impulse asymptotes of the elastoplastic model were:

$$P_0 = 10000 \times \left[0.0055 \times \exp\left(\frac{f^c}{30}\right) + 0.012 \times \exp\left(\frac{fy}{300}\right) + 0.048 \times \exp\left(\frac{\rho}{0.03}\right) + 0.017 \times \left(\frac{L}{1000}\right)^2 - 0.18 \times \left(\frac{L}{1000}\right) - 1.03 \times \left(\frac{h}{200}\right)^3 + 3.11 \times \left(\frac{h}{200}\right)^2 - 2.45 \times \left(\frac{h}{200}\right) + 0.80 \right] \quad (4.5)$$

$$I_0 = 0.026 \times \exp\left(\frac{f^c}{30}\right) + 0.039 \times \exp\left(\frac{fy}{300}\right) + 0.22 \times \ln\left(\frac{\rho}{0.03}\right) + 0.054 \times \left(\frac{L}{1000}\right)^2 - 0.56 \times \left(\frac{L}{1000}\right) + 0.058 \times \left(\frac{h}{200}\right)^2 + 1.59 \times \left(\frac{h}{200}\right) + 0.72 \quad (4.6)$$

The parameters used in these formulae are concrete strength f^c , steel strength fy , reinforcement ratio ρ , slab span L , and slab depth h . The P-I curves can then be generated by substituting P_0 and I_0 into equation 4.4. The accuracy of Equations 4.5 and 4.6 can be tested by comparing the values of P_0 and I_0 to values obtained by using SDOF. Xu et al. (2014) compared their values and found a difference in P_0 within 6% and less than 10% for I_0 . Hence, Equations 4.5 and 4.6 generates reasonable estimations of the asymptotes (Xu, et al., 2014).

Fallah & Louca (2007) proposed equations for pressure (quasi-static) and impulse asymptotes after studying the effect of material softening and hardening on P-I diagrams:

$$\frac{F_m}{Ky_m} = \alpha(1 - \theta\psi^2) + \frac{\theta}{2}(\psi^2 - \theta\alpha^2 + \alpha^2\psi^2) \quad (4.7)$$

$$\frac{I}{y_m \sqrt{KM}} = \sqrt{2\alpha(1 - \theta\psi^2) + \theta(\psi^2 - \theta\alpha^2 + \alpha^2\psi^2)} \quad (4.8)$$

where I is the impulse, y_m is the maximum deflection of the structure, K is the elastic stiffness, M is the lumped mass of the SDOF system and F_m is the maximum force applied to the system. The dimensionless parameters α , ψ , and θ are defined as following $\alpha = \frac{y_{el}}{y_c}$, $\psi^2 = \frac{K\beta}{K}$ and $\theta = +1$ for elastic-plastic hardening and -1 for softening.

Li & Meng (2002) generated expressions for P-I curves from dimensionless parameters:

$$i = \frac{I}{y_m \sqrt{KM}} \quad (4.9)$$

$$p = \frac{F_m}{Ky_m} \quad (4.10)$$

where i and p are the scaled impulse and scaled pressure and the rest of the parameters are the same as the ones used above in Eqs. 4.7 and 4.8 (Li & Meng, 2002).

Baker et al. (1983) suggested the following formula for non-ideal explosive loading typical for gas or dust explosions:

$$p(t) = P_m \left[\frac{t}{t_r} - \frac{1}{2\pi} \sin \frac{2\pi t}{t_r} \right] \quad t \leq t_r \quad (4.11)$$

$$= P_m \left(1 - \frac{t-t_r}{t_d-t_r} \right) e^{-\left(\frac{t-t_r}{t_d-t_r}\right)} \quad t_r \leq t \leq t_d \quad (4.12)$$

where P_m is the maximum overpressure, t is the time, t_r is the pressure rise time and t_d is the pressure pulse duration in case of venting. Figure 2.8 illustrates an idealised pressure-time curve for confined gas or dust explosions.

According to Baker et al. (1983), a one-degree-of-freedom, elastic-plastic, spring-mass system can be used to evaluate the influences of the shape of the load on the structural response and finite rise time. Baker et al. (1983) replaced the pressure P with the force P^* in the analysis:

$$\bar{P} = \frac{P^*}{KX_{max}} \quad (4.13)$$

$$\bar{I} = \frac{I}{X_{max}\sqrt{KM}} \tag{4.14}$$

Figure 4.1 shows a comparison between a non-ideal (B) explosion and an ideal explosion (A).

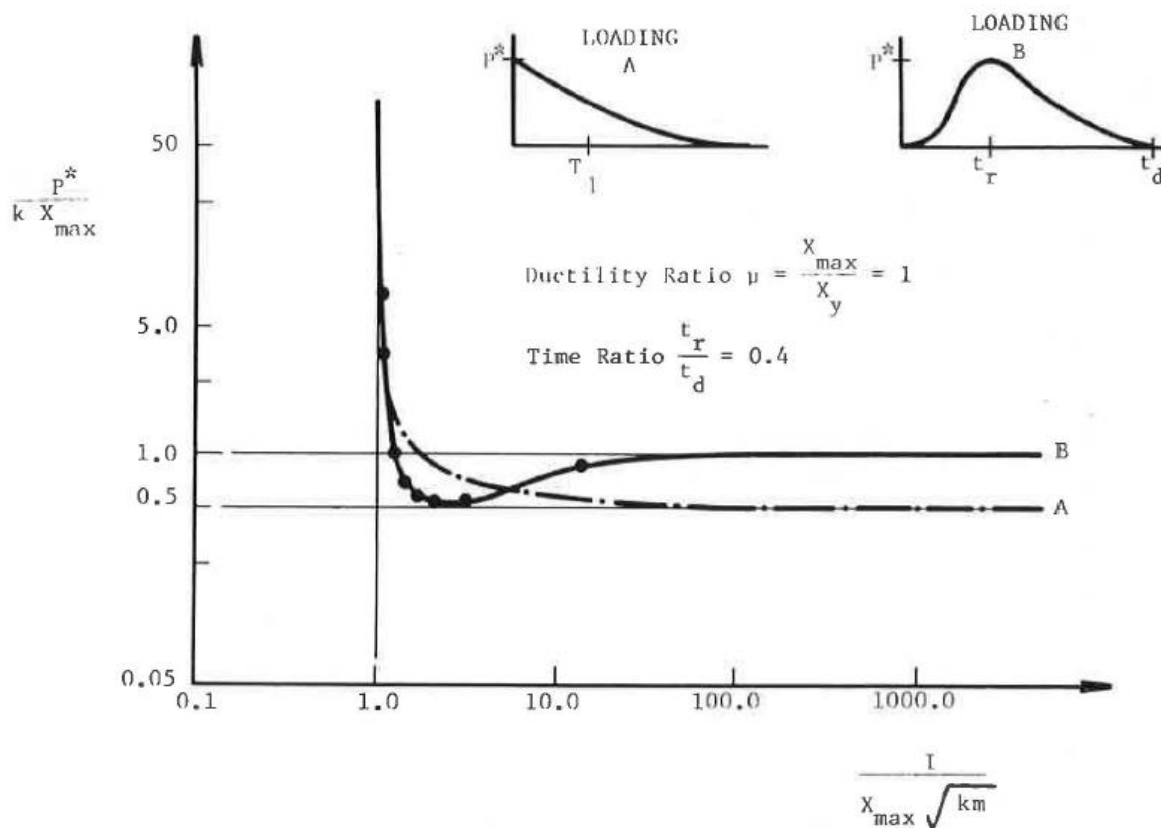


Figure 4.1. P-I diagram for an ideal (A) and a nonideal (B) explosions (Baker, et al., 1983).

Analytical methods to generate P-I diagrams are limited to simple structures, resistance models, and load functions (Krauthammer, et al., 2008). As mentioned by Krauthammer et al. (2008), numerical approaches are required for more complex problems.

4.2 Numerical methods for generating P-I diagrams

Krauthammer *et. al* (2008) pointed out that numerical methods represent the only reasonable approach for deriving P-I diagrams for complex incidents where the load pulse is irregular, or the resistance function is nonlinear.

Rhijnsburger et al. (2002) presented a method that combined the energy balance method to estimate the pressure and impulse asymptotes with numerical analysis to generate the

dynamic regime utilizing a branch-tracing technique. Figure 4.2 illustrates this technique. A prediction point is made by extrapolating the slope from two known points. With the predicted P-I combination, a response calculation can provide the ductility of the system (i.e. ratio between the maximum displacement and the yield displacement). Correction steps are performed to find the next point when the predicted point is not in agreement with the specified ductility until the ductility is found within a reasonable area of the failure criterion. This method could become unstable because of the assumptions included in the algorithm that the P-I curve is continuous and smooth, the time discretization in the numerical method might violate these assumptions and the slope may encounter abrupt changes (Krauthammer, et al., 2008).

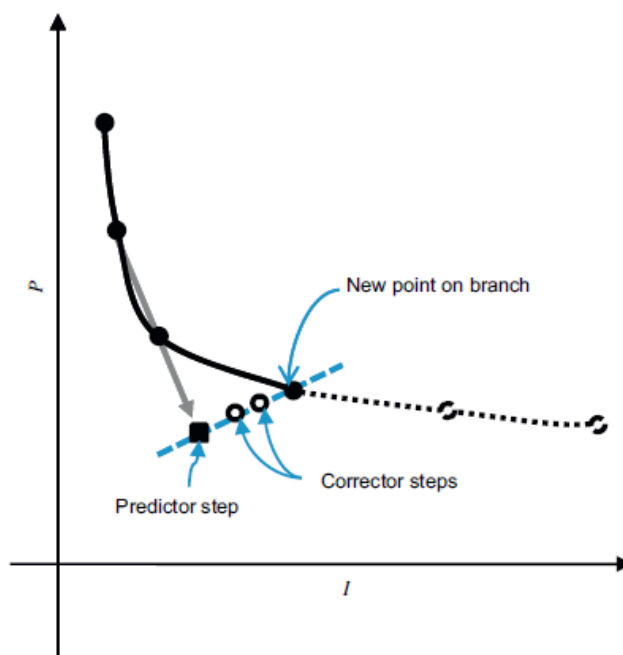


Figure 4.2. Illustration of the branch-tracing technique (Rhijnsburger, et al., 2002).

Soh & Krauthammer (2004) investigated reinforced concrete beams, idealized as two SDOF systems. Their method for generating numerically stable P-I diagrams utilized the combination of the energy balance method to estimate the pressure and impulse asymptotes and a large number of dynamic analyses that were assessed within the limits of these asymptotes. This search algorithm reduced these limits until a threshold curve was developed. Figure 4.3 illustrates this numerical algorithm for this method.

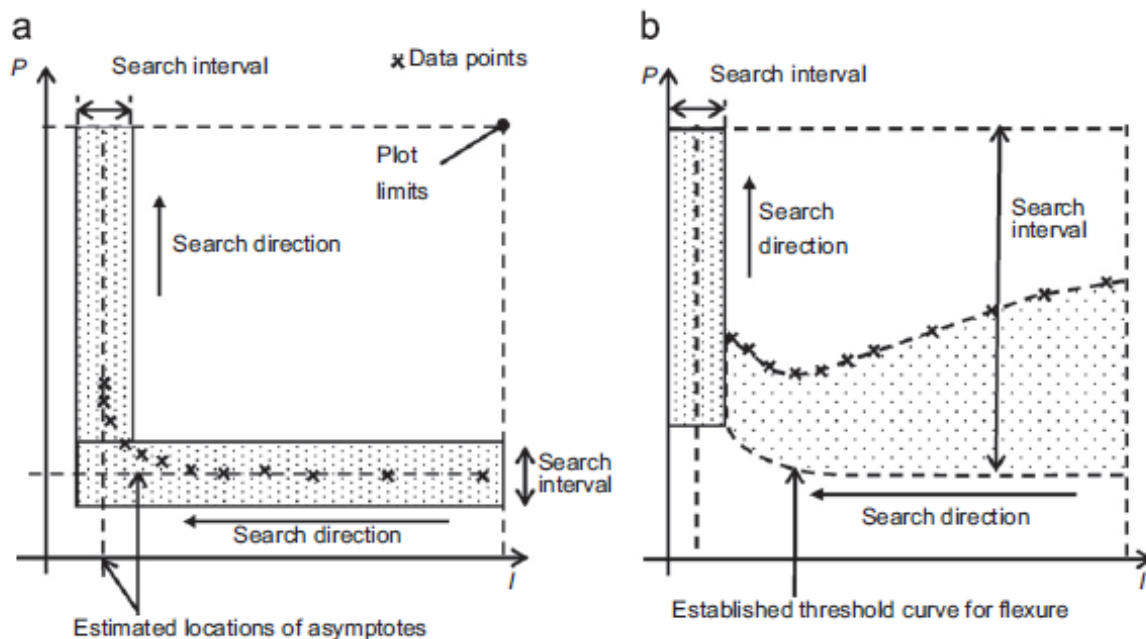


Figure 4.3. Illustration of the search algorithm by Soh & Krauthammer (2004): flexure (a) and direct shear (b).

Ng & Krauthammer (2004) used a numerical method to generate P-I curves that did not depend on the asymptotes. They researched reinforced concrete slabs idealized as two SDOF systems to examine the direct shear and flexural behaviours. The basis of this algorithm is the definition of a threshold curve. By keeping the pressure constant, threshold points are found by checking if several combinations of pressure and impulse are either “safe” or “damaged”. If the result of the combination is safe, it will carry on by increasing the impulse until the result of the point is damaged. If the result is damaged, the impulse is reduced. A threshold point is found between these two boundaries, illustrated in Figure 4.4 (Krauthammer, et al., 2008).

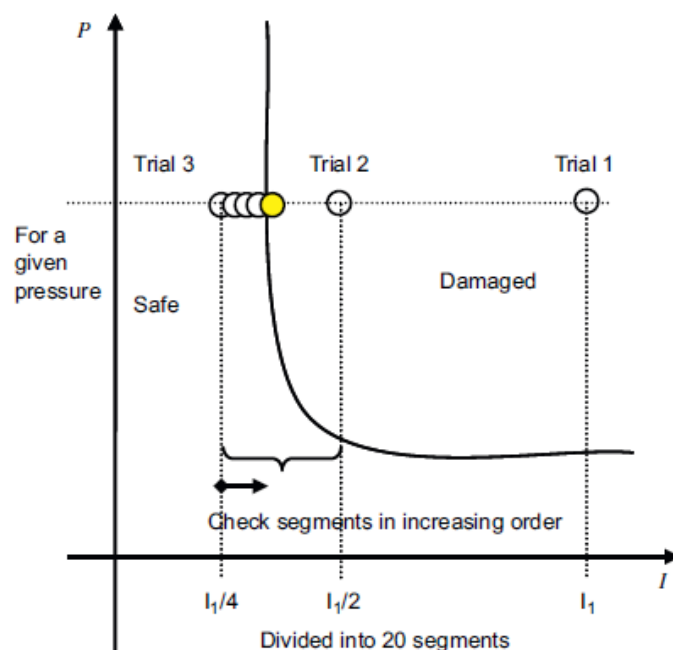


Figure 4.4. Illustration of the numerical search algorithm by Ng & Krauthammer (2004).

Krauthammer et al. (2008) pointed out that the numerical methods presented by Soh & Krauthammer (2004) and Ng & Krauthammer (2004) generated fairly accurate P-I curves. However, both these algorithms include a few shortcomings. They entail a lengthy computational process, generate a substantial amount of unnecessary data, and are computationally intensive. These methods are also case-specific since Soh & Krauthammer (2004) limited their numerical analysis to reinforced concrete beams exposed to localized impact loads, and Ng & Krauthammer (2004) limited their numerical analysis to reinforced concrete slabs exposed to uniformly distributed blast loads (Krauthammer, et al., 2008).

Blasko et al. (2007) developed another numerical method where a bisection method and a polar coordinate system was used to generate P-I diagrams. Running all possible combinations of pressure and impulse will be computationally very expensive, so to avoid this, Krauthammer et al. (2008) mentioned that a search algorithm should be used to find threshold points that divide the safe and unsafe regions from each other (Colombo & Martinelli, 2012). This numerical method developed by Blasko et al. (2007) entails locating a pivot point (I_p, P_p) in the failure zone and setting it as the origin of the polar coordinate system, shown in Figure 4.5. For each angle, ϑ_i , the radius, R_i , to the threshold point is found by iterations utilizing the bisection method.

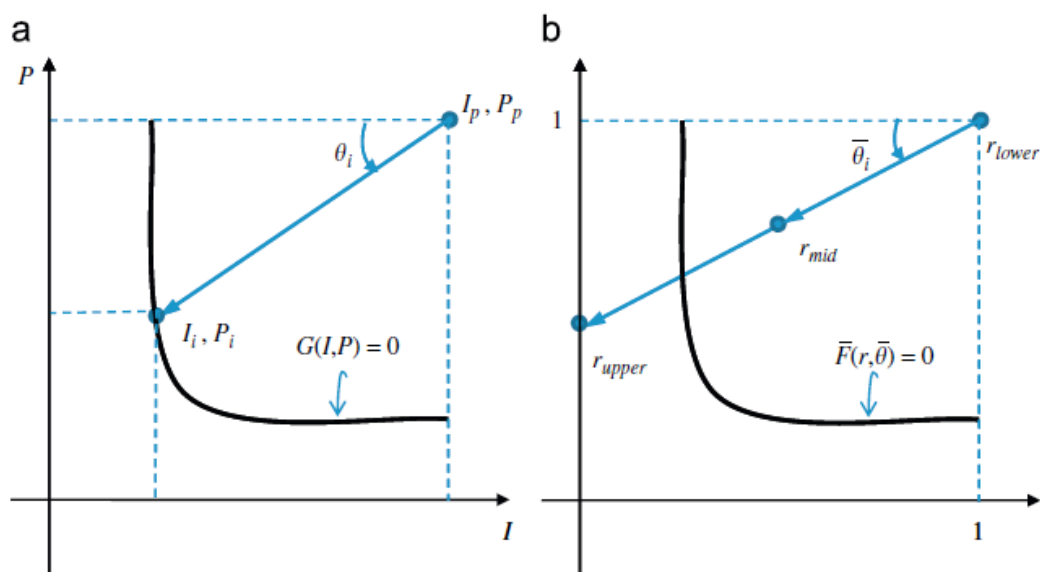


Figure 4.5. Illustration of the search algorithm by Blasko et al. (2007): establish a pivot point (a) and data pivot search (b).

Instead of using two search directions (horizontal and vertical), this method uses a single radial search direction. This method is also independent of computed asymptotes. However, asymptotes can be utilized to locate suitable pivot points which can automate this method (Krauthammer, et al., 2008). Figure 4.6 shows an ideal pivot point located on the line that passes the intersection of the asymptotes and the origin of the P-I diagram. Points along this line are expected to be located at the same distance from each asymptote (Colombo &

Martinelli, 2012). The resolution of the result can be reduced if the pivot point is randomly selected because this point could either be too close to one of the asymptotes or too close to the threshold curve. This method is not restricted to one specific system and can be used for several structural systems as long as a resistance function can be obtained (Krauthammer, et al., 2008).

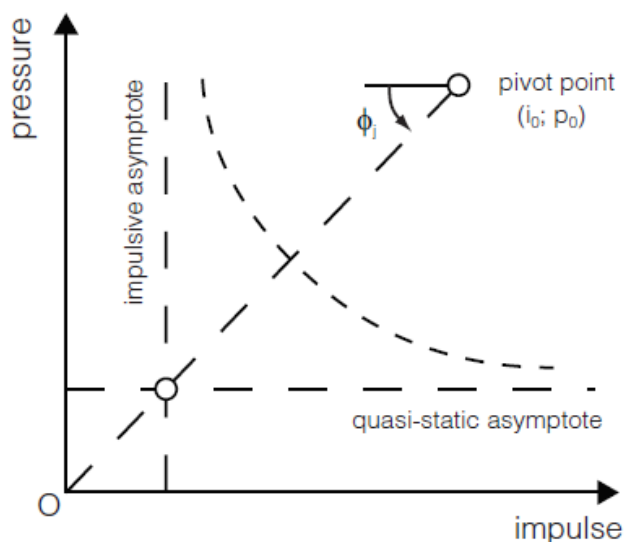


Figure 4.6. Illustration of the search algorithm and location of the pivot point (Colombo & Martinelli, 2012).

Krauthammer *et al.* (2008) investigated the influence of the rise time on P-I curves for reinforced concrete beams (a perfect elastic system). This showed that the impulse response was not affected. However, Figure 4.7 shows how the pressure response will fluctuate considerably, depending on the ratio of the rise time, t_r , and load duration, t_d . The quasi-static or pressure asymptote will move to higher values, in this case from 0.5 to 1 as the ratio increases. When the quasi-static asymptote is equal to 1, it is equivalent to a static load, and hence no dynamic development (Krauthammer, et al., 2008).

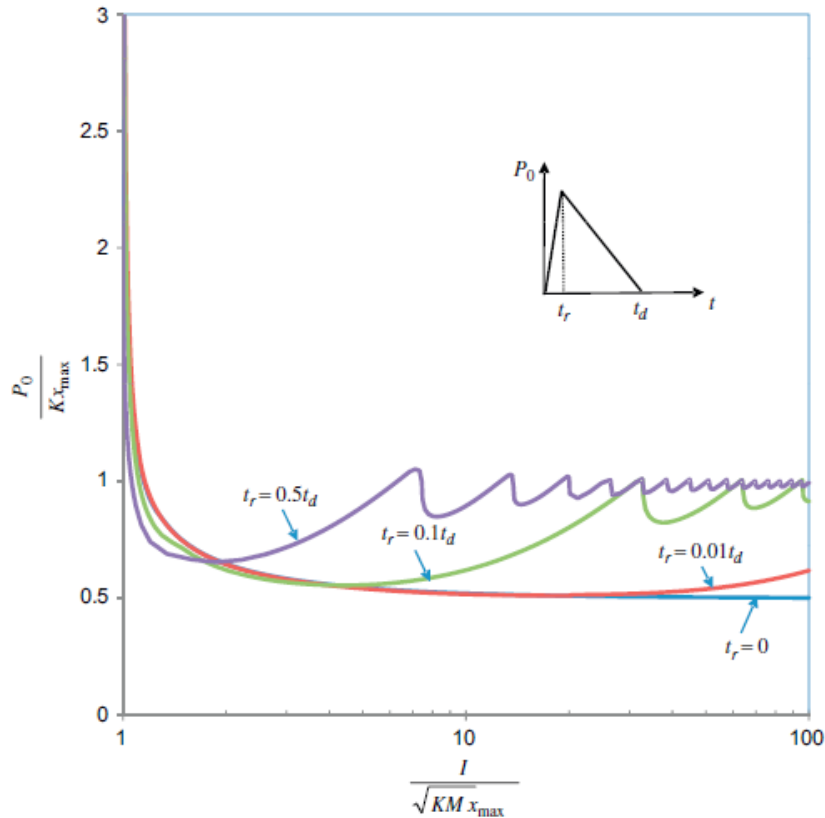


Figure 4.7. Influence of the rise time on the P-I curve (Krauthammer, et al., 2008).

4.3 Experimental methods for generating P-I diagrams

Experimental testing of structures subjected to pressure loads requires comprehensive preparations and can be very expensive (Abedini, et al., 2018). Parlin et al. (2014) utilized both experimental and numerical methods to assess the structural response of lightweight flexible wall panels. They subjected the wall panels to static bending in their experimental test. P-I diagrams were developed based on maximum deflection damage criterion, and both linear and nonlinear dynamic analyses were used. They concluded that a nonlinear SDOF dynamic model was a reasonable model to represent the blast response of the wood-based wall panels (Abedini, et al., 2018).

Wang et al. (2013) generated P-I diagrams for reinforced concrete slabs subjected to blast loads by utilizing two loosely coupled SDOF models. The result of their blast test showed that incorporating the strain rate effect that is caused by rapid application of the load, improved the SDOF systems ability to predict the failure modes of the slab. To generate P-I diagrams they proposed the following analytical formula:

$$(P - P_0)(I - I_0)^n = 0.33\left(\frac{P_0}{2} + \frac{I_0}{2}\right)^{1.5} \quad (4.15)$$

In their study, they evaluated the effect of different parameters, such as the span length of the slab and the concrete reinforcement ratio, on the P-I diagram for two failure modes. From the results, they observed that the slab tends to fail in direct shear mode when the span length is smaller, and in flexure mode when the span length is larger. They also observed an increase in shear and flexure capacity when there is an increase in either the concrete strength or the reinforced ratio (Abedini, et al., 2018).

Empirical P-I diagrams presented in chapter 3 were produced by Skjold et al. (2019c) using experimental data from the HySEA project for vented hydrogen deflagrations in 20-foot shipping containers. In this thesis, the P-I diagrams were produced numerically using the non-linear explicit finite element program Impetus Afea.

5 Methodology

The Impetus Afea Solver is a non-linear explicit finite element program that can be used to analyse the structural response of an object subjected to a load. The formulation of the solver is Lagrangian and suitable for processes where objects undergo extreme deformations. The solver is based on explicit time integration and can utilize GPU (graphics processing unit) for high-computational speed. All calculations are performed with double precision resulting in high accuracy. Even if the mesh is highly distorted, the higher-order element leads to high accuracy (Salaün, et al., 2016).

5.1 Methodology for generating numerical P-I diagrams using the Impetus Afea Solver

This section describes how the Impetus Afea Solver was used to generate P-I diagrams for 20-foot shipping containers exposed to internal pressure loads. The model and geometry for the container were provided by Impetus Afea.

5.1.1 Background

It is not straightforward to create P-I diagrams for 20-foot shipping containers subjected to internal pressure loads from hydrogen deflagration. The duration of the actual event is in the order of seconds, while the simulation time for a single event can be in the order of weeks. It is therefore not realistic to base the analysis on a detailed 3D model of a 20-foot container. Therefore, a simplified model is preferable (Hanssen, 2020).

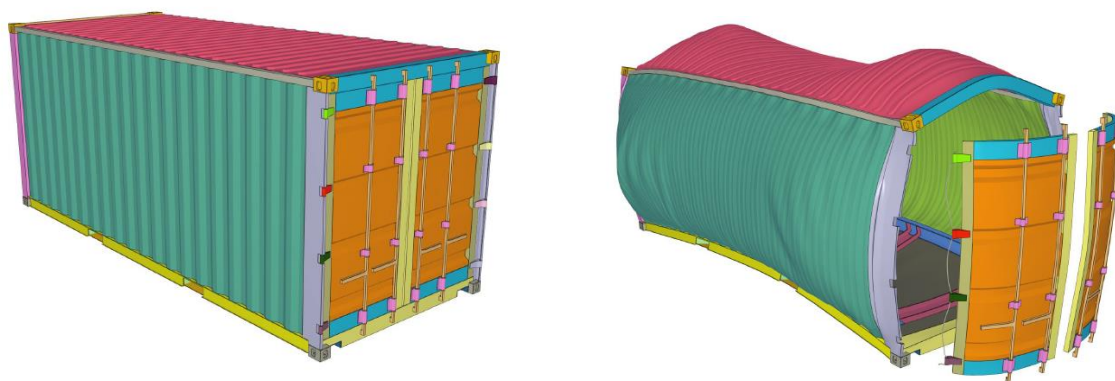


Figure 5.1. Illustration of a shipping container before and during an internal explosion (Hanssen, 2020).

5.1.2 Model simplifications

To achieve efficient simulations, the geometry of the container must be simplified. Including complex details of containers such as hinges, differences in material and geometrical properties of the floor, walls and roof will make the duration of the simulations prohibitively long. Figure 5.2 illustrates how a slice from a container can be used as a simplified model. The model used in this study was simplified further by assuming the same properties for the floor, roof, and walls, illustrated in Figure 5.3. This simplified model can be utilized to investigate how effects such as an increase in pressure or impulse and change in material or geometry influence the structure. Based on the maximum wall centre-displacement of the shipping container this simplified model can now be used to create P-I diagrams (Hanssen, 2020).

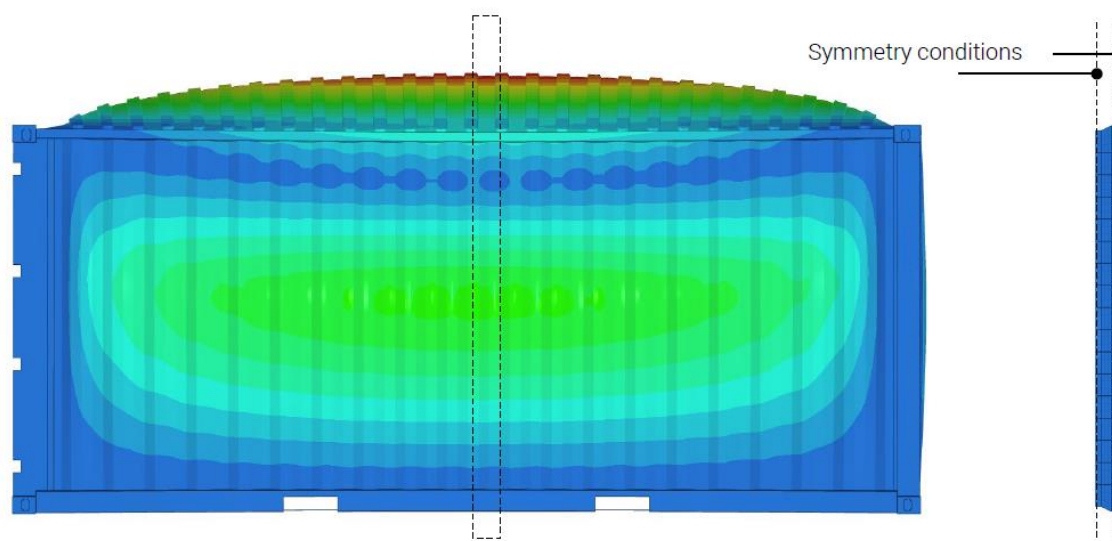


Figure 5.2. Illustration of the simplified model based on symmetry conditions (Hanssen, 2020).

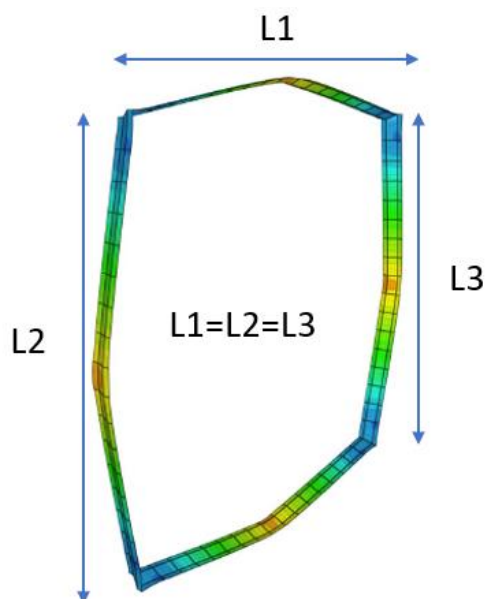


Figure 5.3. Simplified model behaviour for inner pressure load, $L1=L2=L3= 2464$ mm (Hanssen, 2020).

5.1.3 Model sensitivity studies

Sensitivity studies were carried out to ensure the accuracy of the model. For a simplified model, a special type of mass scaling called *SMS_CLUSTER can be applied. This mass scaling feature can speed up the simulations and filter out high frequencies. This is an efficient tool, but it is also a potentially dangerous tool to use and should be used with caution. It is very important to check that the use of mass scaling does not influence the physical results in any way. In the present study, this check was carried out by applying an inner pressure load to the simplified model and then monitoring the side wall displacement with and without mass scaling (Hanssen, 2020).

Table 5.1. Results from mass scaling model sensitivity studies (Hanssen, 2020).

Study	Run	Mass scaling	Time [min]	Comment
0	1	None	32	
	2	100	4.5	*SMS_CLUSTER

Table 5.1 and Figure 5.4 show that the use of a mass scaling factor of 100 will speed up the simulations significantly without influencing the physical results as the displacement is the same. Utilizing mass scaling is therefore advisable for this situation (Hanssen, 2020).

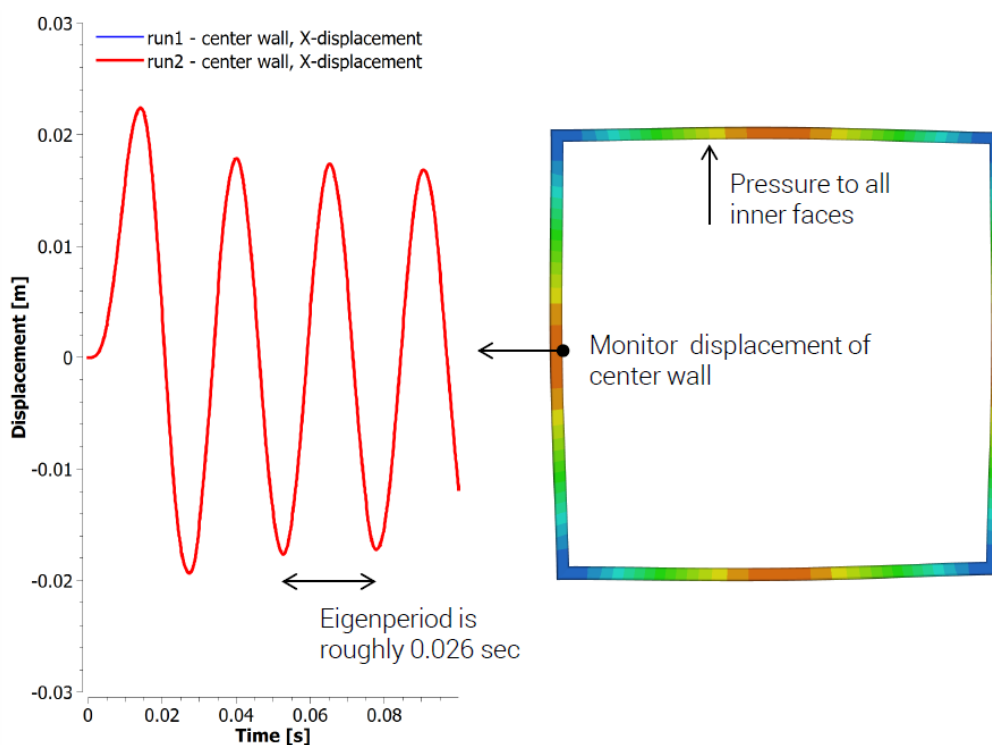


Figure 5.4. Displacement vs. time with and without mass scaling (left), and an illustration of a simplified model with monitoring on the centre of the wall (Hanssen, 2020).

A sensitivity study was also carried out for the geometry and materials by comparison with test data. The aim was to find a model that closely resembles the experimental results. Table 5.2 shows the different runs that were carried out by Hanssen (2020) with details about corrugation height, mesh, and material yield strength.

Table 5.2. Results from geometry and material model sensitivity studies (Hanssen, 2020).

Study	Run	Loading	Corrugation height [mm]	Mesh	Material yield strength (MPa)
0	3	HySEA Test 70	36	Original	355
	4		30	Original	355
	5		36	Fine	355
	6		36	Original	235
	7		32	Original	355

The experimentally measured pressure loading from HySEA Test 70 was applied. This test featured an almost quasi-static load, to test the response of corrugation height and material strength. Figure 5.5 shows that Run 7 with a corrugation height of 32 mm, a material yield strength of 355 MPa, and the original mesh is closest to the test data (Run 3) from Test 70 (Hanssen, 2020).

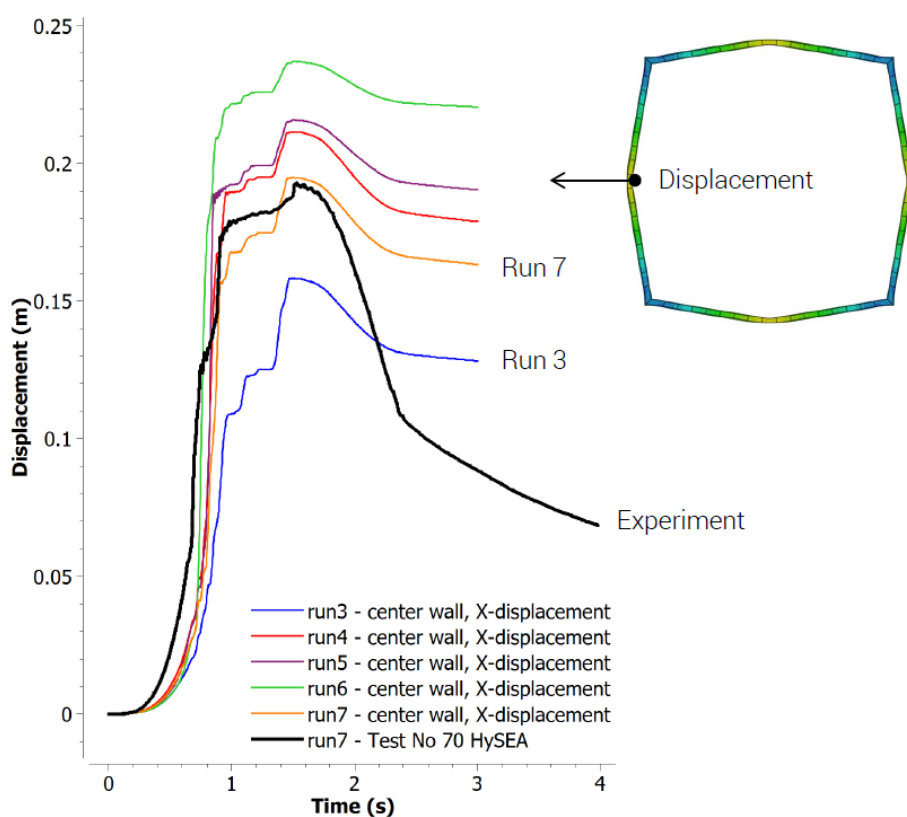


Figure 5.5. Results from geometry and material model sensitivity studies compared with results from Test 70 (Hanssen, 2020).

5.1.4 Final model

The model that was used in simulating the P-I curves had a corrugation height of 32 mm, 2mm wall thickness, 2465 mm wall length, and steel material with yield strength 355 MPa with no hardening. Figure 5.6 illustrates how the maximum displacement of the centre wall is monitored as pressure is added to all inner faces (Hanssen, 2020).

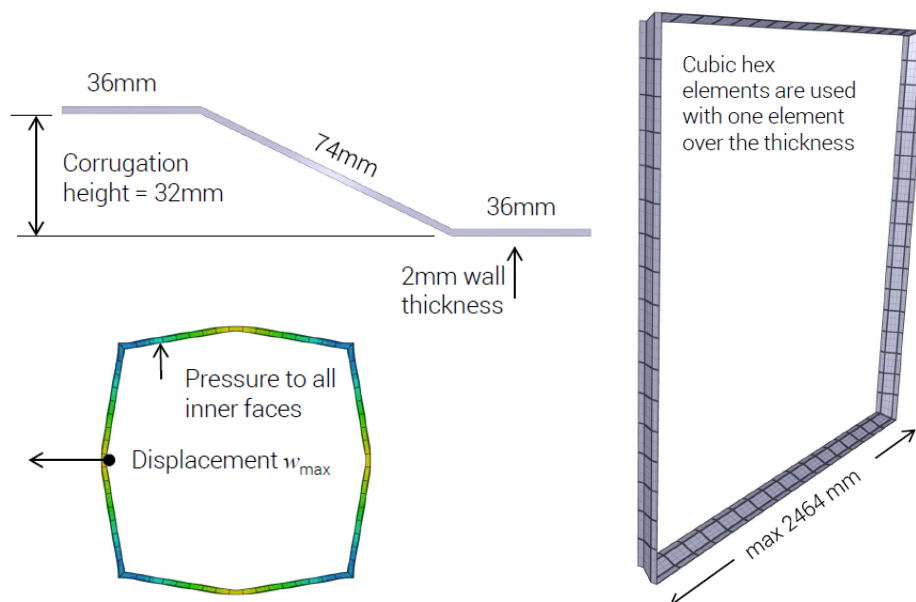


Figure 5.6. Illustration and details of the wall corrugation and the simplified model (Hanssen, 2020).

Figure 5.7 illustrates the “harmonic” pressure-time relation that was used in this study given by the following relation between the impulse (I), peak pressure (P_m), and the duration of the load (t_d) (Hanssen, 2020):

$$I = \frac{2}{\pi} P_m t_d \quad (5.1)$$

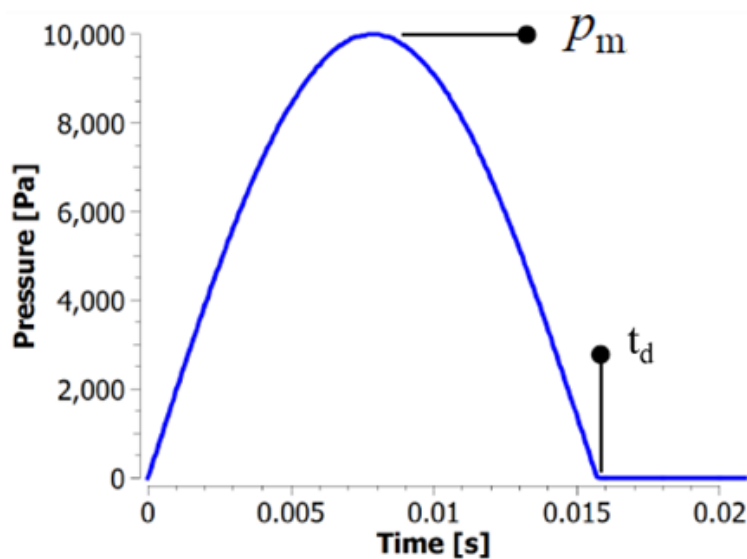


Figure 5.7. Harmonic pressure-time relation that was used in this study.

In addition, a triangular load with different rise time were used in some simulations, to investigate the effect of rise time. Figure 5.8 shows the relation between impulse (I), peak pressure (P_m), and the duration of the load (t_d) for a triangular load given by the following relation:

$$I = \frac{1}{2} P_m t_d \quad (5.2)$$

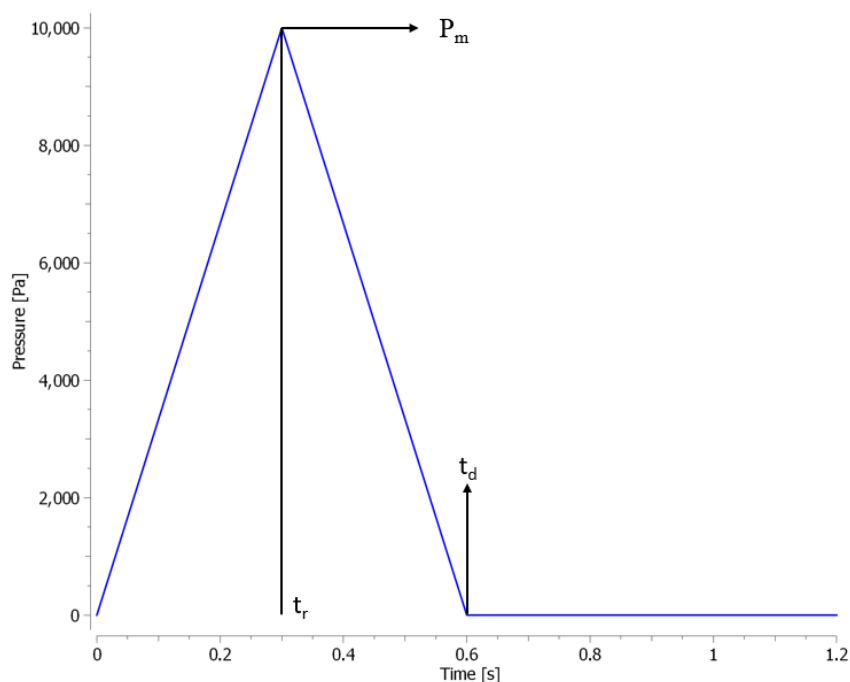


Figure 5.8. A triangular load with rise time relation $t_r = 0.5 t_d$.

In the present study, the harmonic pressure-time relation was utilized to find the P-I curves for maximum wall displacements of 5, 10, 20, and 30 cm on undamaged geometry. This was done by starting within the quasi-static loading regime and moving towards lower impulses and higher pressures to find the combinations of P_m and I that resulted in the desired maximum wall displacement, w_{max} . A few iterations were needed to get the desired displacement. This method was chosen due to its simplicity. For each iteration, the displacement result had to be checked against the desired displacement. If the displacement result deviated significantly from the desired result the maximum pressure or impulse had to be changed manually. This method provides good control of the results and minimizes the possibilities for errors. Appendix E shows the simulated pressures and impulses resulting in the desired displacements used to create the P-I curves.

Sensitivity studies on the material were also carried out by running the same simulations with steel strength 355 MPa and 235 MPa. Studies looking at the response on the walls when there was a dent of different sizes in the frame were also carried out.

6 Results and discussion

In this chapter, the results from the numerical study of P-I diagrams looking at the structural response of a 20-foot shipping container subjected to an internal load is presented, discussed, and compared with experimental results from the HySEA project. The damage criterion chosen for the generated P-I diagrams is maximum wall displacement. The numerical model used for simulations is too simplified to provide information about the material failure. Results from the sensitivity studies looking at the influence of steel strength and moderate damage on the structure are also presented.

6.1 Numerical pressure- impulse diagrams

Using the methodology of moving toward lower impulses and higher pressures with a few iterations, P-I diagrams for 5, 10, 20, and 30 cm were produced and illustrated in Figure 6.1. The curves display similar characteristics as the curve Baker et.al (1983) presented in Figure 4.1 for non-ideal explosions with finite rise time. Figure 6.1 shows that the characteristic “dip” in the dynamic area is present.

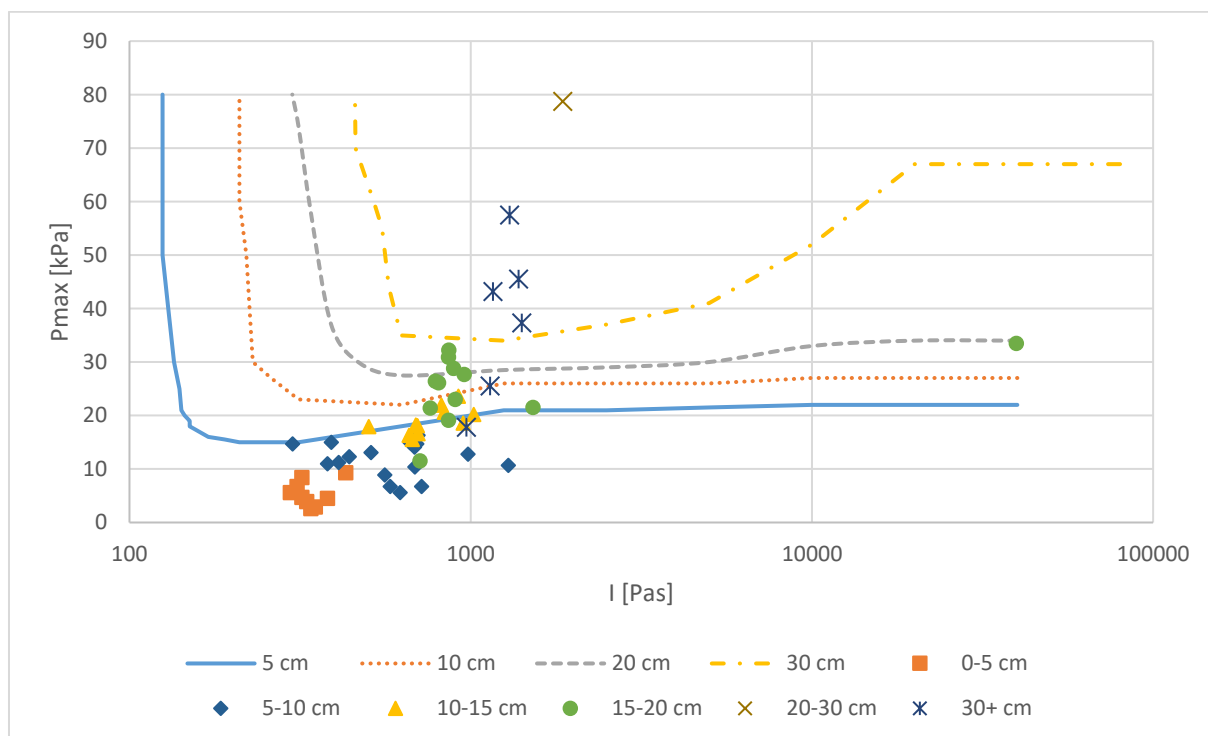


Figure 6.1. P-I diagram for 5, 10, 20, and 30 cm produced by simulations with Impetus Afea Solver plotted with the HySEA test results in displacement categories.

6.1.1 P-I diagram for maximum wall displacement of 20 cm

The 20 cm P-I curve presented in Figure 6.1 was motivated by the near quasi-static experiment from the HySEA project. This experiment was carried out to look at the structural response of the container walls when subjected to an internal quasi-static load and were achieved by using a low reactivity mixture with a concentration of 12 vol% hydrogen in air. Some leakage occurred, but the container remained closed during this experiment. Figure 6.2 illustrates the measured pressure-time history of the near quasi-static experiment.

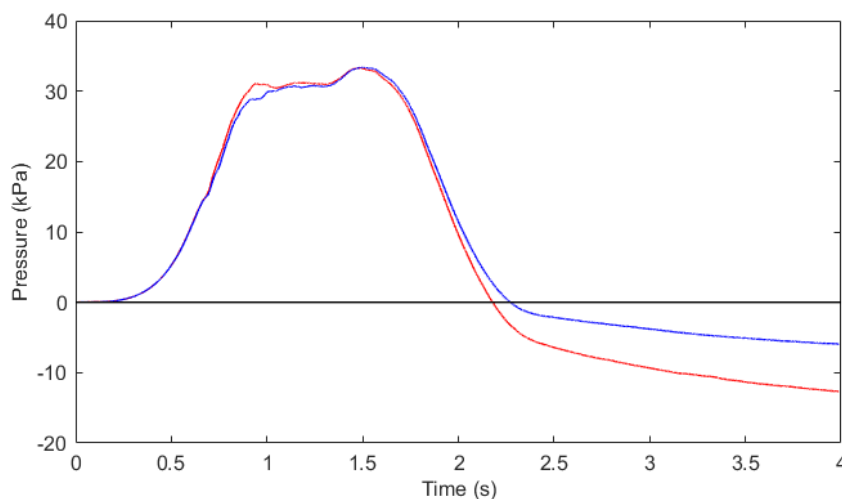


Figure 6.2. Average pressure-time history from the near quasi-static test for wall 1 (red) and wall 2 (blue).

The measured maximum pressure and the following maximum impulse were used in the simulation model to look at the resulting wall displacement. The result was then compared to the measured displacement (D1 and D2) of the two container walls. The result from using the pressure and impulse from wall 1 and wall 2 (W1 and W2 respectively) in the simulation gave a wall displacement of 19.88 cm and 19.89 cm (see Table A1 in Appendix A), while the measured experimental displacement was 18.91 cm and 19.64 cm, for W1 and W2, respectively. This gives a relative uncertainty of 2.4% for W1 and 0.6% for W2. See Appendix G for the uncertainty formula.

The simulated results were plotted creating a P-I curve for maximum wall displacement of around 20 cm. Figure 6.1 presents the curve and some average experimental results from the HySEA project. The results from the experimental tests were categorized in different displacement groups. The result from the almost quasi-static test lies just under the curve in the quasi-static region, which is expected since it was the motivation for the model. It also shows that most of the experimental results are in the dynamic region where the structural response is complex and highly influenced by the profile of the load. Figure 6.1 shows that there are deviations in the positioning of some of the displacement groups. The test results which gave a measured wall displacement of around 30 cm, show that most of the results lie

above the 30 cm curve as desired, while some lie below. Possible reasons for the deviations are discussed further down.

6.1.2 P-I diagram for maximum wall displacement vs experimental results

For a more systematic analysis of why some of the experimental test results may deviate from the simulated curves, a closer look at each container and their corresponding tests were completed. Each container had a different number of tests carried out on them. Since most of the containers were used in several tests there will in some cases be permanent deformation from previous experiments affecting the results and therefore causing significant uncertainty. Damage from the previous test will make the container and material weaker.

Container #1

Figure 6.3 shows the results from the tests carried out with the first of the twelve containers. For test number nine the displacement was not measured since the back wall of the container ruptured and the doors flew off due to breakage in the hinges. This shows the danger of projectiles. Table 6.1 presents the average experimental results for each test carried out on container one. The experimental results are categorized in different displacement groups and comments on which test that experienced multiple pressure peaks are presented. For detailed results on the P-I curves with 5, 10, 20, and 30 cm displacement, see Appendix A. Appendix B for details about each test and Appendix C for further details about the relative test number (RC) of the containers, geometry configurations (GC), ventilation device (VD), ignition position (IG), mixture generation (MG) and initial turbulence (IT).

Table 6.1. Experimental results for tests carried out on Container 1 including maximum pressure (P), impulse (I), maximum displacement (D_m), permanent deformation (D_p), and comments on the shape of the pressure-time histories.

Container	Test	P [kPa]	I [Pa s]	D_m [cm]	Group D_m [cm]	D_p [cm]	Group D_p [cm]	Comment on pressure peaks
1	1	2.9	350.0	1.8	0-5	0.0	0-5	MP
	2	2.6	340.0	4.2	0-5	0.1	0-5	MP
	3	6.7	580.0	9.6	5-10	1.1	0-5	MP
	4	5.6	620.0	6.3	5-10	0.1	0-5	MP
	5	3.9	330.0	1.7	0-5	0.0	0-5	MP
	6	4.5	380.0	3.2	0-5	0.2	0-5	MP
	7	19.1	860.0	19.0	15-20	3.1	0-5	DP
	8	37.3	1410.0	45.0	30+	0.0	0-5	DP
	9	129.5	4780.0	-	-	-	-	SP

* Single peak (SP), Double peak (DP), Multiple peaks (MP)

As mentioned earlier, displacement of the walls in the experimental project was measured on two walls with different results, the results from both wall one and two are included in the different displacement groups used in the figures. This implies that test results from one test can be included in two displacement groups.

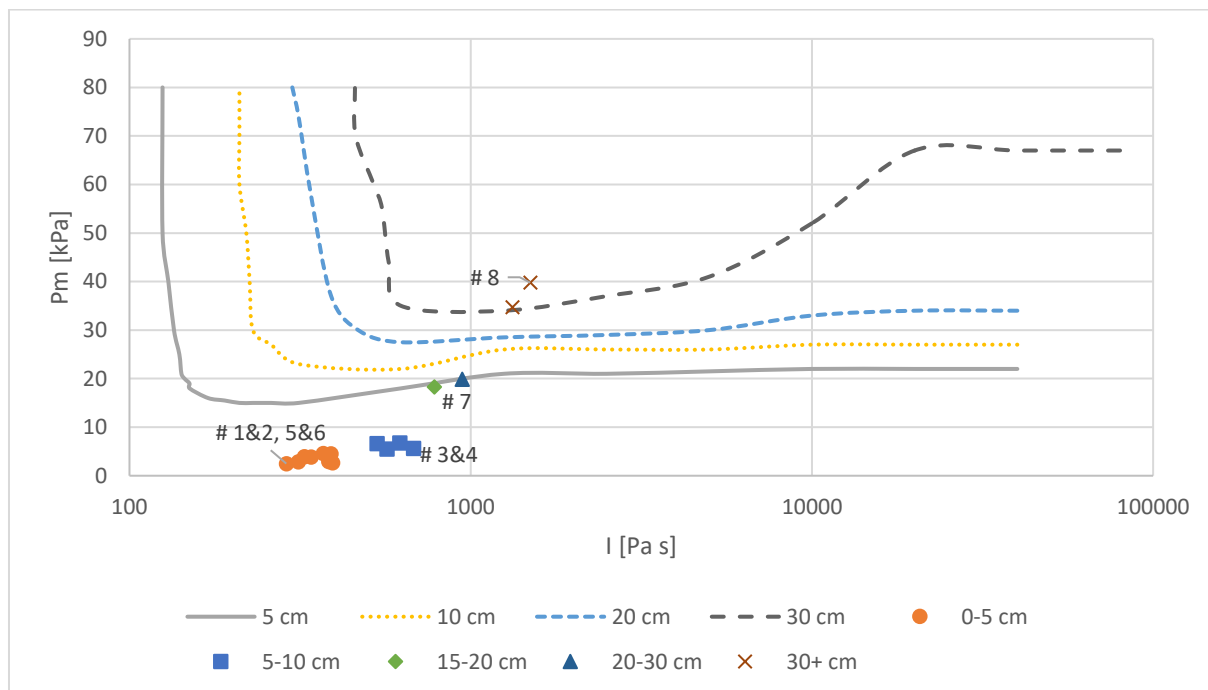


Figure 6.3. P-I curve for maximum wall displacement plotted with HySEA test results divided in displacement categories for Container 1.

For container one, the displacement categories 0-5 cm and 30+ cm agree reasonably well with the P-I curves. Test 3 and 4 are in the 5-10 cm group and should theoretically be in between the 5 and 10 cm curves, not below the 5 cm curve. The geometry configuration of Test 3 and 4 include a bottle basket in the inner position (see Figures 3.3 and 3.4), ventilation through the open container doors and the ignition position is in the back-wall centre. There was no initial turbulence and the mixture was homogeneous. Displacement groups 15-20 cm and 20-30 cm are also located on the 5 cm P-I curve, which is lower than expected.

Possible causes for the deviations can be that the container was already used in experiments before. Damage may have weakened the material and structure, resulting in higher displacements of the walls from lower pressure and impulse. The pressure-time histories from the experiment were also not ideal. They were for many tests very complex with multiple pressure peaks which makes it difficult to determine the impulse. This will influence the results significantly. Figure 6.4 illustrates some complex pressure-time histories from the experimental project.

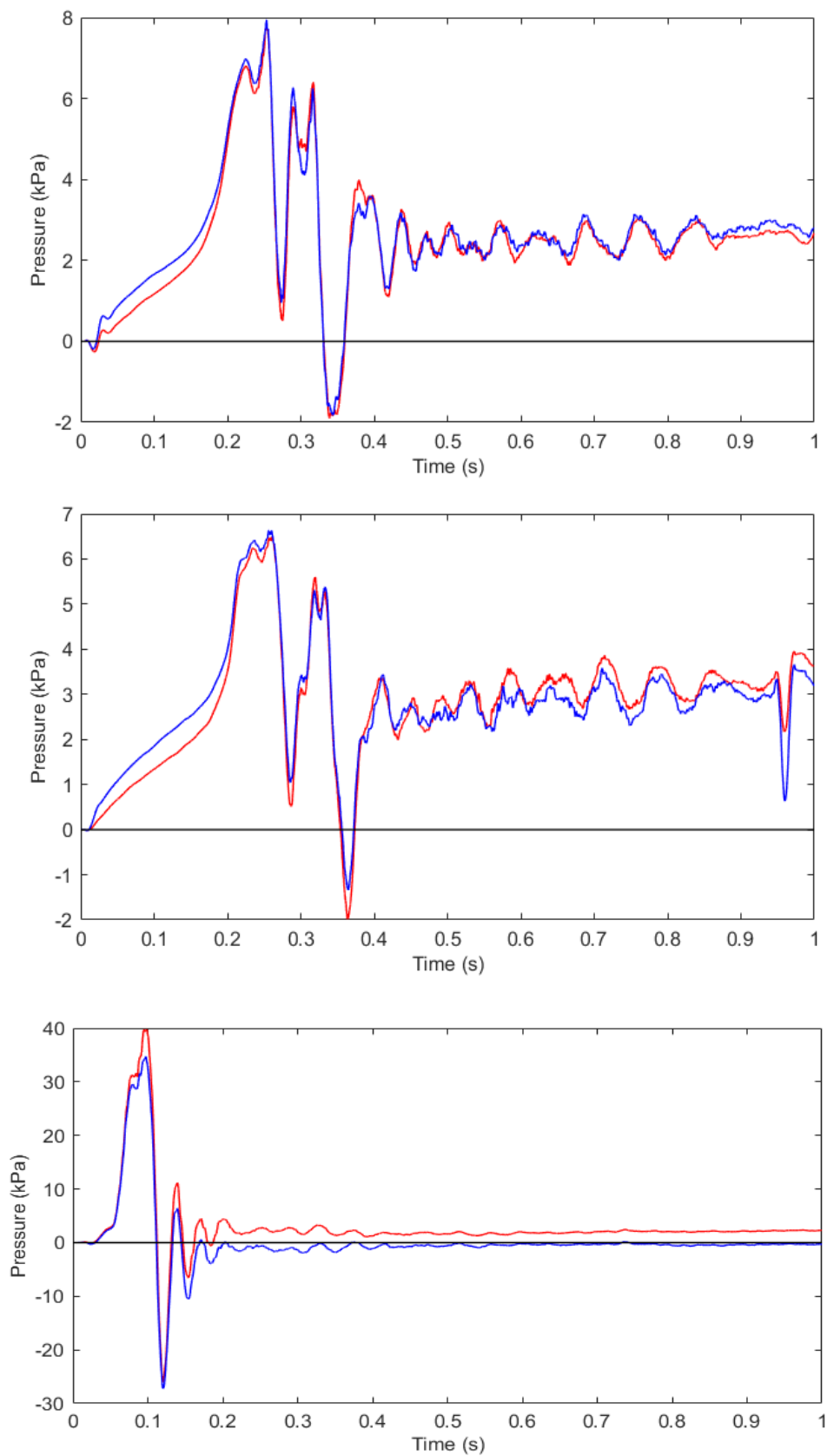


Figure 6.4. Average pressure-time histories for wall 1 (red) and wall 2 (blue) for Test 3 (top) and Test 4 (middle) and Test 8 (bottom).

Maximum displacement can be very sensitive to the resonance phenomena, where the frequency of the load subjected to the structure is near or equal to the structure's Eigenfrequency. Because of this phenomenon, the measured displacement may be higher than what it was so it can be sensible to look at the permanent deformation, D_p , for comparison. The frequency of the main pressure oscillations for tests 3 and 4 was around 17 Hz, which is also the Eigenfrequency of the structure. Table 6.1 shows details of the displacement and permanent deformation for each test including their corresponding displacement or deformation groups.

For the experiments with the container doors open, Skjold (2018a) stated that it was in the closed end of the container the highest pressures were measured. Since the simulation had a uniform pressure load equal to all the walls, different ignition positions and differences in the distribution of the pressures in the container is not replicated in the simulation. The difference in the pressure distribution in the container can influence different parts of the container. It may have a greater impact on the weaker points of the container, i.e. where the walls are connected with hinges. The corrugation height was also adjusted in the simulation to achieve a model closest to the test data.

The experimental measured pressure-time histories were for some tests simulated in Impetus Afea to calculate the resulting maximum wall displacement. Table 6.2 presents the results from the simulation, the average experimental displacement, and permanent deformation results. The pressure-time histories were used in a model with and without a dent. Using the pressure-time histories from Test 3 in the simulation model, the maximum displacement of the walls was 2.725 cm and 6.047 cm for a model without and with a dent, respectively. For an undamaged structure, the simulated maximum displacement is significantly smaller than the displacement measured in the experimental test. The measured experimental displacement is closer to the displacement reached when there was a dent in one of the walls. As the frequency of the main pressure oscillations for tests 3 and 4 was equal or very close to the structures Eigenfrequency it may have influenced the measured displacement significantly. The pressure-time histories are complex, and it is not straightforward to determine the Eigenfrequency and significant uncertainties are expected. Similar results were obtained for tests 4, 5, and 8. The experimental displacement result is likely influenced by permanent deformation from previous tests. This may be why the result is closer to the displacement results of the structure with a dent. Looking at the result from the simulated model without a dent the results fit quite good with the placement of the test results in the P-I diagrams. Figure 6.5 illustrates the displacement-time histories for the simulated and experimental test results for Test 5 utilizing the same pressure-time history.

Table 6.2. Results from the experimental measured pressure-time histories simulated in Impetus Afea compared to experimental results.

Container	Test	Simulated results		Experimental results	
		D_m [cm]	D_m [cm] with dent, amp=1	D_m [cm]	D_p [cm]
1	3	2.725	6.047	9.6	1.1
	4	1.737	6.124	6.3	0.1
	5	0.8188	2.372	1.7	0.0
	8	29.60	35.91	45.0	0.0
2	12	2.751	7.318	17.9	2.0
	13	13.94	35.43	34.0	3.1
	14	47.71	50.77	28.5	10.3
3	15	4.581	17.65	32.2	10.1
4	25	4.748	10.50	5.6	0.3
11	70	19.92	23.34	19.3	6.5

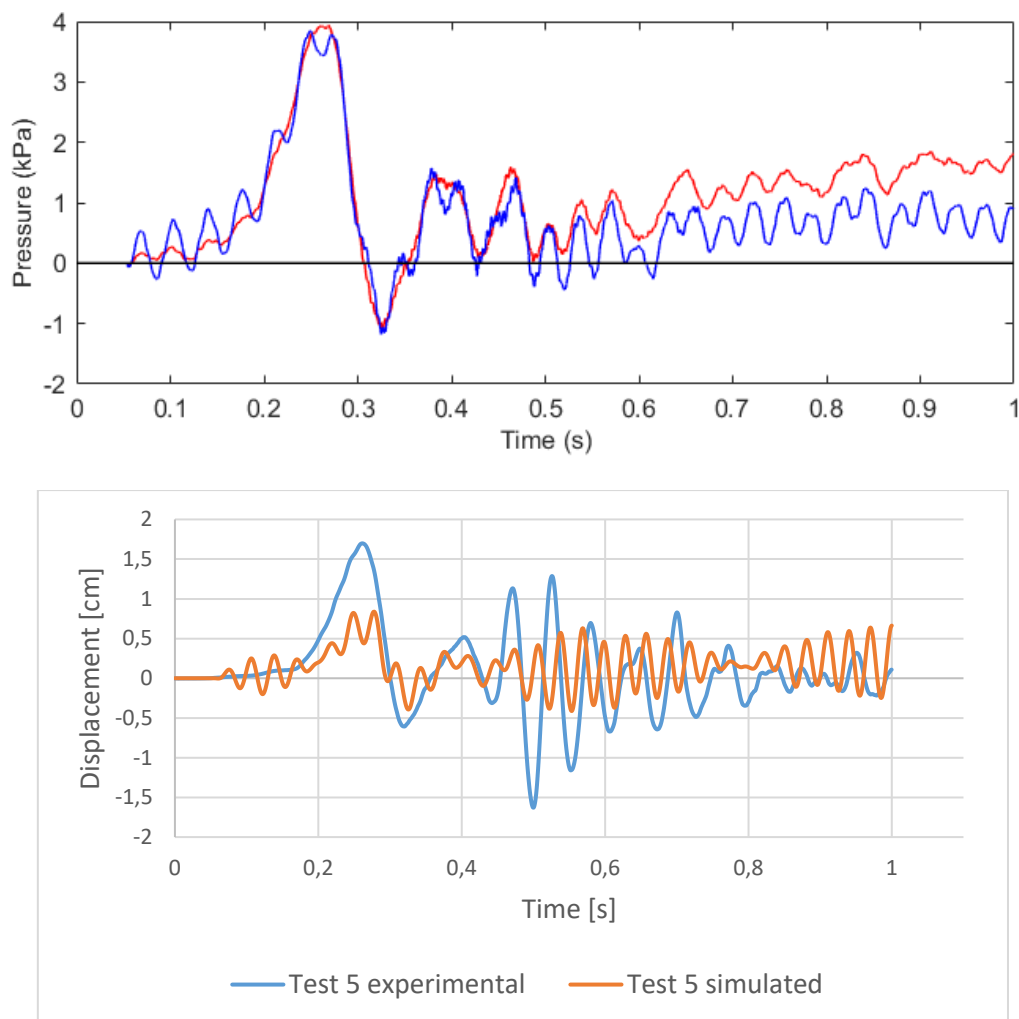


Figure 6.5. Top: average pressure-time recording for wall 1 (red) and wall 2 (blue) from Test 5. Bottom: displacement vs time. Comparison of experiment vs simulation. In the simulation the top pressure curve has been applied as the load.

Container #2

Container number two was used in five experiments, tests 10-14. Results from the five experiments divided into displacement categories are plotted in Figure 6.7. The measured displacement from Test 10 was inconclusive and therefore not included. Most of the displacement categories from the experiment were below the expected curves. The reasons for this are likely the same as mentioned above for the experiments on container one. Test 12 and 13 in displacement groups 15-20 cm and 30+ cm, respectively were both below their expected curves. Test 14 had the results from wall 1 in the displacement group 20-30 cm and wall 2 in displacement group 30+, they were both above the 30 cm curve. The back wall of the container also ruptured in Test 14.

Table 6.3 shows that the tests had pressure-time histories with double pressure peaks which may influence the displacement result. The pressure-time histories for tests 12-14 were simulated in Impetus Afea. Table 6.2 presents the results. Test 12 shows similarities to the tests carried out on container 1, while the displacement result from Test 13 shows that the experimental displacement lies between the results of the two simulation models and is slightly less than the simulated result from the model with a dent. The experimental result from Test 14 is significantly lower than the simulated results. The maximum pressure for Test 14 was almost 80 kPa which is significantly higher than for the other tests. The pressure-time history from Test 14 had a great impact on the structure in the simulation model. Figure 6.6 illustrates how this complex load influences the simplified structure from the simulation. The original structure is deformed beyond recognition. The simulated displacement results are well suited to the position of the tests in the P-I diagram.

Table 6.3. Experimental results for tests carried out on Container 2 including maximum pressure (P), impulse (I), maximum displacement (D_m), permanent deformation (D_p), and comments on the shape of the pressure-time histories.

Container	Test	P [kPa]	I [Pa s]	D_m [cm]	Group D_m [cm]	D_p [cm]	Group D_p [cm]	Comment on pressure peaks
2	10	12.7	740.0	-	-	-	-	DP
	11	4.7	320.0	4.0	0-5	0.2	0-5	DP
	12	11.5	710.0	17.9	15-20	2.0	0-5	DP
	13	25.5	1140	34.0	30+	3.1	0-5	DP
	14	78.7	1860	28.5	20-30	10.3	10-15	DP

* Single peak (SP), Double peak (DP), Multiple peaks (MP)

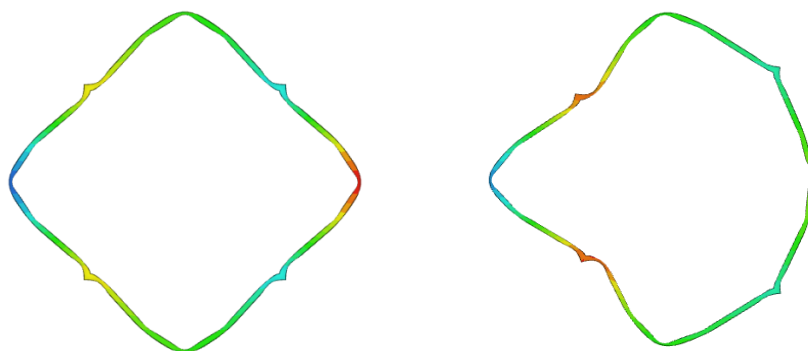


Figure 6.6. Illustration of the simulated model without (left) and with (right) a dent subjected to pressure-time histories from Test 14.

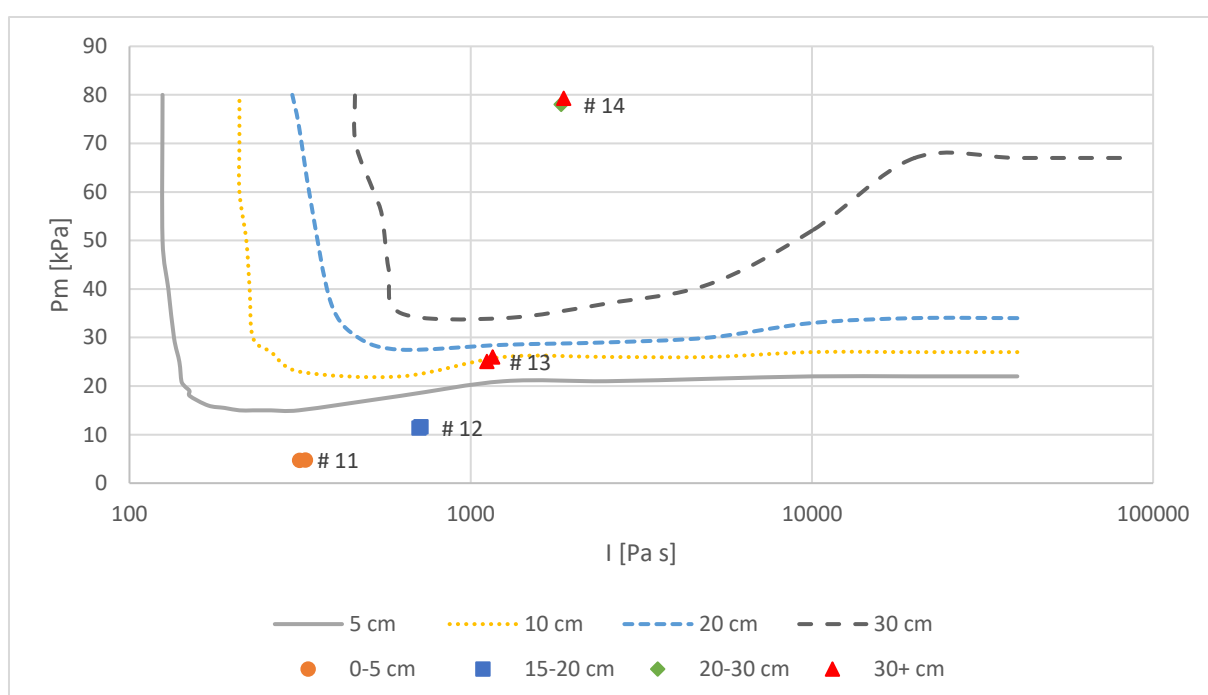


Figure 6.7. P-I curve for maximum wall displacement plotted with HySEA test results divided in displacement categories for Container 2.

Container #3

The third container was used in six experiments, tests 15-20. Figure 6.8 shows the results plotted in displacement categories. Looking at the results from Table B3 (Appendix B) it shows that the measured displacement for wall 2 is higher than for wall 1. Reasons for this can be weaknesses in the container, hinges and manufacturing defaults, or irregularities in how the deflagration spread and distributed different loads throughout the container. The tests that were carried out for this container varied between frame only, a pipe rack in the middle position, and ventilation through the roof with either polyethylene roof or bulged single sheet vent panels. The ignition position, mixture generation, and the initial turbulence were the

same for all the tests and were respectively floor centre, homogeneous mixture, and initially quiescent.

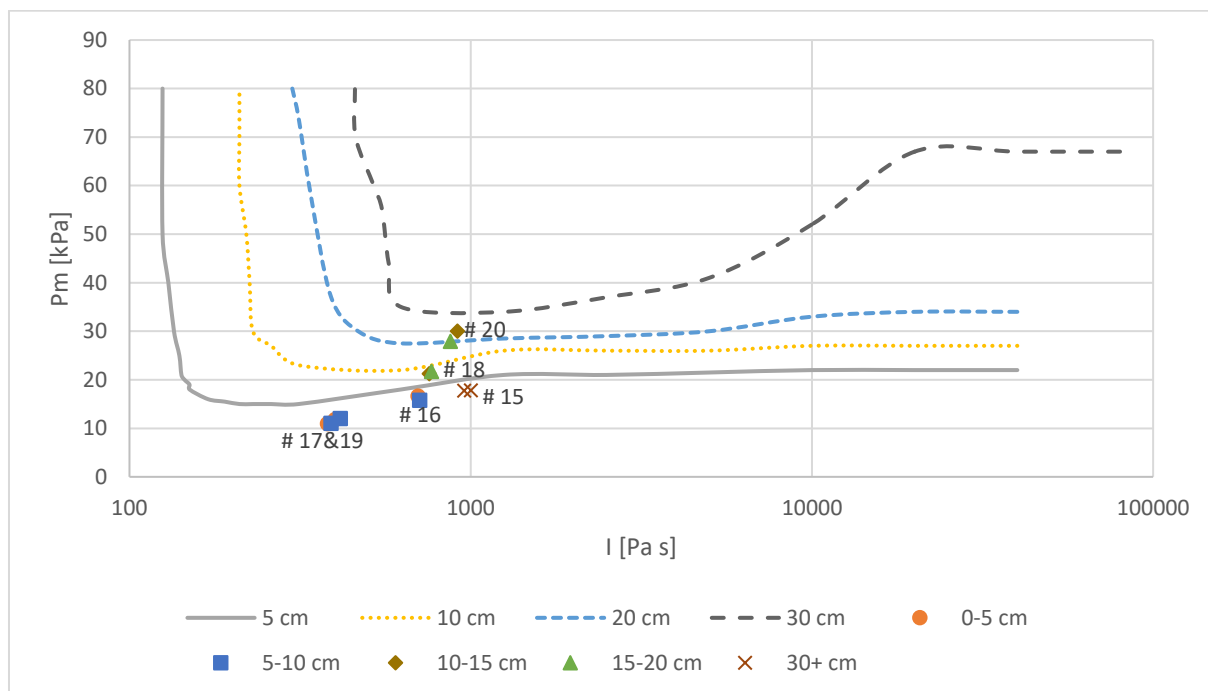


Figure 6.8. P-I curve for maximum wall displacement plotted with HySEA test results divided in displacement categories for Container 3.

As seen for the previous containers, some of the displacement groups are located within reasonable limits and some are below. Test 15 gave a measured displacement of 30+ cm. It was the first experiment on this container and the only test that resulted in displacement higher than 30 cm and ended up beneath the 5 cm curve. The frequency of this load was around 33 Hz. The ignition position was floor centre and the ventilation were through bulged single sheet vent panels.

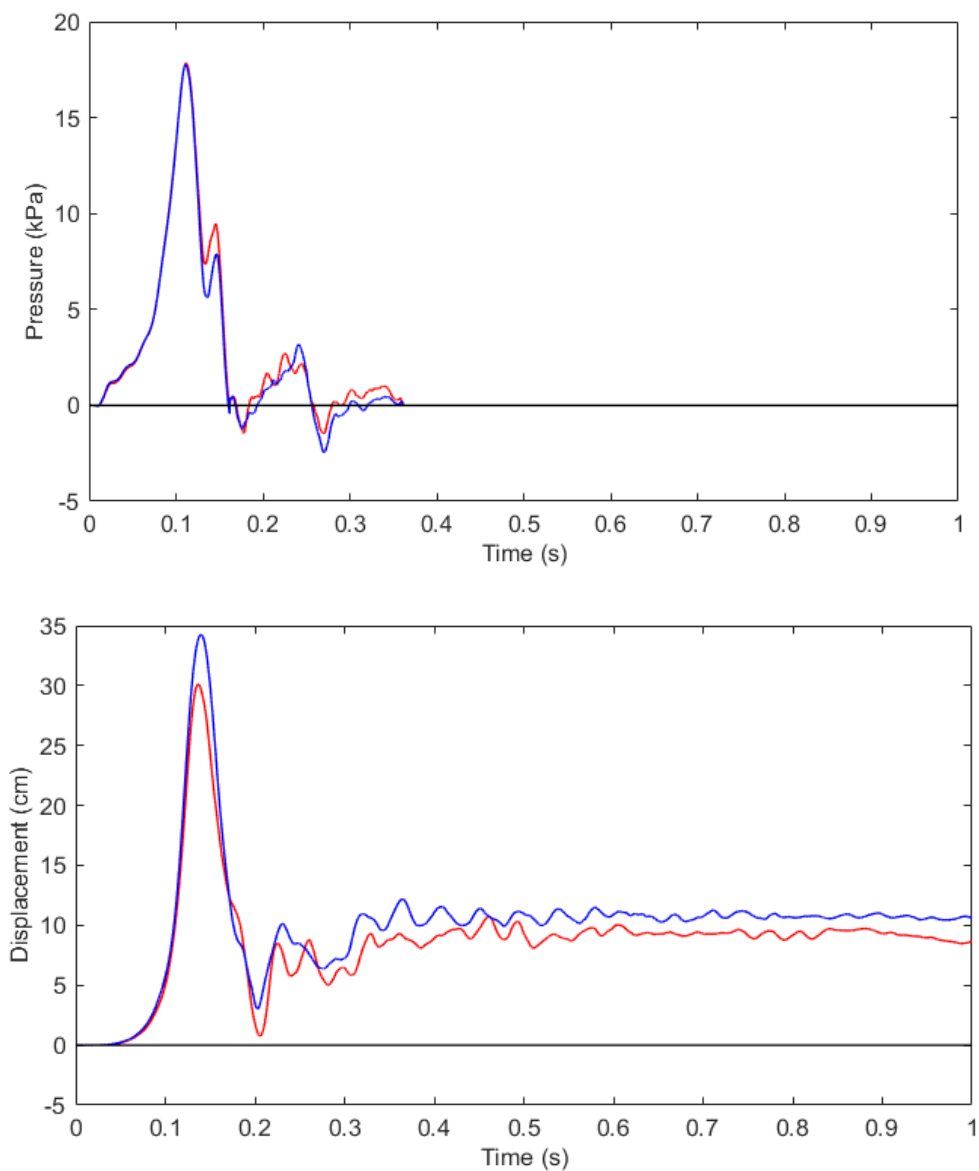


Figure 6.9. Average pressure-time histories (top) and measured displacement (bottom) for wall 1 (red) and wall 2 (blue) for Test 15.

Table 6.4 shows that the tests had pressure-time histories with single, double, and multiple pressure peaks. The pressure-time histories for Test 15 were simulated in Impetus Afea. The result presented in Table 6.2 showed that the simulation model without a dent using the pressure-time history from Test 15 resulted in a maximum wall displacement of 4.581 cm. This result agrees well with the placement of Test 15 in Figure 6.8.

Table 6.4. Experimental results for tests carried out on Container 3 including maximum pressure (P), impulse (I), maximum displacement (D_m), permanent deformation (D_p), and comments on the shape of the pressure-time histories.

Container	Test	P [kPa]	I [Pa s]	D_m [cm]	Group D_m [cm]	D_p [cm]	Group D_p [cm]	Comment on pressure peaks
3	15	17.8	970.0	32.2	30+	10.1	10-15	MP
	16	16.3	700.0	5.6	5-10	0.7	5-10	MP
	17	11.0	380.0	5.8	5-10	0.6	5-10	MP
	18	21.4	760.0	16.0	15-20	4.0	5-10	SP
	19	11.9	410.0	6.3	5-10	1.4	0-5	MP
	20	28.8	890.0	17.1	15-20	8.3	5-10	DP

* Single peak (SP), Double peak (DP), Multiple peaks (MP)

Container #4

Container number four was used in eight tests, 21-28. The experimental results are plotted in displacement categories in Figure 6.10. The tests for this container varied between frame only and a pipe rack in the middle position, and ventilation through the roof with either polyethylene roof or bulged single sheet vent panels. The ignition position, mixture generation, and the initial turbulence were the same for all the tests and were respectively floor centre, homogeneous mixture, and initially quiescent. The displacement group 5-10 cm and 10-15 cm lies below the 5 cm curve, while the displacement group 15-20 cm lies both below and over its intended region.

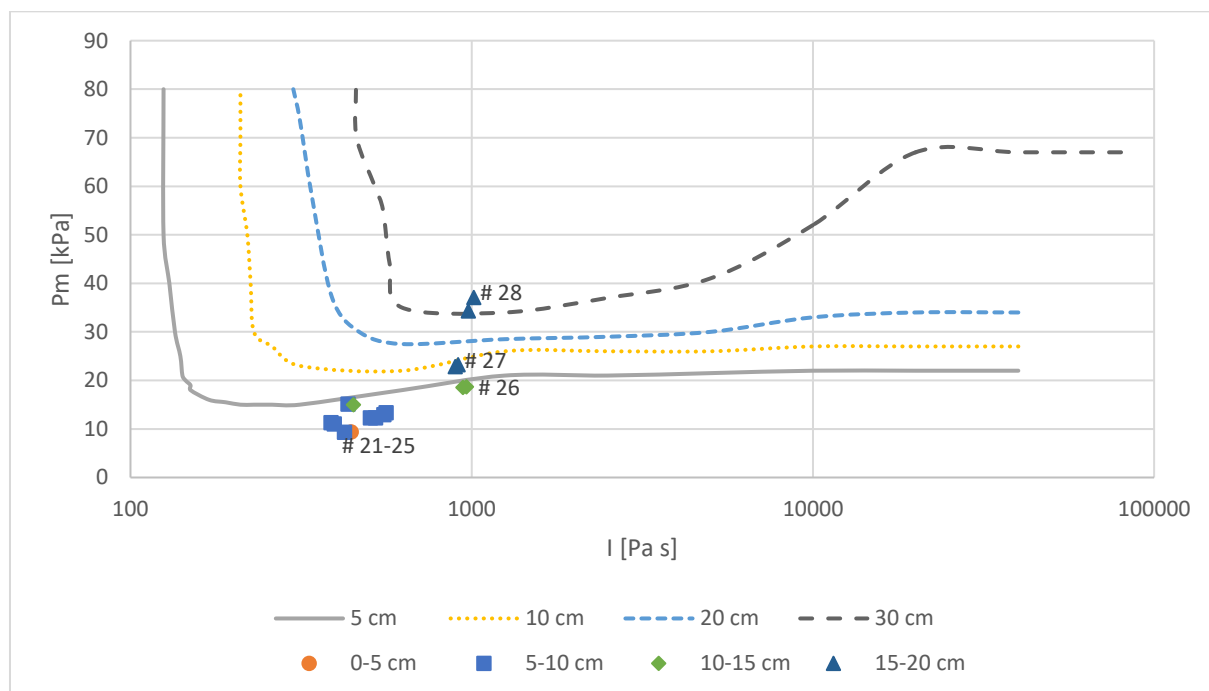


Figure 6.10. P - I curve for maximum wall displacement plotted with HySEA test results divided in displacement categories for Container 4.

Table 6.5 shows that the tests had complex pressure-time histories with double and multiple pressure peaks. The pressure-time histories for Test 25 were simulated in Impetus Afea. The result presented in Table 6.2 showed that the simulation model without a dent using the pressure-time history from Test 25 resulted in a maximum wall displacement of 4.748 cm. This result agrees well with the placement of Test 25 in Figure 6.10.

Table 6.5. Experimental results for tests carried out on Container 4 including maximum pressure (P), impulse (I), maximum displacement (D_m), permanent deformation (D_p), and comments on the shape of the pressure-time histories.

Container	Test	P [kPa]	I [Pa s]	D_m [cm]	Group D_m [cm]	D_p [cm]	Group D_p [cm]	Comment on pressure peaks
4	21	9.3	430.0	4.3	0-5	0.4	0-5	MP
	22	11.2	390.0	6.5	5-10	1.2	0-5	MP
	23	15.0	440.0	9.1	5-10	2.6	0-5	DP
	24	12.3	510.0	6.5	5-10	0.3	0-5	DP
	25	13.1	560.0	5.6	5-10	0.3	0-5	DP
	26	18.6	950.0	10.3	10-15	0.7	0-5	DP
	27	23.0	900.0	15.8	15-20	4.2	0-5	MP
	28	30.9	860.0	16.8	15-20	8.1	5-10	DP

* Single peak (SP), Double peak (DP), Multiple peaks (MP)

Containers #5- #12

This pattern of experimental results deviating from their intended positions continues for the next containers. Some of the results fit quite well, some are near their intended region and some are way off. Since the model used in the simulations is simplified, deviations while comparing the curve to experimental results are expected. The model of the container had to be simplified so an efficient simulation could be carried out. This means that many detailed elements that may affect the structural response of a container will be excluded, such as weak points on the container. Some weak points on the structure can be where the walls, roof, and floor are connected by i.e. hinges or welding. Containers experience wear and tear, and manufacturing faults can also have an impact.

In the HySEA project, some of the containers underwent some modifications such as inserting ventilation on the roof. This will likely affect the results by weakening the structure of the container and is probably a major cause for the scatter. The simulation was also only carried out on a closed empty geometry, while the experiment varied between different types and positions of ventilation and obstacles inside the container. The material of the container used in the experimental project was not analysed. This results in significant uncertainty when it comes to the material and its behavioural characteristics.

In the simulations, there is a uniform load evenly distributed on all the walls. This is not necessarily the case for a real explosion. Uncertainties in the measured pressure may result in significant deviations as the pressure was measured at the frame on the floor, near the walls. There may also be uncertainties associated with the data processing of the experimental data from the HySEA project. Skjold (2018b) discuss in further detail how the data was processed, and the uncertainties related to this process. He emphasised that several pressure measurements were discarded due to problems associated with drift and noise. This problem was most severe for the weakest explosions (Skjold, 2018b).

Symmetry was used in the simplified model where all the walls were the same. This is not the case for a real full-size container. In the experiment, the wall displacement was measured on two of the walls (D1 and D2 illustrated in Figure 3.4) and the results showed a difference in the measured wall displacements for these two walls, while the displacement was the same for all the walls in the simulations. The same containers were also used in several tests which results in a significant uncertainty due to permanent deformation influencing the following test results. In the simulations, a harmonic pressure-time pulse is assumed, which deviates from the pressure loadings from the experiments, which in some cases showed multiple pressure peaks.

The maximum displacement results in Table 6.2, where the experimental measured pressure-time histories for some tests were used in a simplified simulation model, were more suitable to the placement of the test results in the P-I diagrams. Since there are significant uncertainties in the experimentally measured displacement, more experimental pressure-time histories could be simulated as only some selected experiments were simulated due to time limitations. Despite the deviations between model predictions and experiments, the use of P-I diagrams may still be valuable for safety and design purposes. The primary limitation from an engineering design point of view will most likely be the reliable prediction of the relevant pressure loads for a given structure. It is not straightforward to predict relevant pressure loads, especially for vented hydrogen deflagrations in 20-foot shipping containers with finite rise time, this was demonstrated by two blind-prediction benchmark studies conducted as part of the HySEA project (Skjold, et al., 2019a; Skjold, et al., 2019d). Comparing displacement and permanent deformation can also be valuable. Appendix D presents details of the displacement and permanent deformation for each test including their corresponding displacement and deformation groups.

Table 6.6 shows an overview of which displacement group that was either located under or over its “intended region”. G is for the results that are located in a good position. U and O are for the results that are under or over their intended region. When some of the results from the same displacement group are under and over it is marked with I for inconclusive. Container

eleven was used for the near quasi-static experiment so this result lies just below the 20 cm curve, as it was the motivation behind the simulation model.

Table 6.6. Detailed overview of displacement groups location, over or under its “intended region”.

Disp. groups	Container											
	1	2	3	4	5	6	7	8	9	10	11	12
0-5 cm	G	G	G	G	-	-	G	-	-	-	-	-
5-10 cm	U	-	U	U	G	U	U	-	-	U	-	U
10-15 cm	-	-	I	U	U	-	U	G	-	U	-	-
15-20 cm	U	U	I	I	U	O	I	G	-	-	G	-
20-30 cm	U	O	-	-	-	-	-	-	-	-	-	-
30+ cm	G	I	U	-	-	-	-	-	G	G	-	G

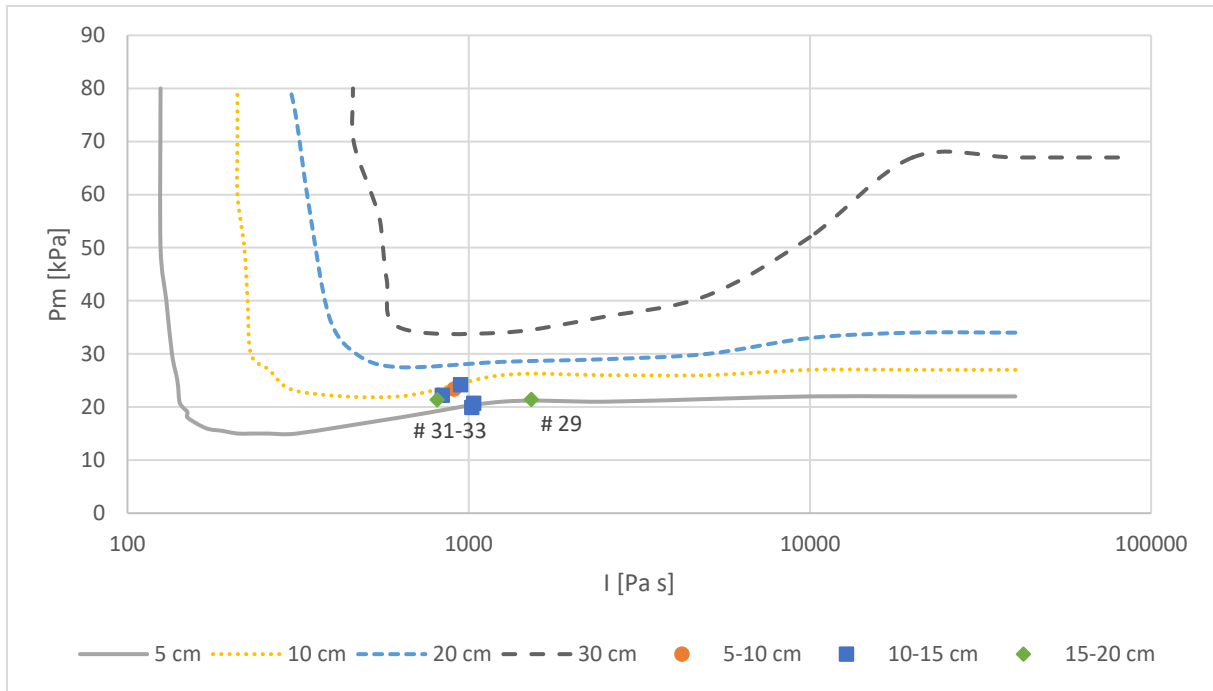


Figure 6.11. P-I curve for maximum wall displacement plotted with HySEA test results divided in displacement categories for Container 5.

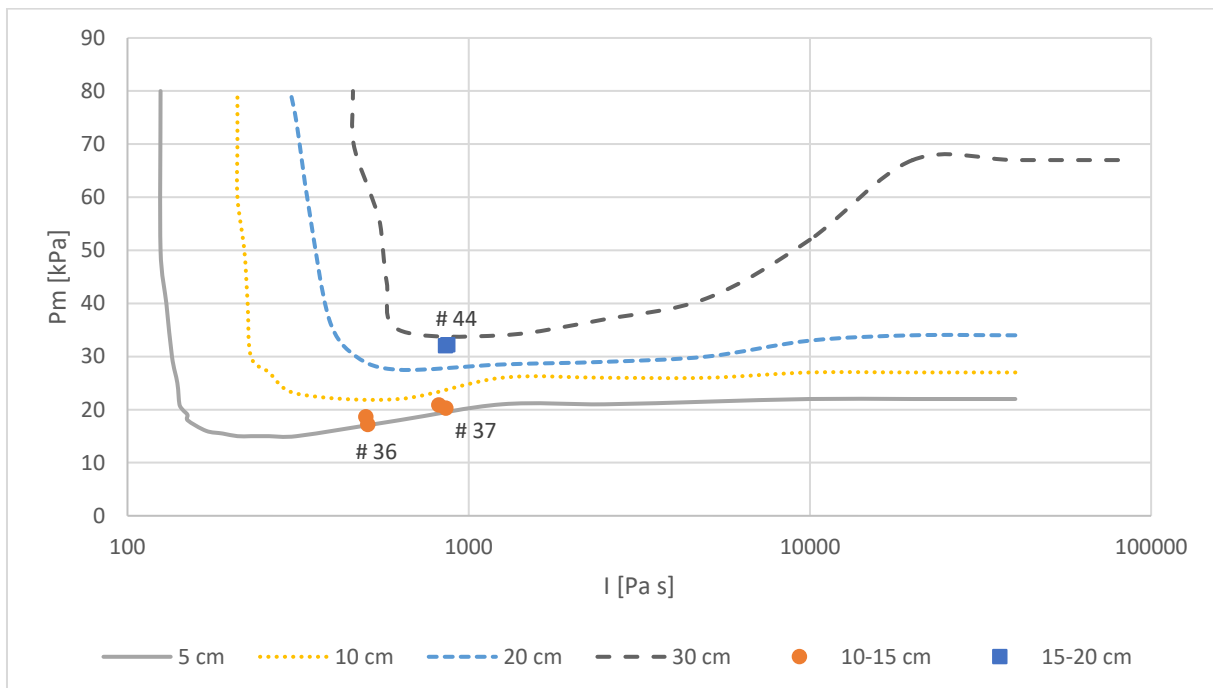


Figure 6.12. P-I curve for maximum wall displacement plotted with HySEA test results divided in displacement categories for Container 6.

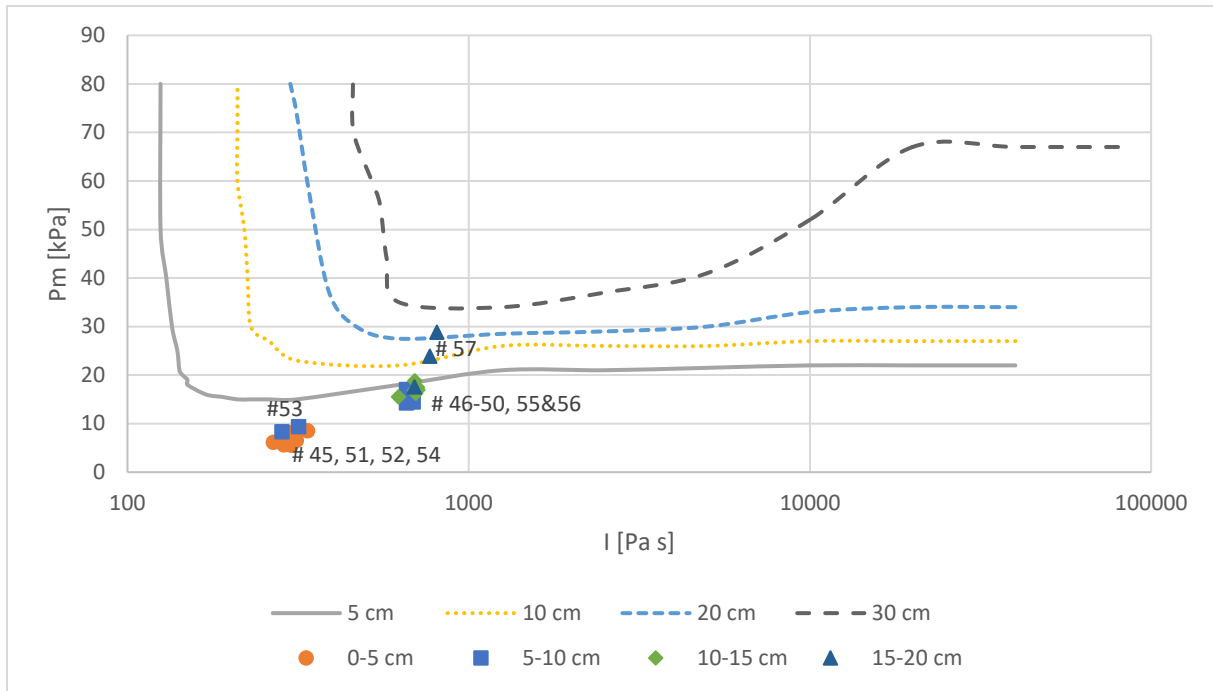


Figure 6.13. P-I curve for maximum wall displacement plotted with HySEA test results divided in displacement categories for Container 7.

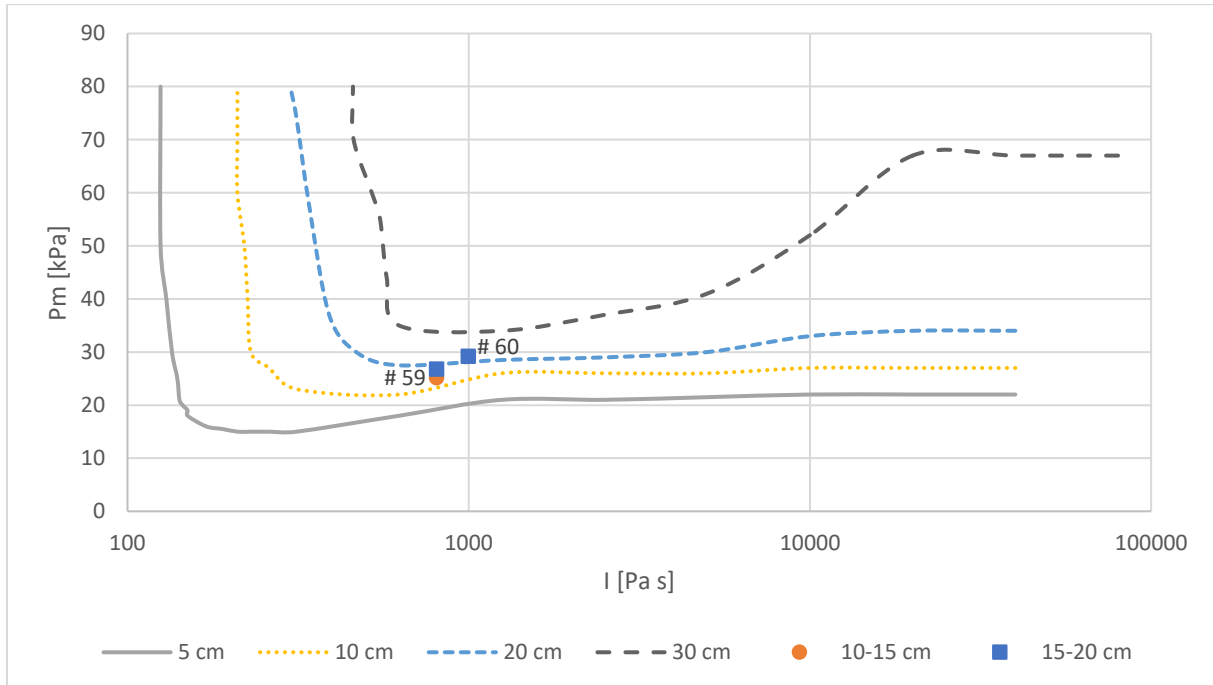


Figure 6.14. P-I curve for maximum wall displacement plotted with HySEA test results divided in displacement categories for Container 8.

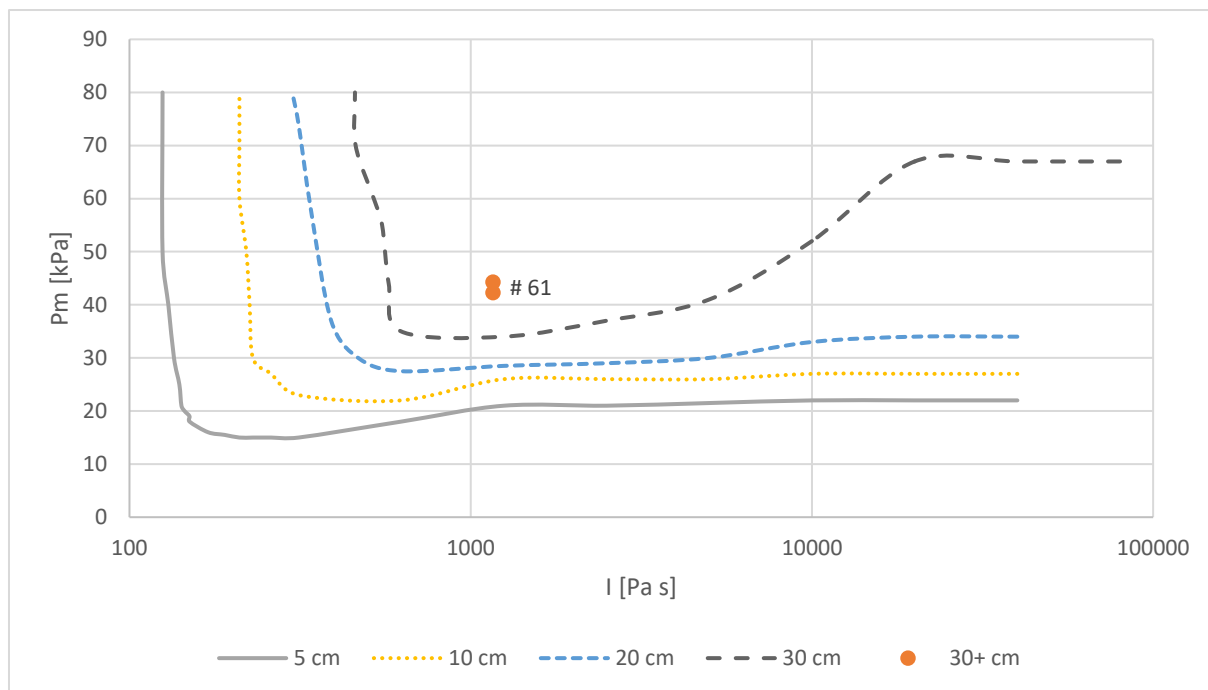


Figure 6.15. P-I curve for maximum wall displacement plotted with HySEA test results divided in displacement categories for Container 9.

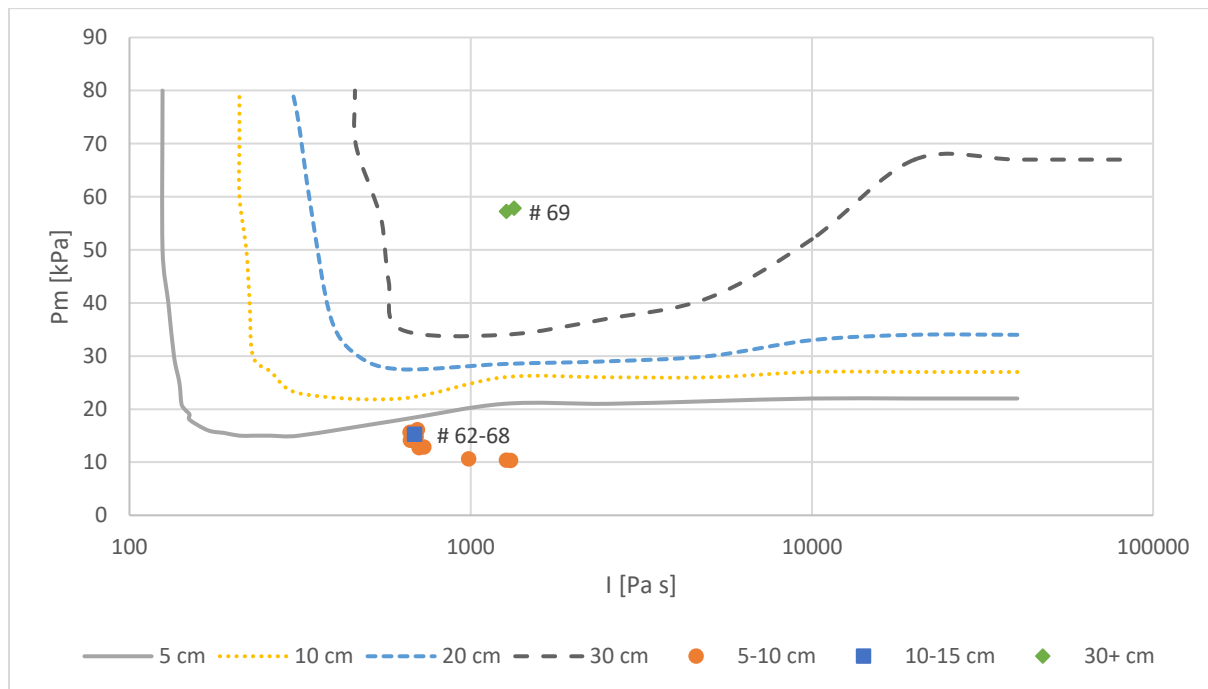


Figure 6.16. P-I curve for maximum wall displacement plotted with HySEA test results divided in displacement categories for Container 10.

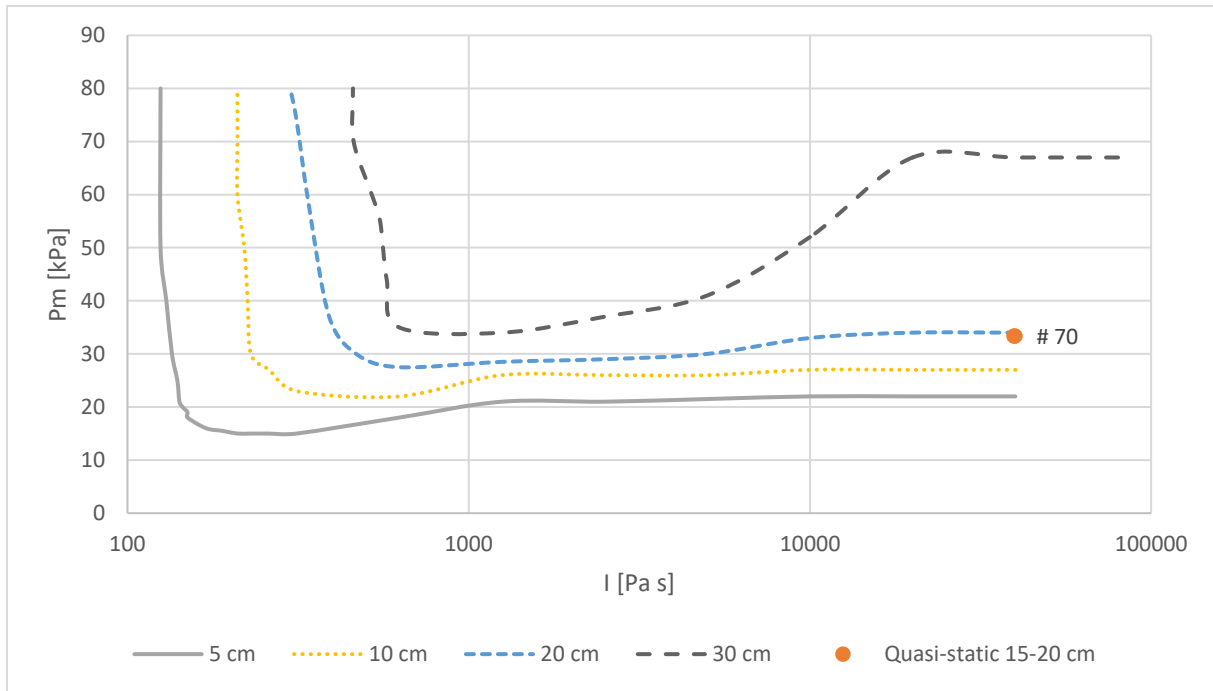


Figure 6.17. P-I curve for maximum wall displacement plotted with HySEA test results divided in displacement categories for Container 11.

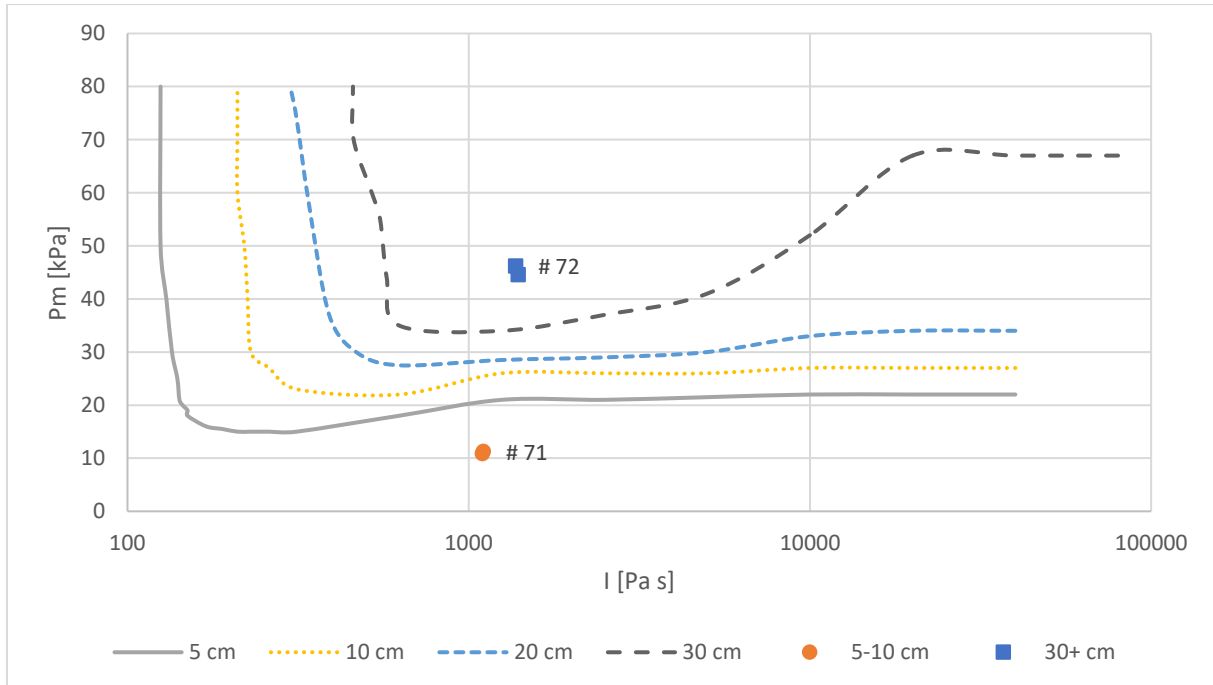


Figure 6.18. P-I curve for maximum wall displacement plotted with HySEA test results divided in displacement categories for Container 12.

6.2 Influence of steel strength on the structural response

A sensitivity study was conducted to look at the influence of different steel strengths on the structure. Simulations with two different steel strengths were conducted for comparison. The material yield strengths that were used were 235 and 355 MPa.

This was done by running the simulations for 5, 10, 20, and 30 cm with the original material yield strength of 355 MPa again with the same pressures and impulses, but with the material yield strength of 235 MPa. Tables 6.7 to 6.10 show the results obtained by the simulations.

Table 6.7. Simulated displacement results for 5 cm displacement with the material yield strength of 355 MPa and 235 MPa.

Study 3			Displacement [cm]	
Run	P_m [kPa]	I [Pas]	Material yield strength [MPa]	
			355	235
1	22	40000	5.053	19.52
2	22	20000	5.056	19.62
3	22	10000	5.083	19.97
4	21.5	5000	4.918	22.80
5	21.5	2500	5.174	26.36
6	21	1250	4.996	25.69
7	18	625	5.087	16.82
8	15	313	5.012	8.949
9	15	260	5.162	8.350
10	15	230	5.153	7.767
11	15	210	5.094	7.338
12	15.5	190	5.140	7.088
13	16	170	5.016	6.647
14	18	150	4.947	6.327
15	19	150	5.077	6.496
16	20	145	5.026	6.377
17	21	142	5.009	6.325
18	25	140	5.137	6.494
19	30	135	5.051	6.348
20	40	130	5.003	6.282
21	50	125	4.915	6.173
22	80	125	5.158	6.627

The figures below show the P-I curves for both material yield strengths of 355 MPa and 235 MPa. The P-I curve for material yield strength of 235 MPa was simulated in the same way as the one for 355 MPa with a few iterations. The results for plotting the 235 MPa curves are presented in further detail in Appendix E. Plotting them together shows the impact weaker steel has on the structure and in which region the steel strength has the most impact.

The results for the 5 cm P-I curve presented in Table 6.7 show that the highest increase in displacement for lower steel strength is around 21 cm. Figure 6.19 shows that the highest displacement increase is located in the quasi-static region.

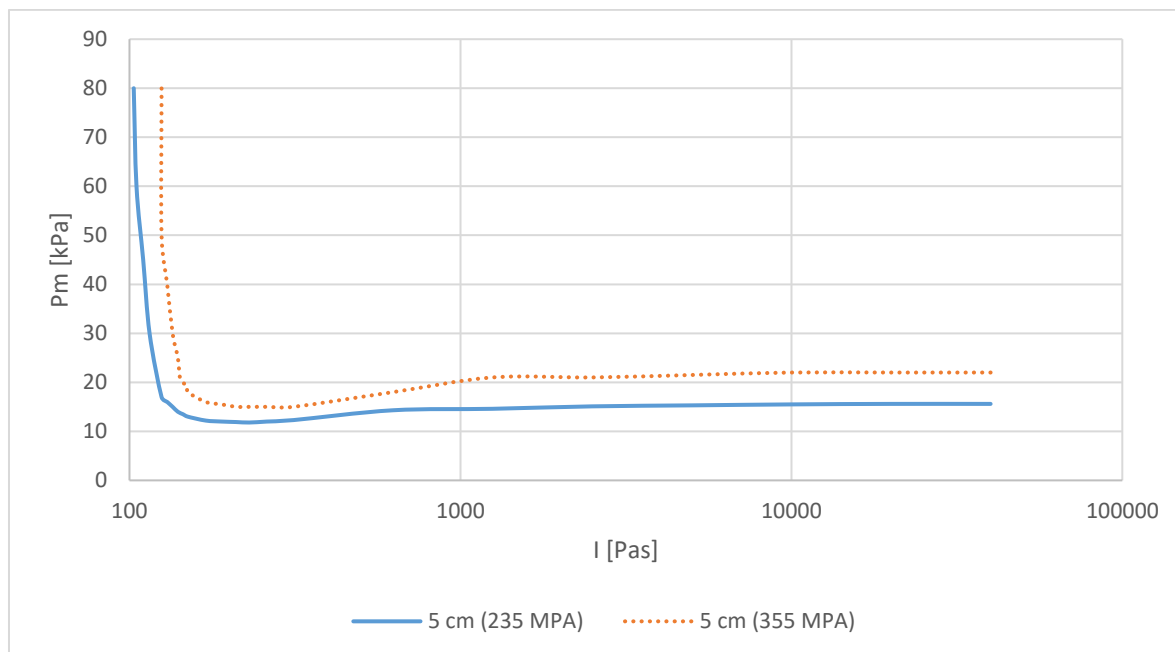


Figure 6.19. 5 cm P-I curves for steel with the material yield strength of 355 MPa and 235 MPa.

Table 6.8 shows the results for the 10 cm P-I curve. The highest increase in displacement was around 25 cm when reducing the steel strength to 235 MPa. Figure 6.20 shows that the greatest difference in the displacement values is located in the same region as for the 5 cm curve.

The displacement results for the 20 cm P-I curve presented in Table 6.9, increases significantly as the steel strength is reduced from 355 MPa to 235 MPa. At its maximum, it increases by around 18 cm. Comparing the results, the increase in displacement is highest for the P-I combinations in the quasi-static region, illustrated in Figure 6.21.

The displacement results for the P-I curve of 30 cm displacement simulated with steel strength of 235 MPa show a significant increase. The maximum increase is around 12 cm, and for this study, the highest difference in displacement is in the dynamic region, illustrated in figure 6.22.

Looking at the results, it is clear that the studies for 5 and 10 cm displacement experience the highest increase in displacement when the steel strength is reduced from 355 MPa to 235 MPa, compared to the studies for 20 and 30 cm displacement.

Table 6.8. Simulated displacement results for 10 cm displacement with the material yield strength of 355 MPa and 235 MPa.

Study 2			Displacement [cm]	
Run	P_m [kPa]	I [Pa s]	Material yield strength [MPa]	
			355	235
1	27	40000	10.05	24.14
2	27	20000	10.03	24.14
3	27	10000	10.46	24.57
4	26	5000	9.837	28.44
5	26	2500	9.890	32.63
6	26	1250	9.863	34.40
7	22	625	10.03	28.19
8	23	313	10.67	17.67
9	24	290	10.68	16.58
10	25	280	10.85	16.18
11	26	270	10.90	15.63
12	27	260	10.81	15.00
13	28	250	10.63	14.34
14	29	240	10.36	13.67
15	30	230	10.02	13.03
16	40	225	10.67	13.98
17	50	220	10.84	15.19
18	60	210	10.47	14.68
19	70	210	10.77	15.07
20	80	210	10.98	15.40

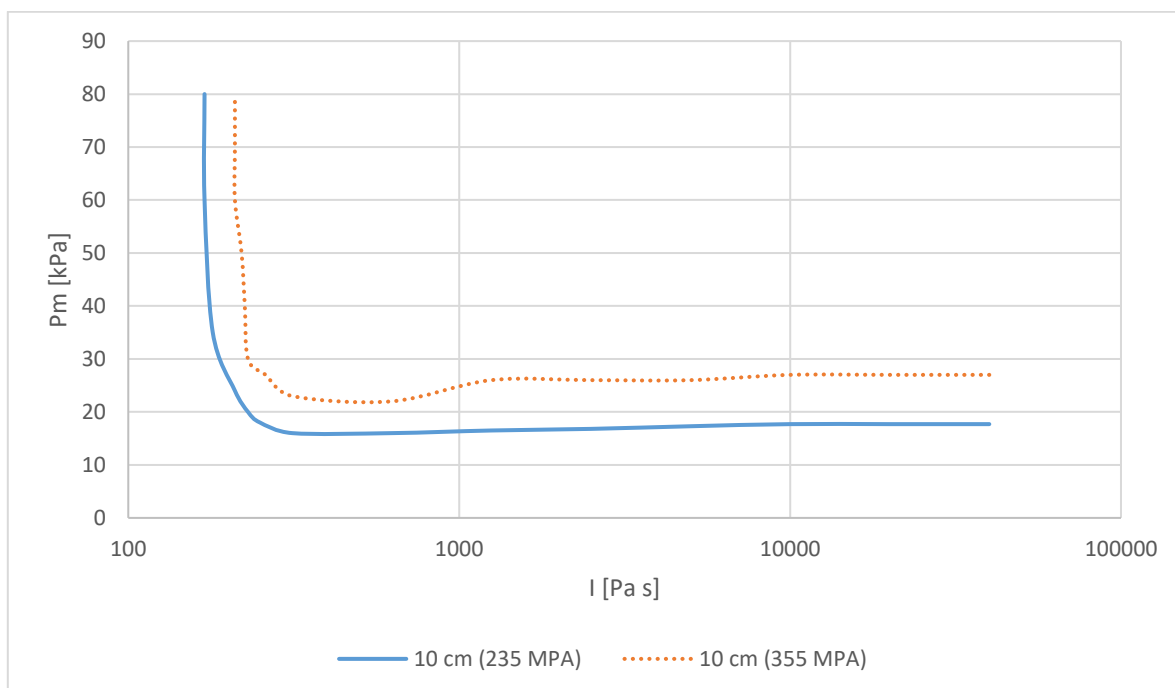


Figure 6.20. 10 cm P-I curves for steel with the material yield strength of 355 MPa and 235 MPa.

Table 6.9. Simulated displacement results for 20 cm displacement with the material yield strength of 355 MPa and 235 MPa.

Study 1			Displacement [cm]	
Run	P_m [kPa]	I [Pas]	Material yield strength [MPa]	
			355	235
1	34	40000	20.38	27.42
2	34	20000	20.42	27.43
3	33	10000	20.53	29.22
4	30	5000	20.15	31.45
5	29	2500	20.09	34.67
6	28.5	1250	19.76	37.50
7	27.5	625	20.44	36.75
8	30	468	20.74	33.07
9	37	390	20.80	26.68
10	58	340	20.54	27.96
11	74	313	20.99	27.04
12	80	300	20.02	26.26
13*	33.37035	39592.54	19.88	27.21
14*	33.38752	39866.78	19.89	27.21

*Values from quasi-static HySEA experiment for wall 1 (13) and 2 (14).

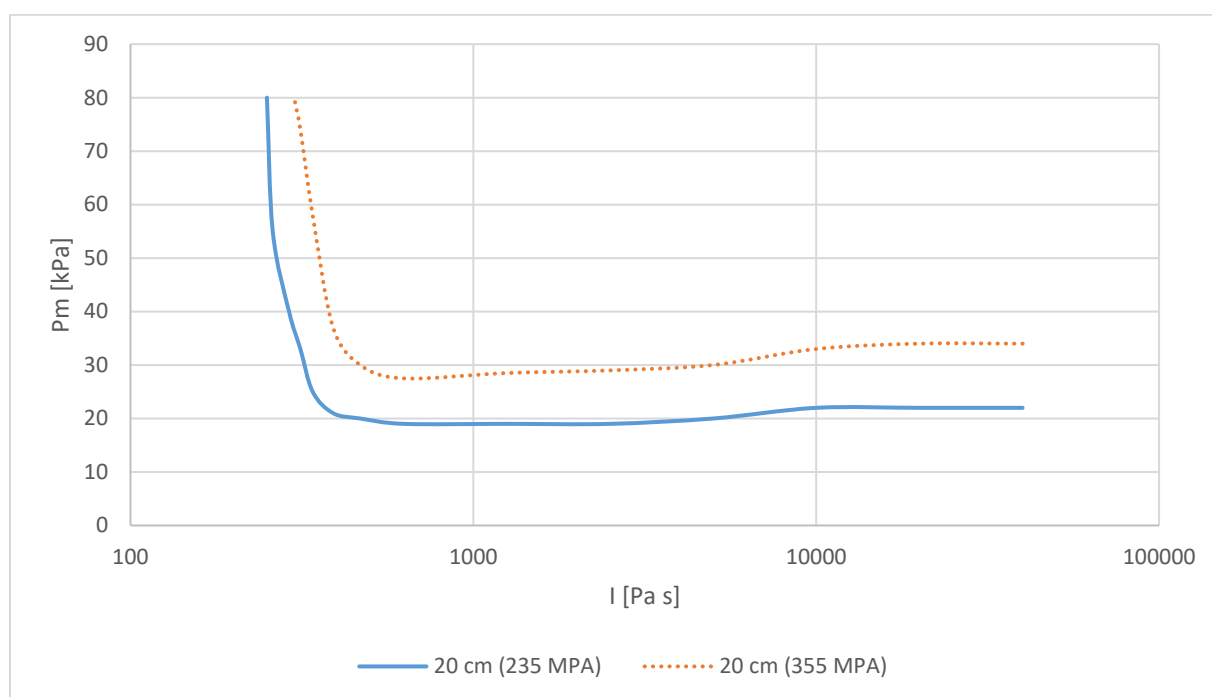


Figure 6.21. 20 cm P-I curves for steel with the material yield strength of 355 MPa and 235 MPa.

Table 6.10. Simulated displacement results for 30 cm displacement with the material yield strength of 355 MPa and 235 MPa.

Study 4			Displacement [cm]	
Run	P_m [kPa]	I [Pas]	Material yield strength [MPa]	
			355	235
1	67	80000	30.02	32.71
2	67	40000	30.02	33.06
3	67	20000	30.44	34.83
4	52	10000	30.24	35.45
5	41	5000	30.45	35.83
6	37	2500	30.58	36.86
7	34	1250	30.74	39.81
8	35	625	30.18	37.75
9	44	575	30.19	38.24
10	55	550	30.93	37.18
11	60	520	30.01	36.70
12	70	460	30.32	40.99
13	80	458	30.04	42.42
14	100	435	30.30	42.58
15	200	360	29.55	37.17
16	300	360	30.65	38.03
17	500	360	30.92	38.32

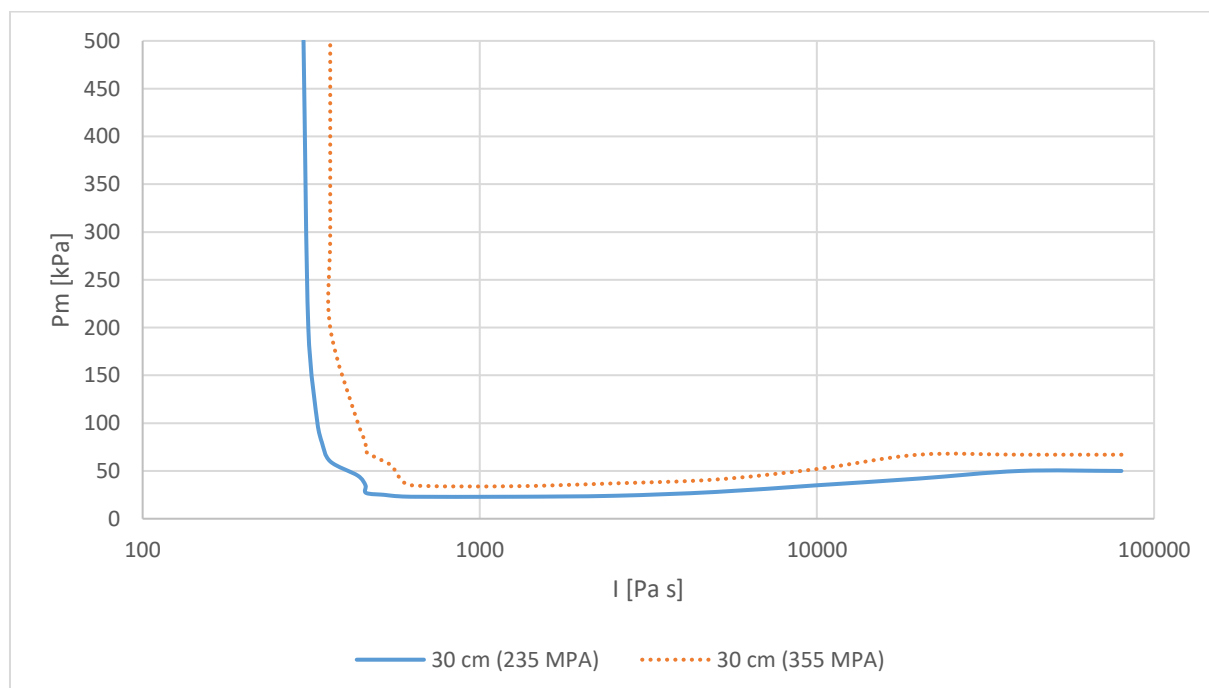


Figure 6.22. 30 cm P-I curves for steel with the material yield strength of 355 MPa and 235 MPa.

6.3 Structural response with a dent in the frame

Sensitivity studies were also conducted to look at how much a small dent in one of the walls would influence the structural response. This was done by making a small dent in the right wall, + x-direction, with a variable amp that could be changed from 0 to 1 depending on the desired damage. If amp equals 0 there is no damage, and if amp equal 1 there is maximum damage for the small dent in the wall. Figure 6.23 shows the three different sizes of dents that were simulated. Because of the layout of the finite element mesh, the dent was not exactly at the centre of the wall, but close.

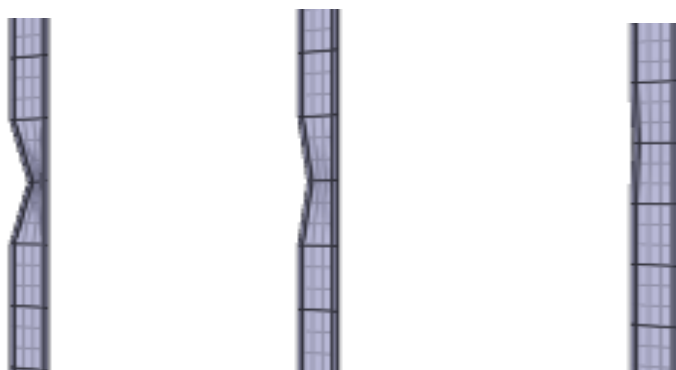


Figure 6.23. From left to right dent of size amp= 1, 0.5 and 0.1.

In the tables below the displacement of the wall with no dent, – x-direction, is compared to the wall with a dent, +x direction, for different dent sizes. The column furthest to the right shows the maximum displacement results of a structure without a dent.

For the study with a maximum wall displacement of 5 cm, Table 6.11 shows how a dent in the structure may increase the wall displacement significantly. The displacement for run 7 almost quadruples in size and increases with $\approx 200\%$ for the largest dent. For the smaller dent sizes, the displacement increases with $\approx 158\%$ for amp= 0.5 and $\approx 10\%$ for amp= 0.1. The smallest dent size does not have that great of an impact on the structure. Tables with the calculated increase in percentage are presented in Appendix F.

The larger the dent, the larger the wall displacement. This is expected when one of the walls is damaged and consequently weakening the structure. Table 6.11 shows that the wall displacement of the undamaged wall differs from the results for the structure with no dent. This shows that a dent does not only affect the response of the damaged wall but the entire structure. For this situation with a wall displacement of about 5 cm, the results show that the highest increase in displacement occurs in the dynamic region.

Table 6.11. Study for max wall displacement, $w_{max} = 5$ cm, with a dent in one wall and material yield strength of 355 MPa. Size of dent amp=0.1 vs 1 vs 0.5.

Run	Amp = 1		Amp = 0.5		Amp = 0.1		w_{max} [cm] without dent
	-X direction w_{max} [cm]	+X direction w_{max} [cm]	-X direction w_{max} [cm]	+X direction w_{max} [cm]	-X direction w_{max} [cm]	+X direction w_{max} [cm]	
1	6.802	17.36	6.356	14.69	5.103	5.453	5.053
2	6.806	17.40	6.368	14.83	5.118	5.488	5.056
3	6.930	17.71	6.532	15.36	5.175	5.525	5.083
4	6.935	18.28	6.562	16.29	4.983	5.251	4.918
5	8.635	19.96	7.232	17.49	5.187	5.486	5.174
6	9.201	24.08	6.552	16.93	5.031	5.537	4.996
7	6.798	20.39	5.204	12.06	5.100	5.404	5.087
8	5.266	13.52	5.026	8.319	5.015	5.255	5.012
9	5.216	13.03	5.156	8.072	5.162	5.428	5.162
10	5.114	12.28	5.137	7.779	5.151	5.406	5.153
11	5.046	11.28	5.075	7.499	5.092	5.326	5.094
12	5.081	10.20	5.116	7.364	5.137	5.371	5.140
13	4.966	9.254	4.999	6.991	5.014	5.218	5.016
14	4.890	8.521	4.926	6.684	4.945	5.132	4.947
15	5.005	8.632	5.050	6.852	5.074	5.278	5.077
16	4.963	8.409	4.998	6.720	5.023	5.220	5.026
17	4.943	8.292	4.982	6.654	5.006	5.190	5.009
18	5.081	8.400	5.111	6.774	5.133	5.325	5.137
19	5.003	8.454	5.027	6.586	5.048	5.201	5.051
20	4.944	8.288	4.971	6.552	4.999	5.193	5.003
21	4.851	8.017	4.880	6.465	4.910	5.137	4.915
22	5.056	8.328	5.090	6.848	5.145	5.441	5.158

Figure 6.24 shows the simulated structure for the first and the last run with different degrees of damage. The first run has higher values of impulse and lower values of pressure, and the last run has the opposite. The difference in the wall displacement is clearly shown in the simulated run for amp equals 1, but it is not always easy to see this difference in the simulated structure when the displacement difference is less. To illustrate the difference in displacement for the two walls the maximum and the minimum displacement for run 1 is plotted vs time in Figure 6.25.

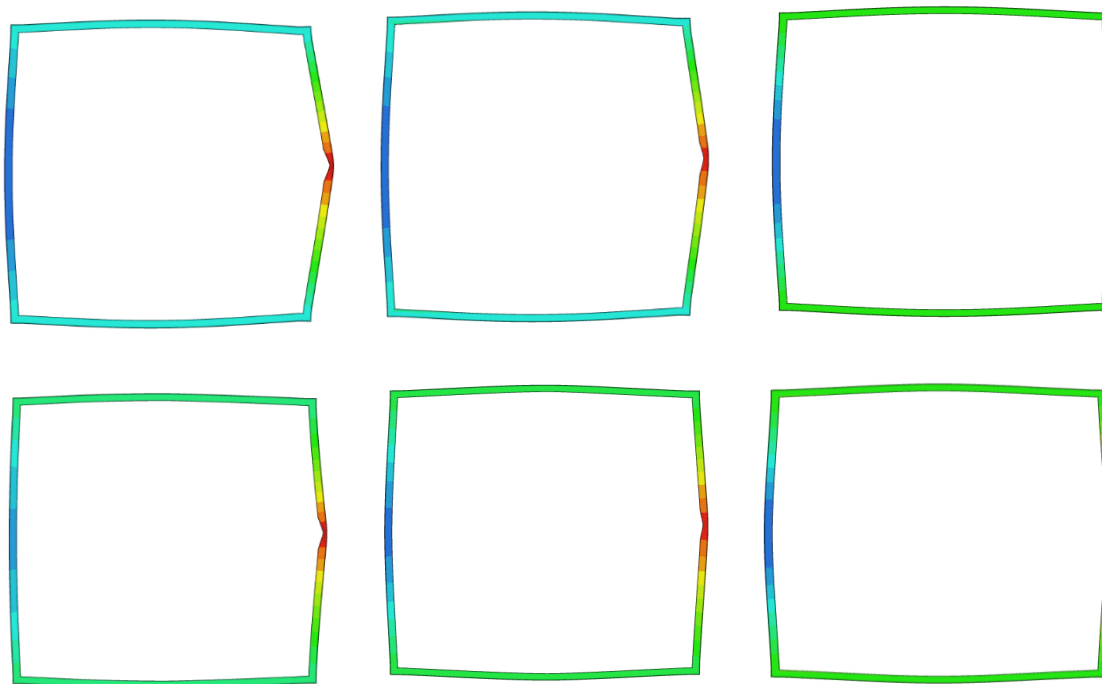


Figure 6.24. From top left to right: first run for 5 cm displacement for $amp=1, 0.5$ and 0.1 From bottom left to right last run for 10 cm displacement for $amp=1, 0.5$ and 0.1

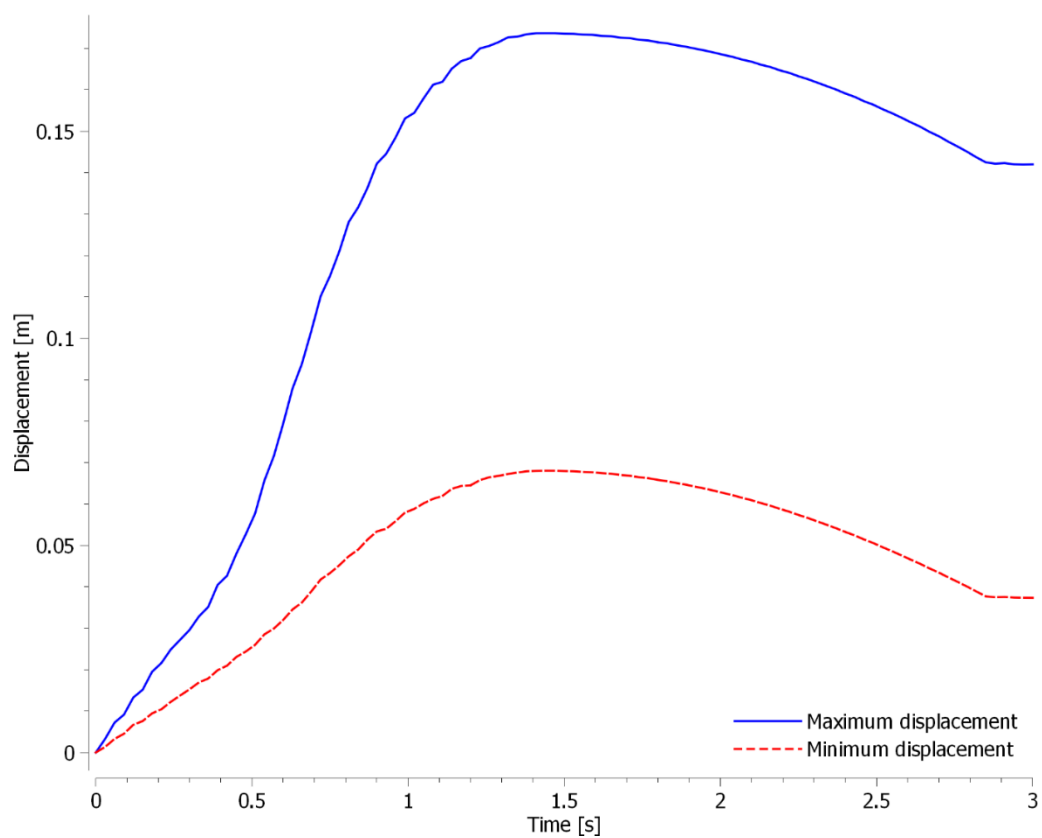


Figure 6.25. Run 1 for 5 cm displacement with dent size $amp=1$.

In the study for maximum wall displacement of 10 cm, the dent has a significant impact on the structural response. There is also an increase or a small decrease in the displacement of the wall without any damage compared to the structure without any dents. Table 6.12 shows that for some of the runs the displacement more than doubles for the wall with a dent. For the biggest dent size, the wall displacement increases at its highest with 166%. For lesser dent sizes, the highest displacement increase is $\approx 116\%$ for amp= 0.5 and $\approx 66\%$ for amp= 0.1. The highest displacement increase occurs in the dynamic region.

Table 6.12. Study for max wall displacement, $w_{max} = 10$ cm, with a dent in one wall and material yield strength of 355 MPa. Size of dent amp=0.1 vs 1 vs 0.5.

Run	Amp = 1		Amp = 0.5		Amp = 0.1		w_{max} [cm] without dent
	-x direction w_{max} [cm]	+x direction w_{max} [cm]	-x direction w_{max} [cm]	+x direction w_{max} [cm]	-x direction w_{max} [cm]	+x direction w_{max} [cm]	
1	12.04	20.79	11.73	19.62	10.86	14.78	10.23
2	12.16	20.83	12.24	19.72	11.25	14.98	10.20
3	12.16	21.05	13.09	20.37	12.01	15.81	10.40
4	11.35	20.92	14.61	21.66	10.80	16.42	10.48
5	15.06	24.21	12.84	24.64	10.13	16.85	10.65
6	14.59	30.64	11.95	25.81	10.05	15.83	9.879
7	9.866	26.25	9.807	20.61	9.959	12.19	9.561
8	10.31	20.74	10.47	15.71	10.66	11.97	10.43
9	10.34	19.26	10.50	15.13	10.67	11.97	10.03
10	10.51	18.69	10.68	15.03	10.84	12.14	10.90
11	10.64	18.20	10.73	14.83	10.89	12.15	9.595
12	10.59	17.69	10.68	14.55	10.81	12.06	10.26
13	10.40	17.07	10.50	14.19	10.62	11.85	10.65
14	10.14	16.33	10.24	13.77	10.35	11.54	10.23
15	9.777	15.49	9.916	13.29	10.01	11.16	10.79
16	10.47	16.11	10.57	14.01	10.67	11.99	10.52
17	10.68	16.91	10.74	14.27	10.84	12.16	10.26
18	10.26	16.91	10.34	13.91	10.45	11.60	10.74
19	10.52	17.51	10.62	14.33	10.76	11.84	9.899
20	10.75	17.87	10.83	14.65	10.96	12.05	10.32

Figure 6.26 illustrates the simulated structure highlighting the difference in the wall displacement. It shows how the wall damaged by the dent has a higher value of displacement, and how this difference in displacement becomes less with smaller dents. Figure 6.27 shows the difference in displacement plotted vs time for the first run.

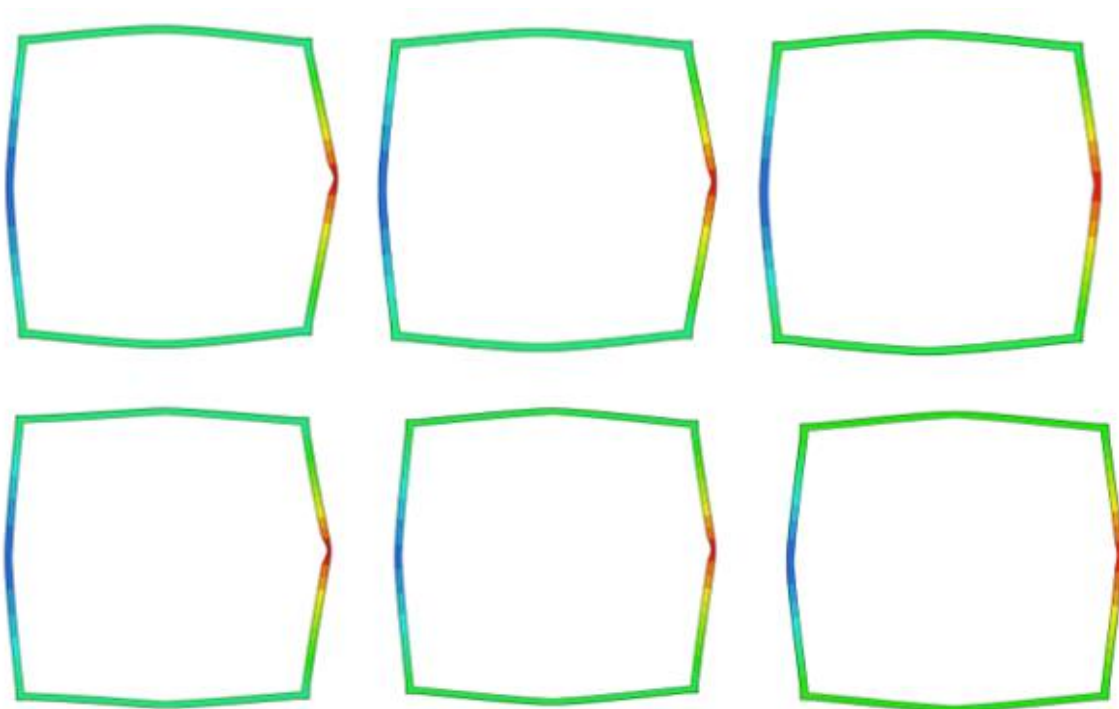


Figure 6.26. From top left to right: first run for 10 cm displacement for amp= 1, 0.5 and 0.1 From bottom left to right last run for 10 cm displacement for amp= 1, 0.5 and 0.1

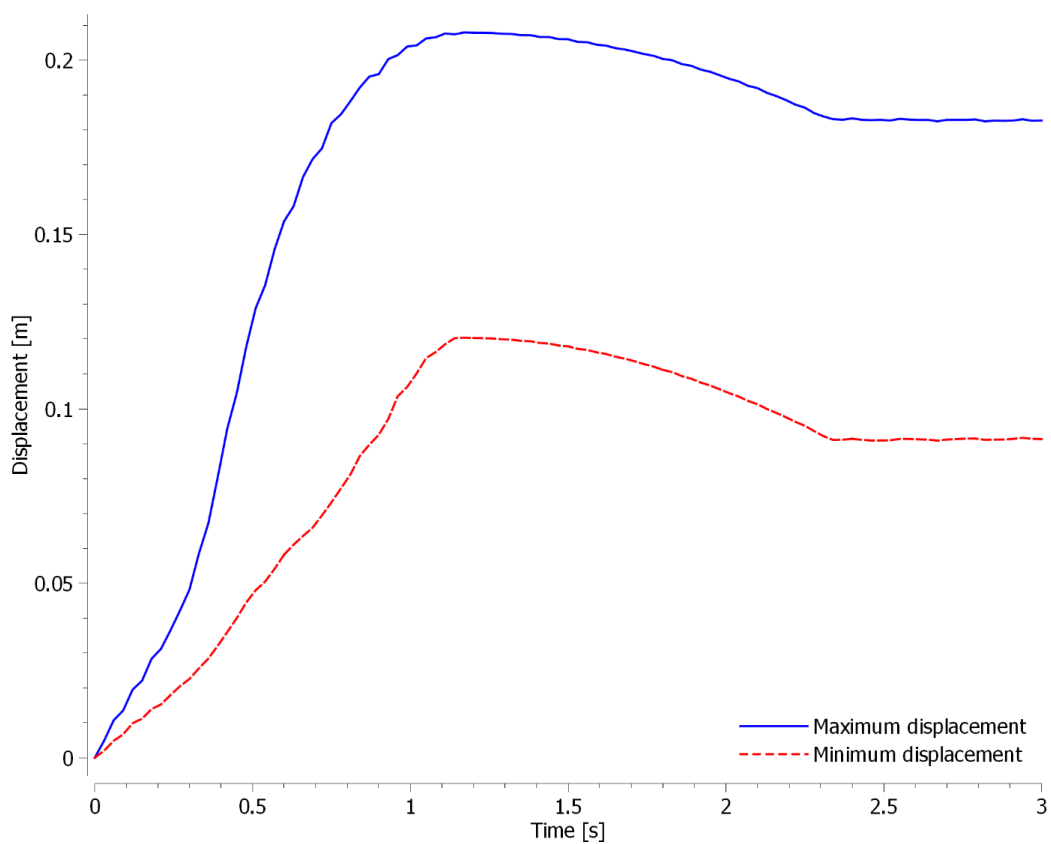


Figure 6.27. Run 1 for 10 cm displacement with dent size amp= 1.

For the study with a maximum wall displacement of 20 cm, the results in Table 6.13 show a small difference in the wall displacement for the wall with a dent compared to the wall without a dent. The wall with a dent has a greater wall displacement. The results clearly show this, especially for the two situations with the biggest damage, for amp equals 1 or 0.5. At its highest, the wall displacement increased with $\approx 57\%$ for amp equal 1, and $\approx 49\%$ for amp equal 0.5. For the smallest dent, amp = 0.1, the wall displacement increased at its maximum with $\approx 19\%$.

Figure 6.28 shows the two simulated P-I curves with a displacement of around 20 cm for a simplified structure with and without a dent. The curves in the figure show that the highest increase in displacement occurs in the dynamic region and how much a small dent influences the structural response. A small dent reduces the strength of the structure and material and allows the same displacement to occur with lower pressures and impulses.

The simulated structure is illustrated in Figure 6.29 for different den sizes which shows how the dent size influences the structural response. The great difference in displacement is plotted vs time in Figure 6.30.

Table 6.13. Study for max wall displacement, $w_{max} = 20$ cm, with a dent in one wall and material yield strength of 355 MPa. Size of dent amp=0.1 vs 1 vs 0.5.

Run	Amp = 1		Amp = 0.5		Amp = 0.1		w_{max} [cm] without dent
	-X direction w_{max} [cm]	+X direction w_{max} [cm]	-X direction w_{max} [cm]	+X direction w_{max} [cm]	-X direction w_{max} [cm]	+X direction w_{max} [cm]	
1	21.16	23.57	20.97	23.29	20.58	21.41	20.38
2	21.14	23.66	21.14	23.34	21.04	21.57	20.42
3	21.85	24.27	21.58	23.90	21.59	22.13	20.53
4	23.19	23.85	24.66	25.96	21.27	23.80	20.15
5	27.74	29.08	23.94	29.35	20.45	24.32	20.09
6	21.92	33.40	20.70	30.97	19.84	23.65	19.76
7	20.78	32.63	20.34	29.04	20.42	22.74	20.44
8	20.75	30.77	20.59	27.44	20.69	22.68	20.74
9	21.10	29.69	20.66	26.60	20.76	22.72	20.80
10	20.68	28.35	20.49	26.23	20.59	23.07	20.54
11	20.73	26.82	20.82	25.22	20.96	22.23	20.99
12	19.72	25.77	19.84	24.17	19.98	21.22	20.02

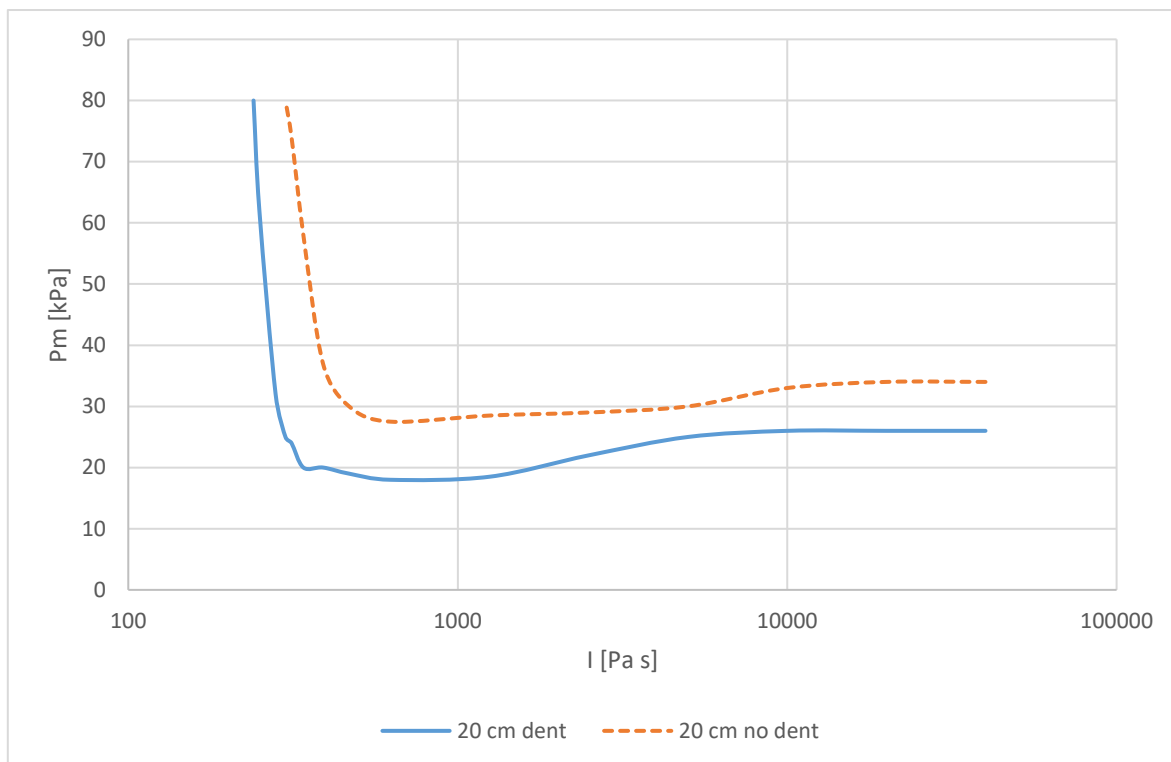


Figure 6.28. *P-I* curves for around 20 cm wall displacement for the simplified structure with and without a dent.

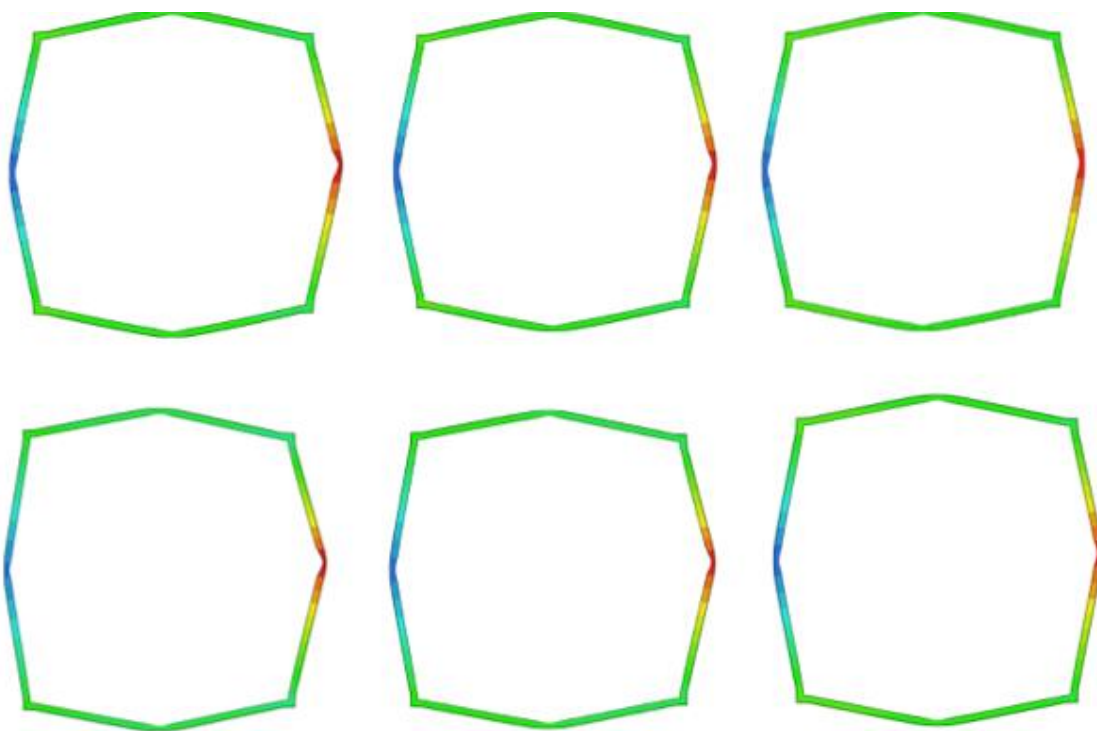


Figure 6.29. From top left to right: first run for 20 cm displacement for amp= 1, 0.5 and 0.1 From bottom left to right last run for 20 cm displacement for amp= 1, 0.5 and 0.1

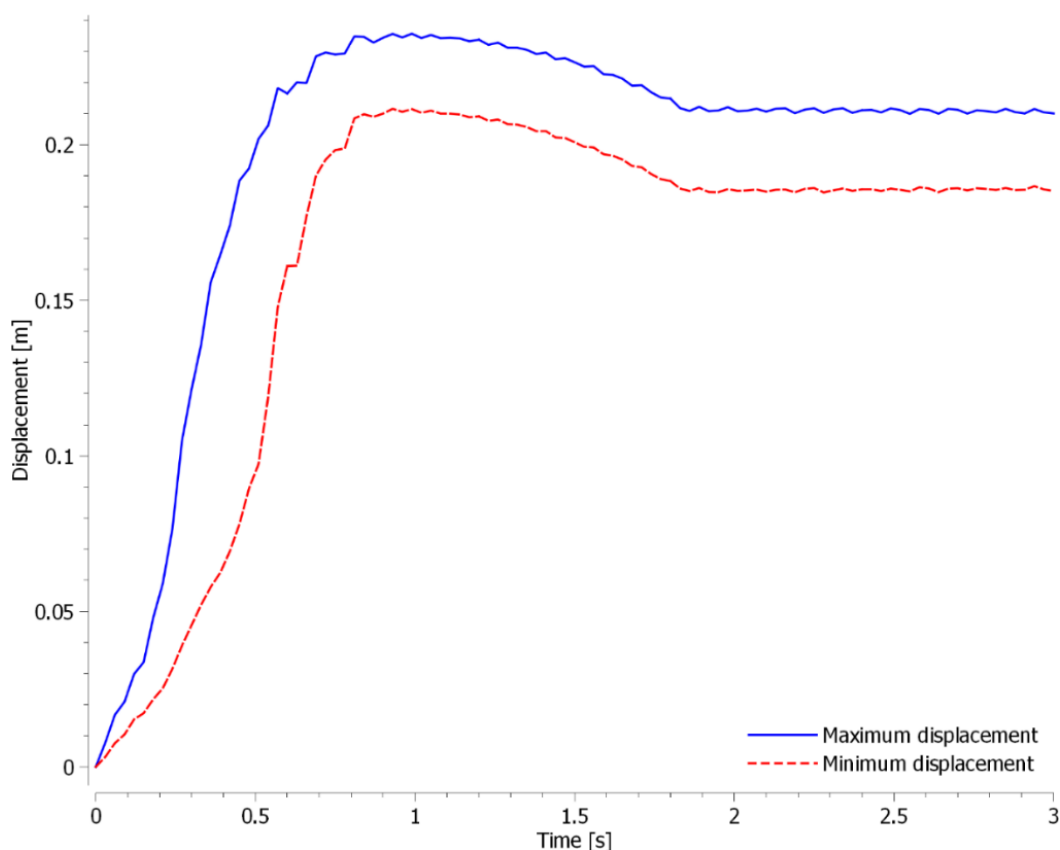


Figure 6.30. Run 1 for 20 cm displacement with dent size amp= 1.

When it comes to the study with a maximum wall displacement of 30 cm, Table 6.14 shows that the difference in displacement is less compared to the studies conducted with smaller displacement. For the different sized dents, amp = 1, 0.5 and 0.1, displacement increased with $\approx 39\%$, $\approx 36\%$ and $\approx 28\%$, respectively. Table 6.14 show that the wall without the dent has a slightly higher value of displacement for some of the runs with high impulse. These values are emphasized with bold font in the table. In the quasi-static region, the duration of the load is long with high impulse, and the walls pulsated back and forth at high displacements. Figure 3.42 shows the comparison of the first run in the quasi-static region and the last run in the impulsive region. For larger wall displacement and pressures the structure experience significant deformation, and a small dent has less effect on the structural response compared to the previous studies with smaller displacements. Figure 6.32 shows the displacement of the walls for run 1. The previous studies showed that the wall with the dent was less stiff and as a result had higher displacement. For this study, the wall with the dent is less stiff until the curves intersect and the wall without a dent achieves greater wall displacements. This is the only study out of the four where this effect occurred. Reasons for this dynamic effect are uncertain, but the dent may make the wall stiffer in the quasi-static region when pressures are higher resulting in a slightly smaller displacement compared to the other wall.

Table 6.14. Study for max wall displacement, $w_{max} = 30$ cm, with a dent in one wall and material yield strength of 355 MPa. Size of dent amp=0.1 vs 1 vs 0.5.

Run	Amp = 1		Amp = 0.5		Amp = 0.1		w_{max} [cm] without dent
	-x direction w_{max} [cm]	+x direction w_{max} [cm]	-x direction w_{max} [cm]	+x direction w_{max} [cm]	-x direction w_{max} [cm]	+x direction w_{max} [cm]	
1	30.02	28.74	30.00	29.37	30.05	29.90	30.02
2	30.24	29.06	30.58	29.99	30.15	29.95	30.02
3	32.44	31.01	31.38	31.01	30.61	30.68	30.44
4	33.38	30.90	32.65	32.04	30.59	30.70	30.24
5	33.40	31.59	33.01	34.09	30.47	30.35	30.45
6	35.49	36.51	32.56	35.26	30.94	31.82	30.58
7	31.88	35.75	31.31	34.66	30.84	32.19	30.74
8	30.25	38.30	30.22	36.08	30.21	32.07	30.18
9	32.40	41.20	30.75	39.59	30.52	36.18	30.19
10	33.04	45.21	31.84	42.66	30.98	39.22	30.93
11	31.96	44.57	31.18	42.27	30.08	38.56	30.01
12	30.44	40.17	29.47	38.94	30.26	35.69	30.32
13	30.81	41.03	30.58	40.07	30.11	36.96	30.04
14	30.83	40.05	30.63	39.32	30.33	36.63	30.30
15	29.49	34.63	29.51	33.78	29.54	31.10	29.55
16	30.65	34.87	30.66	34.10	30.65	31.68	30.65
17	30.91	35.02	30.93	34.26	30.92	31.88	30.92

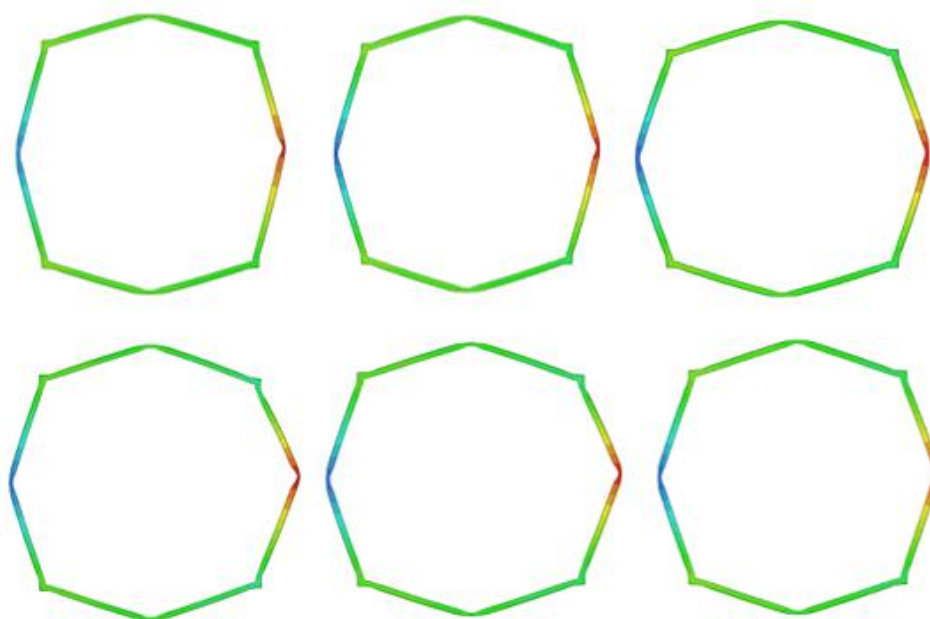


Figure 6.31. From top left to right: first run for 30 cm displacement for amp= 1, 0.5 and 0.1 From bottom left to right last run for 10 cm displacement for amp= 1, 0.5 and 0.1

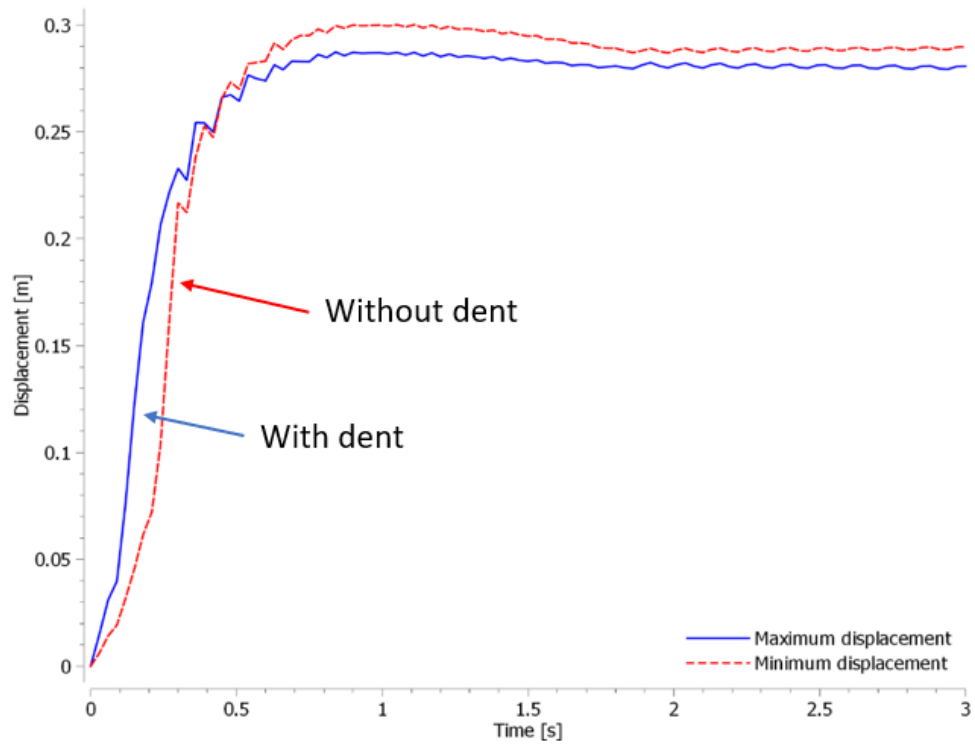


Figure 6.32. Run 1 for 30 cm displacement with dent size $amp=1$.

6.4 Harmonic vs triangular pressure load

In this section, the results from comparing the “harmonic” and triangular load are presented. The influence of rise time on the P-I curve was also studied closer with a rise time relation of $t_r = 0.5 t_d$ and $t_r = 0.000001 t_d \approx 0$. Figure 5.8 shows the relation between impulse (I), peak pressure (P_m), and the duration of the load (t_d) for a triangular load. These studies were carried out not only to compare the different loads, but also to compare the results with previous conclusions from literature, and to check the accuracy of the model.

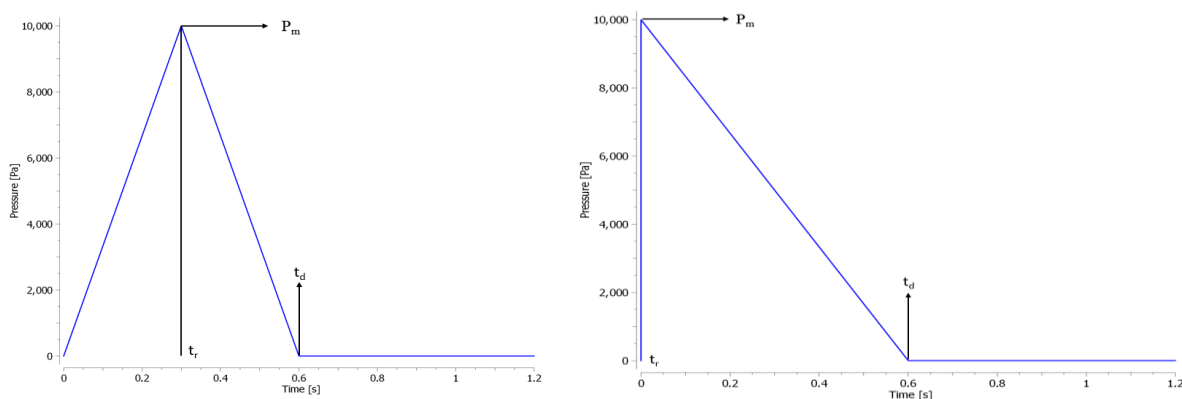


Figure 6.33. Illustration of the triangular loads with different rise times used in the simulation. To the left $t_r = 0.5 t_d$ and to the right $t_r = 0 t_d$.

Figure 6.33 shows the two different triangular loads used in the simulations. The influence of different rise time was only carried out for the study with a maximum wall displacement of 20 cm. The simulations that were carried out for the harmonic sinus load were modified to run with triangular loads and then compared with the triangular loads with different rise times. The simulations for the triangular loads with different rise times were carried out using the same methods as previous simulations with a few iterations. The results from these simulations are presented in Tables H1 and H2 in Appendix H. The results were then plotted to create P-I curves in the same figure as the curve created from the harmonic load.

Figure 6.34 shows that the P-I curve from the harmonic sinus load has approximately the same characteristics as a curve for a nonideal explosion with finite rise time presented in Figure 4.1 by Baker et al. (1983). The curve with \approx zero rise time shows the same characteristics as a curve for an ideal explosion, and the curve with a rise time relation of $t_r = 0.5 t_d$ shows a great correlation to the curves Krauthammer et al. (2008) presented in Figure 4.7. The results obtained from the different triangular loads where the quasi-static asymptote moves to higher values when the relation increases, agrees well with what Krauthammer et al. (2008) presented.

When comparing the harmonic sinus load with the triangular load, the harmonic load is best suited for the complex situations with a non-ideal explosion in an enclosed environment. The harmonic load gives curves with characteristics closest to the curves from the literature. The results from the simulations with Impetus Afea Solver showed a good correlation with previous results and conclusions.

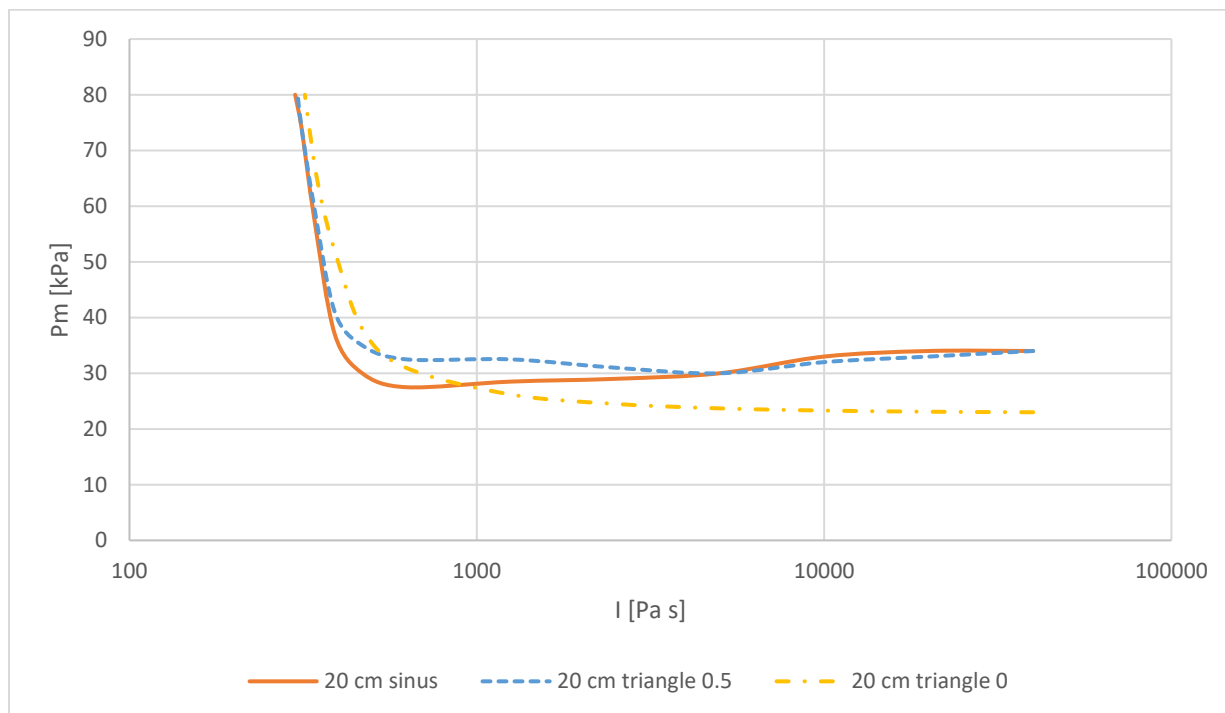


Figure 6.34. P-I curve for 20 cm wall displacement from harmonic load compared to a triangular load with different rise times.

6.5 20 cm P-I curve compilation

This section presents a compilation of different P-I curves that creates a “band” where the width of the “band” represents the effect of material strength, wall imperfection, and pressure-time curve shape.

Figure 6.35 shows the different curves creating the “band” together with the unique experimental data from the HySEA project with error bars. These error bars indicate the spread from minimum to maximum values in the measured results from the different pressure sensors in the experiment. The different curves all have the same maximum wall displacement of around 20 cm. The width of the band shows how differences in material, wall imperfections, and the shape of the pressure load influence the result. The different curves in Figure 6.35 show that reduced material yield strength approximately has the same influence on the structure as a dent.

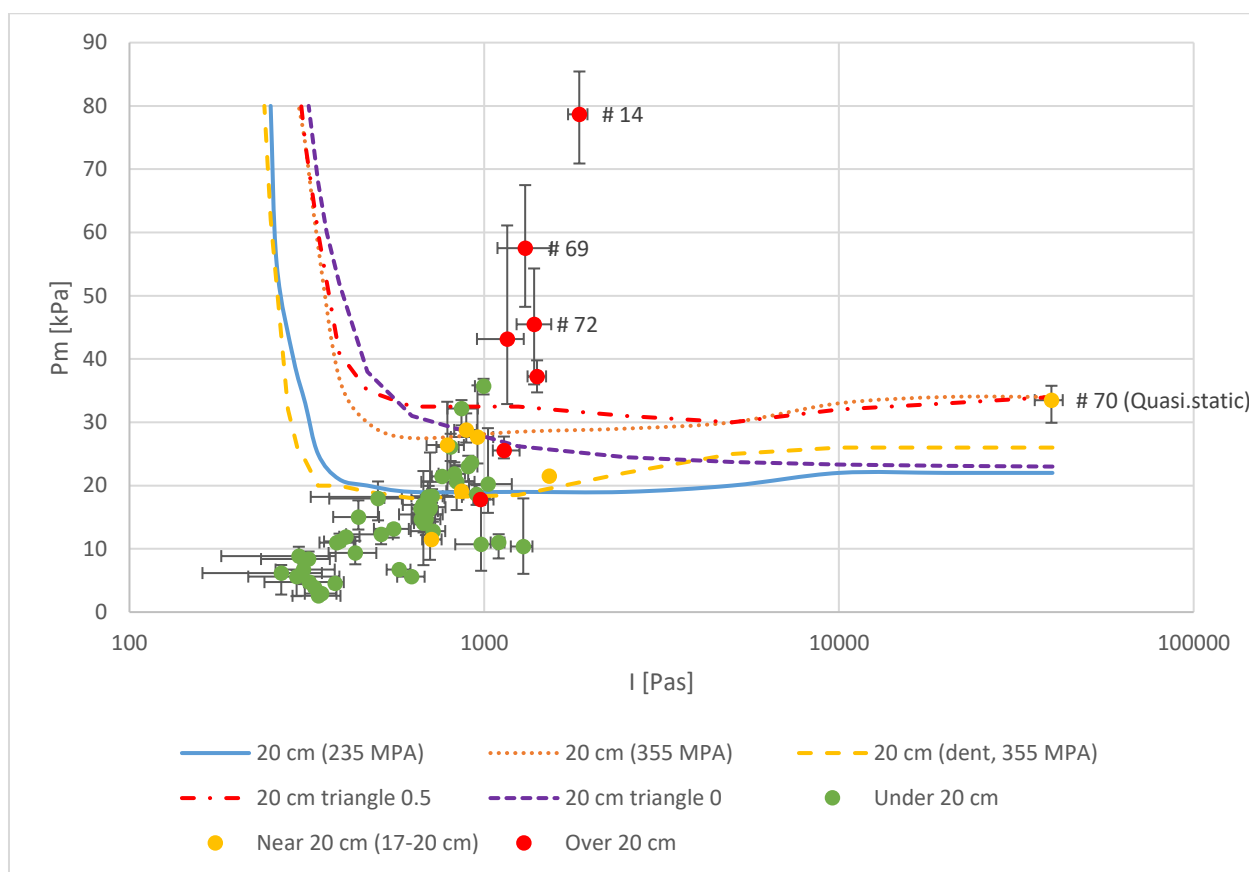


Figure 6.35. Compilation of 20 cm P-I curves resulting in a “band” representing the effect of material strength, wall imperfection, and pressure-time curve shape.

There are significant uncertainties associated with the experimental results. Most containers were used in several tests and permanent deformation from previous tests may influence the test results significantly, together with uncertainties in the measuring devices, material, and

the influence of resonance. The experimental data is categorized in different displacement categories illustrated in Figure 6.35. The tests with maximum wall displacement near 20 cm (between 17-20 cm) were tests 7, 12, 20, 29, 57, 60, and 70. Test 8, 13-15, 69, and 57 resulted in maximum wall displacement greater than 20 cm. The remaining tests resulted in maximum wall displacement under 20 cm.

Table 6.2 presented the results from simulations using selected pressure-time histories from the experiment. The results show that the simulated maximum wall displacement agreed well with the positioning of the experimental tests in the P-I diagram. The measured displacement is likely higher in some tests due to the influence of different uncertainties. Considering the error in the experimental data, the different factors influencing the maximum wall displacement and the results obtained in Table 6.2 the points are within reasonable limits.

7 Conclusion and suggestion for further work

This thesis explores the use of P-I diagrams to assess the structural damage to containers subjected to internal pressure loads from vented hydrogen deflagrations. The approach adopted entailed the use of the finite element tool Impetus Afea to create P-I curves representing the structural response of a 20-foot shipping container subjected to internal pressure loads with specified shape, pressure and impulse, corresponding to a specific level of maximum wall displacement. The analysis also included sensitivity studies with respect to material strength, damage to the structure, and the shape of the pressure load.

The numerical model of the 20-foot shipping container was developed from a quasi-static experiment conducted as part of the HySEA project. This model was then used to generate P-I curves for 5, 10, 20, and 30 cm wall displacement. The characteristic properties of the curves agreed well with the theory for non-ideal explosion with finite rise time. When comparing the simulated curves with the experimental results, most of the experimental results were in the dynamic region. The experimental results were divided into different displacement groups. There were some deviations when comparing the simulated curves with the experimental result. These can most likely be explained by inherent uncertainties associated with both the numerical model and the experimental results. The maximum wall displacement measured in the experiment was likely influenced by factors such as previous damage (used containers), deformation from previous experiments (most containers were used in several tests), as well as multiple pressure peaks and resonance. This may have resulted in higher measured maximum wall displacements for some of the experimental tests compared to the simulated maximum wall displacement. The result summarised in Table 6.2 shows that the simulated maximum wall displacements using the measured complex pressure-time histories from selected tests agree well with the positioning of the experimental tests in the P-I diagram. Detailed elements on the structure that may influence the structural response, such as hinges and doors, were excluded in the simplified model. Even though the simplified model does not replicate the experiment exactly, and deviations from the experimental result occur, the model captures the most important effects, such as the influence of different P and I values and changes in material or geometry. Despite the deviations between model predictions and experiments, the use of P-I diagrams can be valuable for safety and design purposes. The primary limitation from an engineering design point of view will most likely be the reliable prediction of the relevant pressure loads for a given structure. It is not straightforward to predict relevant pressure loads in vented deflagrations, as Skjold et al. (2019a, d) demonstrated in two blind-prediction benchmark studies. Consequently, improvements in predictive capabilities are necessary.

The sensitivity study carried out on the existing model to investigate the influence of reducing the material yield strength revealed a significant increase in the maximum wall displacement for a reduction from 355 MPa to 235 MPa. The highest increase of the displacement occurred

in the quasi-static region, for the 5, 10, and 20 cm displacement curves, while it occurred in the dynamic region for the 30 cm displacement curve. The studies for 5 and 10 cm displacement had the highest increase in displacement when the steel strength was reduced compared to the other studies.

Some degree of damage to used shipping containers is inevitable, and will affect the structural response if the structure is subjected to an internal pressure load. The sensitivity study conducted to look at the effect of a dent on the structure demonstrates that a damaged wall has greater maximum displacement compared to an intact wall. The numerical results showed that by increasing the dent size the displacement increased. Compared to the results for an intact container, a dent does not only affect the damaged wall but the whole structure. The studies for maximum wall displacement of 5 and 10 cm had the highest increase in displacement for the wall with a dent. The studies for maximum wall displacement of 20 and 30 cm did not have such a significant difference in the displacement of the two walls. The structural response was most sensitive to a dent in the dynamic region.

Looking at the comparison of the harmonic and triangular load, their characteristics corresponded well with previous theory and studies. The numerical results showed that by utilizing the harmonic pressure load the P-I curves obtained characteristics closest to the curves for nonideal explosions with finite rise time presented by Baker et al. (1983).

P-I diagrams are useful for assessing the structural response of structures subjected to different types of loads. In this study, the structural response of a container was studied numerically with a simplified model utilizing the finite element tool Impetus Afea Solver and unique experimental data conducted as part of the HySEA project to look at the maximum displacement of the walls.

Suggestions for further work include:

- Explore other FE methods and geometry models for comparison.
- Simulate more complex structures, e.g. the entire container, including more details, such as weak points to look at permanent damage/- breakage.
- Produce P-I diagrams for permanent deformation.
- Looking at the influence of structural damage from previous tests on the structure by including data from former simulations in the next simulation.

- Make the 5, 10, and 30 cm P-I diagrams as “bands” where the width of the band could represent the gathered information on the effect of material strength, wall imperfections, and pressure-time curve shape.
- Utilize the complex pressure-time histories from the HySEA experiment for the remaining tests in Impetus Afea to calculate resulting maximum wall displacement for comparison with P-I curves and experimental displacement results.
- Test samples from the containers used in the HySEA experiments to determine material properties.

Bibliography

- Aarnes, J., Eijgelaar, M., & Hektor, E. A. (2018). *Hydrogen as an energy carrier: An evaluation of emerging hydrogen value chains*. Report: DNV-GL.
- Abedini, M., Mutalib, A. A., Raman, S. N., Alipour, R., & Akhlaghi, E. (2018). *Pressure–Impulse (P–I) Diagrams for Reinforced Concrete (RC) Structures: A Review*. *Archives of Computational Methods in Engineering*, 26:733–767.
- Arnold, C. (2006). Chapter 4 - Earthquake effects on buildings. I *Designing for Earthquakes* (ss. 1-27). The Earthquake Engineering Research Institute (EERI).
- ASCE. (2010). *Design of Blast-Resistant Buildings in Petrochemical Facilities* (2nd. ed.). American Society of Civil Engineers.
- Atanga, G., Lakshmipathy, S., Skjold, T., Hisken, H., & Hanssen, A. G. (2019). *Structural response for vented hydrogen deflagrations: Coupling CFD and FE tools*. *International Journal of Hydrogen Energy*, 44:8893-8903.
- Babrauskas, V. (2003). *Ignition Handbook* (1st. ed.). Issaquah: Fire Science Publishers.
- Baker, W. E., Cox, P. A., Westine, P. S., Kulesz, J. J., & Streholw, R. A. (1983). *Explosion hazards and evaluation*. Elsevier: Amsterdam.
- Bangash, M. Y., & Bangash, T. (2006). *Explosion-Resistant Buildings*. Springer: London.
- Biggs, J. M. (1964). *Introduction to Structural Dynamics* (1st. ed.). McGraw-Hill Inc: New York.
- Bjerketvedt, D., Bakke, J. R., & Wingerden, K. v. (1997). *Gas Explosion Handbook*. Christian Michelsen Research AS. Bergen: *Journal of Hazardous Materials*, 52: 1-150.
- Blasko, J., Krauthammer, T., & Astarlioglu, S. (2007). *Pressure–impulse diagrams for structural elements subjected to dynamic loads*. The Pennsylvania State University: Technical report PTC-TR-002-2007. University Park, PA: Protective Technology Center.
- Chen, A. (2014). *Structural Response to Vapour Cloud Explosions*. London: Department of Civil and Environmental Engineering Imperial College London.
- Colombo, M., & Martinelli, P. (2012). *Pressure–impulse diagrams for RC and FRC circular plates under blast loads*. Milan: *European Journal of Environmental and Civil Engineering*, 16: 837-862.
- Cormie, D., Mays, G., & Smith, P. (2009). *Blast effects on buildings* (2nd. ed.). thomas telford: London.
- Doormaal, A. v., Haberacker, C., Hüsken, G., Larcher, M., Saarenheimo, A., Solomos, G., . . . C, K. (2013). *Resistance of structures to explosion effects: Review report of testing methods*. European Commission: Luxembourg.
- Eckhoff, R. K. (2016). *Explosion hazards in the process industries*. Elsevier: Amsterdam.

- European Commission (EU). (2020). *A hydrogen strategy for a climate-neutral Europe*. Brussel, 8 July 2020.
- Fallah, A., & Louca, L. (2007). *Pressure–impulse diagrams for elastic-plastic-hardening and softening single-degree-of-freedom models subjected to blast loading*. *International Journal of Impact Engineering*, 34:823–842.
- Hanssen, A. G. (2020). *Simplified container model as basis for P-I diagrams*. Note. Impetus: Flekkefjord.
- Jansen, C. M., van den Bosch, C. J., Merx, W. P., & de Weger, D. (1992). *Methods for the determination of possible damage* (1st. ed.). The Director-Geberal of Labour: Voorburg.
- Johansson, M., & Laine, L. (2007). *Bebyggelsens motståndsförmåga mot extrem dynamisk belastning*. Räddningsverket: Karlstad.
- King, R. (1990). *Safety in the process industries*. Butterworth-Heinemann: Oxford.
- Krauthammer, T., Astarlioglu, S., Blasko, J., Soh, T. B., & Ng, P. H. (2008). *Pressure–impulse diagrams for the behavior assessment of structural components*. *International Journal of Impact Engineering*, 35: 771–783.
- Li, Q., & Meng, H. (2002). *Pressure–impulse diagram for blast loads based on dimensional analysis and single-degree-of-freedom model*. *Journal of Engineering Mechanics*, 128: 87–92.
- Lien, J. R., & Løvhøiden, G. (2001). *Generell fysikk for universiteter og høyskoler: bind 1 mekanikk* (2nd. ed.). Universitetsforlaget: Oslo.
- Logan, D. L. (2012). *A first course in the finite element method*. (5th. ed.). Cengage Learning.
- MARSH. (2018). *The 100 Largest Losses 1978-2017*. Report: MARSH & McLENNAN Companies.
- Molkov, V. (2015). *Fundamentals of Hydrogen Safety Engineering I*. The eBook company.
- Najjar, Y. S. (2013). *Hydrogen safety: The road toward green technology*. Jordan: *International Journal of Hydrogen Energy*, 38: 10716-10728.
- Ng, H. D., & Lee, J. H. (2007). *Comments on explosion problems for hydrogen safety*. *Journal of Loss Prevention in the Process Industries*, 21: 136–146.
- Ng, P., & Krauthammer, T. (2004). *Pressure–impulse diagrams for reinforced concrete slabs*. Technical report PTC-TR-007-2004.: Protective Technology Center, The Pennsylvania State University, University Park.
- Ngo, T., Mendis, P., Gupta, A., & Ramsay, J. (2007). *Blast Loading and Blast Effects on Structures – An Overview*. EJSE International: Melbourne .

- Norwegian Ministry of Petroleum and Energy, & Norwegian Ministry of Climate and Environment (NMPE & NMCE). (2020). *The Norwegian Government's hydrogen strategy: towards a low emission society*.
- Oswald, C., & Skerhut, D. (1994). *FACEDAP theory manual*. U.S. Army Corps of Engineers: Omaha.
- Parlin, N., Davids, W., Nagy, E., & Cummins, T. (2014). *Dynamic response of lightweight wood-based flexible wall panels to blast and impulse loading*. *Construction and Building Materials*, 50: 237–245.
- Rhijnsburger, M., van Deursen, J., & van Doormaal, J. (2002). *Development of a toolbox suitable for dynamic response analysis of simplified structures*. 30th DoD Explosives Safety Seminar: Atlanta.
- Rivkin, C., Burgess, R., & Buttner, W. (2015). *Hydrogen Technologies Safety Guide*. NREL.
- Rosen, M. A., & Koohi-Fayegh, S. (2016). *The prospects for hydrogen as an energy carrier: an overview of hydrogen energy and hydrogen energy systems*. *Energy Ecology Environment*, 1:10–29.
- Salaün, N., Grønsund Hanssen, A., & Nilsen, P. E. (2016). *Risk-based Structural Response against Explosion Blast Loads: Systematic One-to-one CFD (FLACS) / NLFEA (Impetus Afea solver) Coupling to Derive Quantified Response Exceedance*. *Chemical Engineering Transactions*, 48, 55-60 DOI:10.3303/CET1648010.
- Sharmila, C., Anandavalli, N., Arunachalam, N., & Prakash, A. (2014). *Pressure-Impulse diagram for damage assesment of structural elements subjected to blast loads: a state of art review*. IJCIET.
- Shepherd, J. E. (2007). *Structural Response to Explosions*. Pasadena.
- Shi, Y., Hao, H., & Li, Z.-X. (2008). *Numerical derivation of pressure–impulse diagrams for prediction of RC column damage to blast loads*. *International Journal of Impact Engineering* 35: 1213–1227.
- Shi, Y., Li, Z.-X., & Hao, H. (2010). *A new method for progressive collapse analysis of RC frames under blast loading*. *Engineering Structures* 32: 1691-1703.
- Shope, R. (2007). *Comparisons of an alternative pressure–impulse (P–I) formulation with experimental and finite element results*. The international symposium on the effects of munitions with structures (ISIEMS), vol 12.1.
- Skjold, T. (2018a). *Experimental investigation of vented hydrogen deflagrations in containers: homogeneous and inhomogeneous mixtures*. Report HySEA-D2-08-2018: 638 pp.
- Skjold, T. (2018b). *Vented hydrogen deflagrations in 20-foot ISO containers*. 12th International Symposium on Hazards, Prevention and Mitigation of Industrial Explosions (12 ISHPMIE), Kansas City, 12-17 August: 823-846.

- Skjold, T., Hisken, H., Bernard, L., & Hanssen, A. G. (2019c). *Structural response of 20-foot shipping containers during vented hydrogen deflagrations*. 27th International Colloquium on the Dynamics of Explosions and Reactive Systems (27 ICDERS), Beijing, 28 July – 2 August 2019: 6 pp.
- Skjold, T., Hisken, H., Bernard, L., Mauri, L., Atanga, G., Lakshmipathy, S., . . . Huser, A. (2019d). *Blind-prediction: Estimating the consequences of vented hydrogen deflagrations for inhomogeneous mixtures in 20-foot ISO containers*. *Journal of Loss Prevention in the Process Industries*, 61: 220–236.
- Skjold, T., Hisken, H., Lakshmipathy, S., Atanga, G., Carcassi, M., Schiavetti, M., . . . Bauwens, C. (2019a). *Blind-prediction: Estimating the consequences of vented hydrogen deflagrations for homogeneous mixtures in 20-foot ISO containers*. *International Journal of Hydrogen Energy*, 44: 8997-9008.
- Skjold, T., Hisken, H., Lakshmipathy, S., Atanga, G., van Wingerden, M., Olsen, K., . . . van Wingerden, K. (2019b). *Vented hydrogen deflagrations in containers: effect of congestion for homogeneous and inhomogeneous mixtures*. *International Journal of Hydrogen Energy*, 44: 8819-8832.
- Skjold, T., Souprayen, C., & Dorofeev, S. (2018c). *Fires and explosions*. *Progress in Energy and Combustion Science* 64: 2-3.
- Soh, T., & Krauthammer, T. (2004). *Load–impulse diagrams of reinforced concrete beams subjected to concentrated transient loading*. Technical report PTC-TR-006-2004: Protective Technology Center, The Pennsylvania State University, University Park.
- Tedesco, J. W., McDougal, W. G., & Ross, W. A. (1999). *Structural dynamics: Theory and Applications* (1st. ed.). Prentice Hall: Englewood Cliffs.
- Vendra, C. M., & Wen, J. X. (2019). *Numerical modelling of vented lean hydrogen deflagrations in an ISO container*. *International Journal of Hydrogen Energy*, 44: 8767-8779.
- Wang, W., Zhang, D., Lu, F., Wang, S.-C., & Tang, F. (2013). *Experimental study and numerical simulation of the damage mode of a square reinforced concrete slab under close-in explosion*. *Engineering Failure Analysis*, 27: 41–51.
- Xu, J., Wu, C., & Li, Z.-X. (2014). *Analysis of direct shear failure mode for RC slabs under external explosive loading*. *International Journal of Impact Engineering*, 69: 136-148.

Appendix A: Results from simulated P-I curves for 5, 10, 20 and 30 cm displacement

Table A1. Study 1: P-I curve for maximum wall displacement $w_{max} = 20$ cm with 355 MPa.

Study	Run	P_m [kPa]	I [Pas]	w_{max} [cm]	w^+_{max} [cm]
1	1	34	40000		20.38
	2	34	20000		20.42
	3	33	10000		20.53
	4	30	5000		20.15
	5	29	2500		20.09
	6	28.5	1250	19.76	
	7	27.5	625		20.44
	8	30	468		20.74
	9	37	390		20.80
	10	58	340		20.54
	11	74	313		20.99
	12	80	300		20.02
	13*	33.37035	39592.54	19.88	
	14*	33.38752	39866.78	19.89	

*Values from quasi-static HySEA experiment for wall 1 (13) and 2 (14).

Table A2. Study 2: P-I curve for maximum wall displacement $w_{max} = 10$ cm with 355 MPa.

Study	Run	P_m [kPa]	I [Pas]	w_{max} [cm]	w^+_{max} [cm]
2	1	27	40000		10.05
	2	27	20000		10.03
	3	27	10000		10.46
	4	26	5000	9.837	
	5	26	2500	9.89	
	6	26	1250	9.863	
	7	22	625		10.03
	8*	23	313		10.67
	9	24	290		10.68
	10*	25	280		10.85
	11*	26	270		10.90
	12*	27	260		10.81
	13	28	250		10.63
	14*	29	240		10.36
	15	30	230		10.02
	16*	40	225		10.67
	17	50	220		10.84
	18	60	210		10.47
	19	70	210		10.77
	20	80	210		10.98

*Run not included in the plot.

Table A3. Study 3: P-I curve for maximum wall displacement $w_{max} = 5$ cm with 355 MPa.

Study	Run	P_m [kPa]	I [Pas]	w_{max} [cm]	w_{max}^+ [cm]
3	1	22	40000		5.053
	2	22	20000		5.056
	3	22	10000		5.083
	4	21.5	5000	4.918	
	5	21.5	2500		5.174
	6	21	1250	4.996	
	7	18	625		5.087
	8	15	313		5.012
	9	15	260		5.162
	10	15	230		5.153
	11	15	210		5.094
	12	15.5	190		5.140
	13	16	170		5.016
	14	18	150	4.947	
	15	19	150		5.077
	16	20	145		5.026
	17	21	142		5.009
	18	25	140		5.137
	19	30	135		5.051
	20	40	130		5.003
	21	50	125	4.915	
	22	80	125		5.158

Table A4. Study 4: P-I curve for maximum wall displacement $w_{max} = 30$ cm with 355 MPa.

Study	Run	P_m [kPa]	I [Pas]	w_{max} [cm]	w_{max}^+ [cm]
4	1	67	80000		30.02
	2	67	40000		30.02
	3	67	20000		30.44
	4	52	10000		30.24
	5	41	5000		30.45
	6	37	2500		30.58
	7	34	1250		30.74
	8	35	625		30.18
	9	44	575		30.19
	10	55	550		30.93
	11	60	520		30.01
	12	70	460		30.32
	13	80	458		30.04
	14	100	435		30.30
	15	200	360	29.55	
	16	300	360		30.65
	17	500	360		30.92

Appendix B: Test results from the HySEA project

Table B1. Details about tests included in experiments with Container 1.

Test	Wall 1			Wall 2			Relative test number
	P [kPa]	I [Pas]	D_m [cm]	P [kPa]	I [Pas]	D_m [cm]	
1	2.86	312.03	2.00	2.96	383.29	1.61	1(9)
2	2.50	288.13	4.15	2.65	393.33	4.16	2(9)
3	6.67	530.86	10.58	6.75	619.62	8.60	3(9)
4	5.52	568.39	7.41	5.67	679.18	5.18	4(9)
5	3.93	325.02	1.97	3.84	340.36	1.50	5(9)
6	4.53	389.37	3.63	4.56	369.26	2.80	6(9)
7	19.91	943.66	20.16	18.30	781.90	17.76	7(9)
8	39.79	1494.10	50.00	34.73	1324.74	40.00	8(9)
9			NaN			NaN	9(9)

Table B2. Details about tests included in experiments with Container 2.

Test	Wall 1			Wall 2			Relative test number
	P [kPa]	I [Pas]	D_m [cm]	P [kPa]	I [Pas]	D_m [cm]	
10			NaN			NaN	1(5)
11	4.78	327.32	4.15	4.69	314.72	3.76	2(5)
12	11.35	704.70	17.54	11.64	713.42	18.31	3(5)
13	25.07	1114.82	35.00	26.02	1157.95	33.00	4(5)
14	78.06	1839.06	27.10	79.30	1871.37	30.00	5(5)

Table B3. Details about tests included in experiments with Container 3.

Test	Wall 1			Wall 2			Relative test number
	P [kPa]	I [Pas]	D_m [cm]	P [kPa]	I [Pas]	D_m [cm]	
15	17.85	999.73	30.10	17.75	955.49	34.25	1(6)
16	16.61	700.66	4.12	15.78	707.84	7.14	2(6)
17	10.98	379.94	4.63	11.02	388.98	7.05	3(6)
18	21.25	754.95	12.74	21.69	767.14	19.22	4(6)
19	11.80	400.18	3.80	12.02	414.06	8.88	5(6)
20	30.00	914.31	14.68	27.88	871.06	19.61	6(6)

Table B4. Details about tests included in experiments with Container 4.

Test	Wall 1			Wall 2			Relative test number
	P [kPa]	I [Pas]	D_m [cm]	P [kPa]	I [Pas]	D_m [cm]	
21	9.38	443.35	3.26	9.31	422.98	5.27	1(8)
22	11.01	395.28	7.37	11.29	386.49	5.61	2(8)
23	14.97	449.52	10.07	15.12	434.05	8.11	3(8)
24	12.30	504.24	6.72	12.29	522.34	6.19	4(8)
25	12.97	552.13	5.69	13.37	560.85	5.55	5(8)
26	18.67	963.73	10.15	18.53	942.56	10.36	6(8)
27	23.25	911.75	16.26	22.84	894.28	15.29	7(8)
28	34.30	977.62	18.58	37.11	1013.72	15.01	8(8)

Table B5. Details about tests included in experiments with Container 5.

Test	Wall 1			Wall 2			Relative test number
	P [kPa]	I [Pas]	D_m [cm]	P [kPa]	I [Pas]	D_m [cm]	
29	21.48	1524.59	19.38			NaN	1(6)
30			NaN			NaN	2(6)
31	22.24	835.69	13.39	21.39	808.27	15.52	3(6)
32	19.97	1019.68	10.24	20.73	1033.60	12.22	4(6)
33	23.34	905.76	9.55	24.21	946.47	11.59	5(6)
34			NaN			NaN	6(6)

Table B6. Details about tests included in experiments with Container 6.

Test	Wall 1			Wall 2			Relative test number
	P [kPa]	I [Pas]	D_m [cm]	P [kPa]	I [Pas]	D_m [cm]	
35			NaN			NaN	1(5)
36	17.23	505.30	11.11	18.65	498.77	10.48	2(5)
37	20.25	855.84	11.55	20.90	816.29	11.49	3(5)
38			NaN			NaN	4(5)
44	32.24	867.01	15.22	32.05	854.11	16.16	5(5)

Table B7. Details about tests included in experiments with Container 7.

Test	Wall 1			Wall 2			Relative test number
	P [kPa]	I [Pas]	D_m [cm]	P [kPa]	I [Pas]	D_m [cm]	
45	8.58	336.90	3.51	8.20	302.82	3.86	1(13)
46	16.93	692.48	10.40	15.55	621.98	12.00	2(13)
47	17.60	692.22	15.14	18.81	694.06	12.72	3(13)
48	16.28	699.20	13.06	17.02	709.15	11.72	4(13)
49	16.83	684.24	9.22	17.03	656.60	9.19	5(13)
50	17.49	706.97	12.79	18.62	687.45	11.98	6(13)
51	5.56	301.54	3.60	5.68	286.88	3.71	7(13)
52	6.59	312.08	3.24	6.92	305.33	3.35	8(13)
53	9.38	317.26	6.13	8.33	283.09	6.45	9(13)
54	6.20	267.21	3.93	6.13	268.50	3.86	10(13)
55	14.32	656.98	9.44	15.06	671.22	9.13	11(13)
56	14.49	687.28	9.19	15.25	680.27	8.95	12(13)
57	23.93	768.13	17.66	28.86	805.19	17.97	13(13)

Table B8. Details about tests included in experiments with Container 8.

Test	Wall 1			Wall 2			Relative test number
	P [kPa]	I [Pas]	D_m [cm]	P [kPa]	I [Pas]	D_m [cm]	
58			NaN			NaN	1(3)
59	26.78	804.04	19.62	25.18	804.83	13.78	2(3)
60	29.20	996.24	19.55	26.12	917.74	17.40	3(3)

Table B9. Details about tests included in experiments with Container 9.

Test	Wall 1			Wall 2			Relative test number
	P [kPa]	I [Pas]	D_m [cm]	P [kPa]	I [Pas]	D_m [cm]	
61	42.32	1160.22	43.21	44.31	1161.05	33.21	1(1)

Table B10. Details about tests included in experiments with Container 10.

Test	Wall 1			Wall 2			Relative test number
	P [kPa]	I [Pas]	D_m [cm]	P [kPa]	I [Pas]	D_m [cm]	
62	14.04	683.65	7.38	14.12	665.18	5.58	1(8)
63	15.84	692.11	9.81	16.12	696.72	8.33	2(8)
64	14.59	679.98	9.82	14.81	691.35	8.62	3(8)
65	15.27	683.99	11.08	15.63	663.95	9.56	4(8)
66	10.40	1271.09	6.96	10.35	1307.68	6.10	5(8)
67			NaN	10.65	985.94	6.23	6(8)
68	12.88	728.16	7.59	12.73	705.06	7.23	7(8)
69	57.22	1271.70	52.92	57.86	1338.05	64.26	8(8)

Table B11. Details about tests included in experiments with Container 11.

Test	Wall 1			Wall 2			Relative test number
	P [kPa]	I [Pas]	D_m [cm]	P [kPa]	I [Pas]	D_m [cm]	
70	33.37	39592.54	18.91	33.39	39866.78	19.64	33.39

Table B12. Details about tests included in experiments with Container 12.

Test	Wall 1			Wall 2			Relative test number
	P [kPa]	I [Pas]	D_m [cm]	P [kPa]	I [Pas]	D_m [cm]	
71	11.28	1103.03	5.30	10.86	1096.07	4.24	1(2)
72	44.57	1396.32	35.22	46.19	1372.04	35.73	2(2)

Appendix C: Further test details from the HySEA project

Table C1. Details about the relative test number (RC) of the containers, geometry configurations (GC), ventilation device (VD), ignition position (IG), mixture generation (MG), and initial turbulence (IT). Explanations below.

Container	Test	RC	GC	VD	IG	MG	IT
1	1	1	1	1	1	1	0
	2	2	1	1	1	1	0
	3	3	2	1	1	1	0
	4	4	2	1	1	1	0
	5	5	1	1	1	1	0
	6	6	2	1	1	1	0
	7	7	2	1	1	1	0
	8	8	2	1	1	1	0
	9	9	2	2	1	1	0
2	10	1	2	1	1	1	0
	11	2	3	1	1	1	0
	12	3	3	1	1	1	0
	13	4	3	1	1	1	0
	14	5	4	1	1	1	0
3	15	1	1	4	2	1	0
	16	2	1	3	2	1	0
	17	3	5	3	2	1	0
	18	4	5	4	2	1	0
	19	5	5	3	2	1	0
	20	6	5	4	2	1	0
4	21	1	1	3	2	1	0
	22	2	5	3	2	1	0
	23	3	5	3	2	1	0
	24	4	5	3	2	1	0
	25	5	1	3	2	1	0
	26	6	1	4	2	1	0
	27	7	5	4	2	1	0
	28	8	5	4	2	1	0
5	29	1	5	3	2	1	0
	30	2	5	4	2	1	0
	31	3	5	4	2	1	0
	32	4	1	4	2	1	0
	33	5	5	4	2	1	0
	34	6	5	3	2	1	0
6	35	1	5	3	2	1	1
	36	2	5	3	2	1	1
	37	3	5	3	2	1	1
	38	4	5	3	2	1	1
	44	5	1	4	3	3	0

Container	Test	RC	GC	VD	IG	MG	IT
7	45	1	1	3	3	1	0
	46	2	1	4	3	1	0
	47	3	1	4	3	1	0
	48	4	5	4	3	1	0
	49	5	5	4	3	3	0
	50	6	5	4	3	2	0
	51	7	5	3	3	2	0
	52	8	5	3	3	3	0
	53	9	1	3	3	3	0
	54	10	1	3	3	2	0
	55	11	1	4	3	2	0
	56	12	1	4	3	3	0
	57	13	1	4	3	2	0
8	58	1	1	4	3	2	0
	59	2	1	4	3	2	0
	60	3	5	4	3	2	0
9	61	1	5	4	3	2	0
10	62	1	5	4	3	2	0
	63	2	5	4	3	3	0
	64	3	1	4	3	3	0
	65	4	1	4	3	2	0
	66	5	1	4	3	2	2
	67	6	1	4	3	2	2
	68	7	1	4	3	2	2
	69	8	5	4	2	1	0
11	70	1	1	0	1	1	0
12	71	1	6	4	2	1	0
	72	2	6	4	2	1	0

Explanations:

RC Relative test number for this container

GC Geometry configuration:

1. Frame only (FO)
2. Bottle basket inner position (BB1)
3. Pipe rack in inner position (PR1)
4. Pipe rack inner pos. & bottle basket outer pos. (PR1BB3)
5. Pipe rack middle position (PR2)
6. High congestion (BB1PR3 + additional obstacles (HC))

VD Venting device:

- 0: Closed container (S)
- 1: Container doors open (D)
- 2: Container doors closed (C)
- 3: Polyethylene roof (O)
- 4: Bulged single-sheet vent panels roof (P)

IG Ignition position:

- 0: no ignition
- 1: back wall centre (bc)
- 2: floor centre (fc)
- 3: back wall upper (bu)

MG Mixture generation:

- 1: Homogeneous mixture (H)
- 2: Jet release (J)
- 3: Diffusive release (D)

IT Initial turbulence:

- 0: Initially quiescent
- 1: Turbulence generated by a fan
- 2: Turbulent generated by the transient release

Appendix D: Maximum displacement and permanent deformation from the HySEA project

Table D1. Details about the maximum displacement, D_m , and permanent deformation, D_p , and their associated displacement or deformation groups.

Container	Test	P [kPa]	I [Pa s]	D_m [cm]	Group D_m [cm]	D_p [cm]	Group D_p [cm]	Comment on pressure peaks
1	1	2.9	350.0	1.8	0-5	0.0	0-5	MP
	2	2.6	340.0	4.2	0-5	0.1	0-5	MP
	3	6.7	580.0	9.6	5-10	1.1	0-5	MP
	4	5.6	620.0	6.3	5-10	0.1	0-5	MP
	5	3.9	330.0	1.7	0-5	0.0	0-5	MP
	6	4.5	380.0	3.2	0-5	0.2	0-5	MP
	7	19.1	860.0	19.0	15-20	3.1	0-5	DP
	8	37.3	1410.0	45.0	30+	0.0	0-5	DP
	9	129.5	4780.0	-	-	-	-	SP
2	10	12.7	740.0	-	-	-	-	DP
	11	4.7	320.0	4.0	0-5	0.2	0-5	DP
	12	11.5	710.0	17.9	15-20	2.0	0-5	DP
	13	25.5	1140	34.0	30+	3.1	0-5	DP
	14	78.7	1860	28.5	20-30	10.3	10-15	DP
3	15	17.8	970.0	32.2	30+	10.1	10-15	DP
	16	16.3	700.0	5.6	5-10	0.7	5-10	MP
	17	11.0	380.0	5.8	5-10	0.6	5-10	MP
	18	21.4	760.0	16.0	15-20	4.0	5-10	SP
	19	11.9	410.0	6.3	5-10	1.4	0-5	MP
	20	28.8	890.0	17.1	15-20	8.3	5-10	DP
4	21	9.3	430.0	4.3	0-5	0.4	0-5	MP
	22	11.2	390.0	6.5	5-10	1.2	0-5	MP
	23	15.0	440.0	9.1	5-10	2.6	0-5	DP
	24	12.3	510.0	6.5	5-10	0.3	0-5	DP
	25	13.1	560.0	5.6	5-10	0.3	0-5	DP
	26	18.6	950.0	10.3	10-15	0.7	0-5	DP
	27	23.0	900.0	15.8	15-20	4.2	0-5	MP
	28	30.9	860.0	16.8	15-20	8.1	5-10	DP
5	29	21.5	1520.0	17.2	15-20	6.9	5-10	DP
	30	18.3	710.0	-	-	-	-	SP
	31	21.9	820.0	14.5	10-15	1.6	0-5	MP
	32	20.2	1020.0	11.2	10-15	1.2	0-5	DP
	33	23.6	920.0	10.6	10-15	0.4	0-5	DP
	34	42.3	3170	-	-	-	-	DP
6	35	11.2	329.4	-	-	-	-	DP
	36	17.9	502.0	10.8	10-15	3.1	0-5	DP
	37	20.6	836.1	11.5	10-15	1.3	0-5	SP

	38	13.8	472.2	-	-	-	0-5	DP
	44	32.2	862.7	15.7	15-20	7.1	5-10	SP
7	45	8.4	320.0	3.7	0-5	0.2	0-5	DP
	46	16.3	660.0	11.2	10-15	1.9	0-5	SP
	47	18.2	690.0	13.9	10-15	2.3	0-5	SP
	48	16.6	700.0	12.4	10-15	1.3	0-5	MP
	49	16.9	670.4	9.2	5-10	1.0	0-5	SP
	50	18.1	697.2	12.4	10-15	0.6	0-5	SP
	51	5.6	295.7	3.7	0-5	0.1	0-5	DP
	52	6.7	309.4	3.3	0-5	0.0	0-5	DP
	53	8.9	300.2	6.3	5-10	0.0	0-5	SP
	54	6.2	267.7	3.9	0-5	0.2	0-5	SP
	55	14.7	664.1	9.3	5-10	0.9	0-5	SP
	56	14.9	683.8	9.1	5-10	0.8	0-5	SP
	57	26.4	786.7	17.8	15-20	4.2	0-5	SP
8	58	-	-	-	-	-	-	-
	59	26.1	804.4	16.7	15-20	3.0	0-5	SP
	60	27.7	957.0	18.5	15-20	6.4	5-10	SP
9	61	43.2	1160.6	38.2	30+	26.3	20-30	SP
10	62	14.1	674.4	6.5	5-10	0.9	0-5	SP
	63	16.0	694.1	9.1	5-10	1.0	0-5	SP
	64	14.7	684.9	9.2	5-10	0.0	0-5	SP
	65	15.5	674.0	10.3	10-15	0.0	0-5	SP
	66	10.4	1289.4	6.5	5-10	0.6	0-5	SP
	67	10.7	980.1	6.2	5-10	0.5	0-5	SP
	68	12.8	716.6	7.4	5-10	0.5	0-5	DP
	69	57.5	1300.0	58.6	30+	47.6	30+	SP
11	70	33.5	39700.0	19.3	15-20	6.5	5-10	SP
12	71	11.0	1100.0	4.8	0-5	0.2	0-5	DP
	72	45.5	1380.0	35.5	30+	27.8	20-30	SP

* Single peak (SP), Double peak (DP), Multiple peaks (MP)

Appendix E: P-I curve results for w_{max} with a material yield strength of 235 MPa

Table E1. Study 9: P-I diagram for max wall displacement $w_{max} = 20$ cm with 235 MPa.

Study	Run	P_m [kPa]	I [Pas]	w_{max} [cm]	w_{max}^+ [cm]
9	1	22	40000	19.52	
	2	22	20000	19.62	
	3	22	10000	19.97	
	4	20	5000		20.13
	5	19	2500	19.69	
	6	19	1250	19.68	
	7	19	625		20.19
	8	33	313		20.91
	9	40	290		20.09
	10	20	468		20.63
	11	21	390	19.83	
	12	25	340		20.43
	13	55	260		20.07
	14	80	250		20.25

Table E2. Study 10: P-I diagram for max wall displacement $w_{max} = 10$ cm with 235 MPa.

Study	Run	P_m [kPa]	I [Pas]	w_{max} [cm]	w_{max}^+ [cm]
10	1	17.7	40000		10.23
	2	17.7	20000		10.20
	3	17.7	10000		10.40
	4	17.3	5000		10.48
	5	16.8	2500		10.65
	6	16.5	1250	9.879	
	7	16	625	9.561	
	8*	16	313		10.43
	9	16	290		10.03
	10*	17	280		10.90
	11*	16	270	9.595	
	12*	17	260		10.26
	13	18	250		10.65
	14*	18	240		10.23
	15	20	230		10.79
	16*	20	225		10.52
	17	20	220		10.26
	18	24	210		10.74
	19	35	180	9.899	
	20	60	170		10.32
	21	80	170		10.69

*Run not included in the plot.

Table E3. Study 11: P-I diagram for max wall displacement $w_{max} = 5$ cm with 235 MPa.

Study	Run	P_m [kPa]	I [Pas]	w_{max} [cm]	w^+_{max} [cm]
11	1	15.6	40000		5.030
	2	15.6	20000		5.038
	3	15.5	10000	4.999	
	4	15.3	5000	4.947	
	5	15.1	2500	4.951	
	6	14.6	1250	4.969	
	7	14.3	625	4.959	
	8	12.3	313		5.054
	9	12	260		5.065
	10	11.8	230	4.965	
	11	11.9	210		5.031
	12	12	190		5.019
	13	12.2	170	4.959	
	14	13	150	4.976	
	15	13.5	145		5.027
	16	14	140		5.028
	17	15	135		5.093
	18	16	130		5.073
	19	17	125	4.987	
	20	30	115		5.031
	21	45	110		5.085
	22	60	105	4.971	
	23	80	103	4.972	

Table E4. Study 12: P-I diagram for max wall displacement $w_{max} = 30$ cm with 235 MPa.

Study	Run	P_m [kPa]	I [Pas]	w_{max} [cm]	w^+_{max} [cm]
12	1	50	80000		30.74
	2	50	40000		30.75
	3	42	20000	29.54	
	4	35	10000		30.35
	5	28	5000	29.72	
	6	24	2500		30.79
	7	23	1250		30.92
	8	23	625		30.20
	9	23.5	575		30.15
	10	24	550		30.32
	11	25	520		30.80
	12	27	460		30.27
	13	35	458		30.91
	14	45	435		30.94
	15	60	360		30.01
	16	80	340		30.25

Appendix F: Percentage increase in displacement with a dent

The formula used for the percentage calculations for the increase in displacement is:

$$\% = \frac{\text{new value} - \text{original value}}{\text{original value}} * 100$$

Example for run 1 in table F1 for amp= 1 is shown below:

$$\frac{23.57 - 21.16}{21.16} * 100 = 11.39 \%$$

Table F1. Study for max wall displacement $w_{max} = 20$ cm with 355 MPa and dent in one wall, size of dent amp=0.1 vs 1 vs 0.5 with an increase in percentage.

Run	Amp = 1			Amp = 0.5			Amp = 0.1		
	-x direction w_{max} [cm]	+x direction w_{max} [cm]	%	-x direction w_{max} [cm]	+x direction w_{max} [cm]	%	-x direction w_{max} [cm]	+x direction w_{max} [cm]	%
1	21.16	23.57	11.39	20.97	23.29	11.06	20.58	21.41	4.03
2	21.14	23.66	11.92	21.14	23.34	10.41	21.04	21.57	2.52
3	21.85	24.27	11.08	21.58	23.90	10.75	21.59	22.13	2.50
4	23.19	23.85	2.85	24.66	25.96	5.27	21.27	23.80	11.89
5	27.74	29.08	4.83	23.94	29.35	22.60	20.45	24.32	18.92
6	21.92	33.40	52.37	20.70	30.97	49.61	19.84	23.65	19.20
7	20.78	32.63	57.03	20.34	29.04	42.77	20.42	22.74	11.36
8	20.75	30.77	48.29	20.59	27.44	33.27	20.69	22.68	9.62
9	21.10	29.69	40.71	20.66	26.60	28.75	20.76	22.72	9.44
10	20.68	28.35	37.09	20.49	26.23	28.01	20.59	23.07	12.04
11	20.73	26.82	29.38	20.82	25.22	21.13	20.96	22.23	6.06
12	19.72	25.77	30.68	19.84	24.17	21.82	19.98	21.22	6.21

Table F2. Study for max wall displacement $w_{max} = 10$ cm with 355 MPa and dent in one wall, size of dent amp=0.1 vs 1 vs 0.5 with an increase in percentage.

Run	Amp = 1			Amp = 0.5			Amp = 0.1		
	-x direction w_{max} [cm]	+x direction w_{max} [cm]	%	-x direction w_{max} [cm]	+x direction w_{max} [cm]	%	-x direction w_{max} [cm]	+x direction w_{max} [cm]	%
1	12.04	20.79	72.67	11.73	19.62	67.26	10.86	14.78	36.10
2	12.16	20.83	71.30	12.24	19.72	61.11	11.25	14.98	33.16
3	12.16	21.05	73.11	13.09	20.37	55.61	12.01	15.81	31.64
4	11.35	20.92	84.32	14.61	21.66	48.25	10.80	16.42	52.04
5	15.06	24.21	60.76	12.84	24.64	91.90	10.13	16.85	66.34
6	14.59	30.64	110.01	11.95	25.81	115.98	10.05	15.83	57.51
7	9.866	26.25	166.07	9.807	20.61	110.16	9.959	12.19	22.40
8	10.31	20.74	101.16	10.47	15.71	50.05	10.66	11.97	12.29
9	10.34	19.26	86.27	10.50	15.13	44.10	10.67	11.97	12.18
10	10.51	18.69	77.83	10.68	15.03	40.73	10.84	12.14	11.99
11	10.64	18.20	71.05	10.73	14.83	38.21	10.89	12.15	11.57
12	10.59	17.69	67.04	10.68	14.55	36.24	10.81	12.06	11.56
13	10.40	17.07	64.13	10.50	14.19	35.14	10.62	11.85	11.58
14	10.14	16.33	61.05	10.24	13.77	34.47	10.35	11.54	11.50
15	9.777	15.49	58.43	9.916	13.29	34.03	10.01	11.16	11.49
16	10.47	16.11	53.87	10.57	14.01	32.54	10.67	11.99	12.37
17	10.68	16.91	58.33	10.74	14.27	32.87	10.84	12.16	12.18
18	10.26	16.91	64.81	10.34	13.91	34.53	10.45	11.60	11.00
19	10.52	17.51	66.44	10.62	14.33	34.93	10.76	11.84	10.04
20	10.75	17.87	66.23	10.83	14.65	35.27	10.96	12.05	9.95

Table F3. Study for max wall displacement $w_{max} = 5$ cm with 355 MPa and dent in one wall, size of dent amp=0.1 vs 1 vs 0.5 with an increase in percentage.

Run	Amp = 1			Amp = 0.5			Amp = 0.1		
	-x direction w_{max} [cm]	+x direction w_{max} [cm]	%	-x direction w_{max} [cm]	+x direction w_{max} [cm]	%	-x direction w_{max} [cm]	+x direction w_{max} [cm]	%
1	6.802	17.36	155.22	6.356	14.69	131.12	5.103	5.453	6.86
2	6.806	17.40	155.66	6.368	14.83	132.88	5.118	5.488	7.23
3	6.930	17.71	155.56	6.532	15.36	135.15	5.175	5.525	6.76
4	6.935	18.28	163.59	6.562	16.29	148.25	4.983	5.251	5.38
5	8.635	19.96	131.15	7.232	17.49	141.84	5.187	5.486	5.76
6	9.201	24.08	161.71	6.552	16.93	158.39	5.031	5.537	10.06
7	6.798	20.39	199.94	5.204	12.06	131.74	5.100	5.404	5.96
8	5.266	13.52	156.74	5.026	8.319	65.52	5.015	5.255	4.79
9	5.216	13.03	149.81	5.156	8.072	56.56	5.162	5.428	5.15
10	5.114	12.28	140.13	5.137	7.779	51.43	5.151	5.406	4.95
11	5.046	11.28	123.54	5.075	7.499	47.76	5.092	5.326	4.60
12	5.081	10.20	100.75	5.116	7.364	43.94	5.137	5.371	4.56
13	4.966	9.254	86.35	4.999	6.991	39.85	5.014	5.218	4.07
14	4.890	8.521	74.25	4.926	6.684	35.69	4.945	5.132	3.78
15	5.005	8.632	72.47	5.050	6.852	35.68	5.074	5.278	4.02
16	4.963	8.409	69.43	4.998	6.720	34.45	5.023	5.220	3.92
17	4.943	8.292	67.75	4.982	6.654	33.56	5.006	5.190	3.68
18	5.081	8.400	65.32	5.111	6.774	32.54	5.133	5.325	3.74
19	5.003	8.454	68.98	5.027	6.586	31.01	5.048	5.201	3.03
20	4.944	8.288	67.64	4.971	6.552	31.80	4.999	5.193	3.88
21	4.851	8.017	65.26	4.880	6.465	32.48	4.910	5.137	4.62
22	5.056	8.328	64.72	5.090	6.848	34.54	5.145	5.441	5.75

Table F4. Study for max wall displacement $w_{max} = 30$ cm with 355 MPa and dent in one wall, size of dent amp=0.1 vs 1 vs 0.5 with an increase in percentage.

Run	Amp = 1			Amp = 0.5			Amp = 0.1		
	-x direction w_{max} [cm]	+x direction w_{max} [cm]	%	-x direction w_{max} [cm]	+x direction w_{max} [cm]	%	-x direction w_{max} [cm]	+x direction w_{max} [cm]	%
1	30.02	28.74	-4.26	30.00	29.37	-2.10	30.05	29.90	-0.50
2	30.24	29.06	-3.90	30.58	29.99	-1.93	30.15	29.95	-0.66
3	32.44	31.01	-4.41	31.38	31.01	-1.18	30.61	30.68	0.23
4	33.38	30.90	-7.43	32.65	32.04	-1.87	30.59	30.70	0.36
5	33.40	31.59	-5.42	33.01	34.09	3.27	30.47	30.35	-0.39
6	35.49	36.51	2.87	32.56	35.26	8.29	30.94	31.82	2.84
7	31.88	35.75	12.14	31.31	34.66	10.70	30.84	32.19	4.38
8	30.25	38.30	26.61	30.22	36.08	19.39	30.21	32.07	6.16
9	32.40	41.20	27.16	30.75	39.59	28.75	30.52	36.18	18.55
10	33.04	45.21	36.83	31.84	42.66	33.98	30.98	39.22	26.60
11	31.96	44.57	39.46	31.18	42.27	35.57	30.08	38.56	28.19
12	30.44	40.17	31.96	29.47	38.94	32.13	30.26	35.69	17.94
13	30.81	41.03	33.17	30.58	40.07	31.03	30.11	36.96	22.75
14	30.83	40.05	29.91	30.63	39.32	28.37	30.33	36.63	20.77
15	29.49	34.63	17.43	29.51	33.78	14.47	29.54	31.10	5.28
16	30.65	34.87	13.77	30.66	34.10	11.22	30.65	31.68	3.36
17	30.91	35.02	13.30	30.93	34.26	10.77	30.92	31.88	3.10

Appendix G: Uncertainty calculation

$$\text{Absolute uncertainty} = \frac{(\text{max} - \text{min})}{2}$$

For wall 1:

$$\frac{(19.88 - 18.91)}{2} = \pm 0.485$$

For wall 2:

$$\frac{(19.89 - 19.64)}{2} = \pm 0.125$$

$$\text{Relative uncertainty [\%]} = \frac{\text{Absolute uncertainty}}{\text{Measured Value}} * 100$$

For wall 1:

$$\frac{0.485}{19.88} * 100 = 2.4\%$$

For wall 2:

$$\frac{0.125}{19.89} * 100 = 0.6\%$$

Appendix H: P-I curve results from triangular pressure loads

Table H1. Results for max wall displacement, $w_{max} = 20$ cm, for triangular load, $tr/td=0.5$ with material yield strength of 355 MPa.

Study	Run	P_m [kPa]	I [Pas]	w_{max}^- [cm]	w_{max}^+ [cm]
13	1	34	40000		20.51
	2	33	20000		20.48
	3	32	10000		20.43
	4	30	5000	19.84	
	5	31	2500	19.60	
	6	32.5	1250	19.57	
	7	32.5	625		20.15
	8	35	468		20.05
	9	41	390		20.07
	10	60	340		20.03
	11	74	313	19.96	
	12	80	305	19.78	

Table H2. Results for max wall displacement, $w_{max} = 20$ cm, for triangular load, $tr/td=0.000001$ with material yield strength of 355 MPa.

Study	Run	P_m [kPa]	I [Pas]	w_{max}^- [cm]	w_{max}^+ [cm]
14	1	23	40000		20.02
	2	23.1	20000		20.05
	3	23.3	10000		20.10
	4	23.7	5000		20.20
	5	24.5	2500		20.28
	6	26.2	1250		20.18
	7	31	625		20.00
	8	38	468		20.44
	9	52	390		20.33
	10	60	360	19.93	
	11	68	340		20.35
	12	80	320		20.30